



# Investigations on Laser-Cluster Interaction Concerning the Acceleration of Protons and Electrons and the Generation of X-Ray Radiation

Doctoral thesis

Inaugural-Dissertation

zur Erlangung des Doktorgrades (Dr. rer. nat.)  
der Naturwissenschaften im Fachbereich Physik  
der Mathematisch-Naturwissenschaftlichen Fakultät  
der Westfälischen Wilhelms-Universität Münster

vorgelegt von

**Lukas Leßmann**

aus Münster

- 2021 -



Dekan: Prof. Dr. Michael Rohlfing  
Erster Gutachter: Prof. Dr. Alfons Khoukaz  
Zweiter Gutachter: Prof. Dr. Christian Klein-Bösing

Tag der Disputation:  
Tag der Promotion:



# Kurzzusammenfassung

Cluster Jet Targets sind eine vielversprechende Alternative zu Folien oder Gas Jets für die Laser-Plasma Physik. Sie können viele Nachteile dieser herkömmlichen Targets überwinden, indem sie einen kontinuierlichen Strom von Materie in Form von massebegrenzten Clustern liefern.

Das in dieser Arbeit vorgestellte CryoFlash Experiment untersucht die Wechselwirkung eines hoch intensiven und ultra kurzen Laser Pulses mit einem Cluster Jet Target höchster Dichte. Das dafür verwendete Cluster Jet Target, das MCT-D, wurde speziell für dieses Experiment entworfen und an der Universität Münster gebaut.

Durch Messungen von Streulicht (Mie-Streuung) an den Clustern bei Stagnationsbedingungen im gasförmigen Bereich und durch Vermessung der Schatten der Cluster bei ultra kurzer Belichtung bei Stagnationsbedingungen im flüssigen Bereich konnten die Clustergrößenverteilungen über einen weiten Parameterraum bestimmt werden.

Das neu gebaute MCT-D wurde am ARCTURUS Laser System der Heinrich Heine Universität Düsseldorf für zahlreiche Messreihen installiert. Dabei konnten ultra kurze Protonenpulse mit hoher Stabilität und Energien bis etwa 300 keV nachgewiesen werden.

Es konnte ein niedriger Fluss an hochenergetischen Elektronen (bis etwa 12 MeV) in ultra kurzen Pulsen und in der Ausbreitungsrichtung des Lasers detektiert werden. Ein wesentlich höherer Elektronenfluss wurde in einer Ringstruktur und bei Energien unterhalb von 150 keV nachgewiesen.

Bei der Laser-Cluster Wechselwirkung entstehende ultra kurze Röntgenpulse mit etwa  $7 \times 10^6$  Photonen pro Laserpuls konnten in einem Öffnungswinkel von 4 mrad gemessen werden. Die Energie der Röntgenstrahlung wurde durch verschiedene Filter in den Bereich zwischen 50 eV und einigen keV eingegrenzt.



# Abstract

Cluster jet targets are a promising alternative to foil or gas jet targets in laser plasma physics. They overcome many drawbacks of the conventional targets by generating a constant flow of mass limited clusters.

The CryoFlash experiment, presented in this thesis, investigates the interaction of a super intense and ultra short laser pulse with a cluster jet target of highest density. The cluster jet target used, the MCT-D, was designed and built specially for this experiment at the Westfälische Wilhelms-University of Münster.

Using measurements of scattered light (Mie scattering) at the clusters at stagnation conditions in the gaseous regime and shadowgraphy images of the clusters at stagnation conditions in the liquid regime, the cluster size distributions were determined over a wide parameter range.

The newly built MCT-D was installed at the ARCTURUS laser system of the Heinrich Heine University Düsseldorf for various measurement series. Ultra short proton pulses with energies up to 300 keV were measured at a very high shot-to-shot stability.

Ultra short electron pulses with a low flux and with energies up to 12 MeV were measured in laser forward direction. A higher flux of lower energetic electrons (below 150 keV) was detected in a ringlike structure around the laser propagation direction.

Ultra short X-ray pulses generated during the laser cluster interaction with around  $7 \times 10^6$  photons per shot were detected in an opening angle of 4 mrad. Different filters determined the X-ray energy to be between 50 eV and a few keV.





# Contents

<b>1</b>	<b>Introduction</b>	<b>1</b>
<b>2</b>	<b>Laser-matter interaction</b>	<b>5</b>
2.1	Single atom-laser interaction . . . . .	5
2.2	Electron-laser interaction . . . . .	8
2.3	Proton acceleration mechanisms . . . . .	12
2.4	X-ray generation mechanisms . . . . .	15
<b>3</b>	<b>Cryogenic cluster jet targets</b>	<b>19</b>
3.1	Working principle and gas flow theory . . . . .	19
3.2	The MCT-D . . . . .	27
3.3	Cluster jet density estimation . . . . .	37
3.4	Cluster size determination using Mie-Scattering . . . . .	40
3.5	Cluster size determination using shadowgraphy . . . . .	50
<b>4</b>	<b>The ARCTURUS laser system</b>	<b>57</b>
4.1	Pre-amplification . . . . .	57
4.2	Main-amplification . . . . .	58
<b>5</b>	<b>Protons accelerated by laser-cluster interaction</b>	<b>63</b>
5.1	Experimental setup . . . . .	64
5.2	Evaluation method . . . . .	68
5.2.1	Systematic uncertainties . . . . .	73
5.3	Proton data . . . . .	77
5.4	Accelerated electrons . . . . .	88
<b>6</b>	<b>X-rays generated by laser-cluster interaction</b>	<b>95</b>
6.1	Experimental setup . . . . .	96

6.2	Evaluation method . . . . .	99
6.3	X-ray detection . . . . .	104
<b>7</b>	<b>Conclusion</b>	<b>115</b>
<b>A</b>	<b>Appendix</b>	<b>119</b>
A.1	Proton spectra taken under $45^\circ$ . . . . .	119
A.2	Proton stability measurements . . . . .	121
A.3	Proton laser pulse energy scans . . . . .	124

# 1 Introduction

Accelerated protons are required for numerous applications in nuclear and particle physics, as seeds for particle accelerators, in material science, for radiation hardness tests and for medical treatments as proton therapy. Currently these accelerated protons are generated by conventional particle accelerators like cyclotrons or linear accelerators by passing either an alternating electric field multiple times or multiple electric fields in a row. This conventional acceleration requires large facilities scaling with the required proton energy, reducing the availability of accelerated protons for science, industry and medicine.

Ultra short X-ray pulses  $\tau \sim O(\text{fs})$  are highly useful for the investigation of ultra fast processes e.g. in molecules or atoms as well as in pump-probe experiments or as pumps for short wavelength lasers. There are a few facilities able to produce such X-ray pulses by sending accelerated electrons of relativistic energies through undulators consisting of an array of magnetic fields with successive changing field directions. This causes a slalom motion of the electrons under X-ray emission in forward direction at every turning point of the slalom. These X-rays accumulate to a very short and intense pulse. However, due to the high cost of such facilities the access is very limited.

The discovery of the laser in 1960 by Theodore Maiman and the principle of chirped pulse amplification (CPA) in 1985 by Gérard Mourou and Donna Strickland (Noble prize in 2018) resulted in easily accessible focus intensities up to  $10^{20} \text{ W/cm}^2$ . This opened a completely new approach for the acceleration of protons or ions and the generation of ultra short X-ray pulses. During the interaction of a short laser pulse of such a focus intensity with matter a plasma is formed. Atoms are ionised, ions and electrons are separated macroscopically causing a very strong electric field up to the TV/m scale, accelerating ions and electrons. The electrons propagate in the alternating magnetic field of the laser pulse generating X-ray radiation like in an undulator. Besides the accelerated ions and the generated X-ray radiation, the accelerated electrons may be used directly

for scientific applications or techniques such as electron melting, electron cutting or radio therapy. Currently, large facilities such as microtrons or synchrotrons are required to accelerate electrons to the energies necessary.

The most common targets for laser plasma experiments are thin foils. In the interaction of an ultra short laser pulse of high intensity with a thin foil, ions are accelerated by the target normal sheath acceleration mechanism. Proton energies of up to 58 MeV have already been reported [S<sup>+</sup>00]. Despite this very promising energy, foil targets come with several drawbacks. Since the interaction leaves a hole in the foil, the target has to be changed after every shot resulting in a very low interaction frequency. Additionally, some of the matter of the foil is severed by the laser pulse as debris and may damage the optical components in the interaction chamber. Furthermore, the shot-to-shot stability is inadequate and a lot of energy is lost in the interaction by electrons leaving the interaction region through the foil transversal to the laser propagation direction.

Many different target alternatives have already been tested. This includes e.g. gas-jets [PV<sup>+</sup>19], frozen droplets [S<sup>+</sup>19, A<sup>+</sup>20], solid spheres [O<sup>+</sup>16], liquid jets [G<sup>+</sup>17] and hydrogen ribbons [M<sup>+</sup>16]. Beside these, there is another type of target able to overcome the numerous drawbacks of foil targets: A cluster jet. A cluster jet is formed by pressing pre-cooled gas (e.g. hydrogen) through a very narrow Laval nozzle ( $d_N = 42 \mu\text{m}$ ). Thereby, the gas atoms cool down further by an adiabatic expansion and they may form clusters of  $10^2 - 10^6$  atoms only loosely bound by the Van der Waals force. The constant flow of target material and the high velocity of the clusters (up to 800 m/s [Täs12]) enable a very high repetition rate. The use of hydrogen as a target material prevents any debris and enables the acceleration of a single ion species. The mass limited target clusters prevent any transversal energy loss and the acceleration mechanism changes to a Coulomb explosion. Therefore only a fraction of the currently available laser intensity is needed ( $\sim 10^{16} \text{ W/cm}^2$ ) resulting in a very large effective interaction volume which improves the shot-to-shot stability drastically. While the overall density of a cluster jet is usually in the range of  $10^{15} - 10^{17} \text{ atoms/cm}^3$ , the density inside of the single clusters is comparable with solids. Usually, cluster jets are used as internal targets at conventional accelerators (e.g. in COSY11, ANKE@COSY or the future  $\bar{\text{P}}\text{ANDA}$  experiment), but in 1996 Ditmire [D<sup>+</sup>96] started to investigate the laser-cluster interaction. Since then laser intensities and cluster jets have made huge improvements. In the scope of this work a new cluster source is built and characterised. This is presented in chapter 3. The new

---

cluster source is able to operate in a previously uninvestigated parameter regime using lower temperatures than before and even liquid hydrogen for the cluster process.

During precursor measurements [Gri18, A<sup>+</sup>19] with an unoptimised cluster source [Gri14, G<sup>+</sup>19] the Balmer spectral lines of the generated plasma were observed and the plasma temperature was estimated. Accelerated protons were detected under different angles identifying the acceleration process as a Coulomb explosion. A very promising shot-to-shot stability was shown. The highest measured proton energy was 88(15) keV [Gri18] and a strong increase of the proton energy for lower temperatures of the cluster source was found. In addition, the generated X-ray radiation and accelerated electrons in laser forward direction were detected.

This thesis will give an overview of the theoretical description of the interaction of a short laser pulse of high intensity with a cluster jet target in chapter 2, starting from the interaction of a strong electromagnetic field with a single electron and ending with the concrete proton acceleration mechanism. Afterwards, the newly built cluster source is presented in chapter 3. This includes the working principle, the design and the hardware as well as the characterisation using interferometry, Mie scattering and shadowgraphy. Chapter 4 introduces the ARCTURUS laser system of the Heinrich Heine Universität Düsseldorf, which was used for the experiments. Finally, in chapter 5 the data taken concerning accelerated protons and electrons are presented. To accomplish this the experimental setup and the detector used are shown and the newly developed evaluation routine is presented, including a detailed handling of the systematic uncertainties. Concluding this thesis, chapter 6 shows the measurements concerning generated X-ray radiation. Again, the experimental setup, the detector used and the evaluation routine for the data taken are presented.



## 2 Laser-matter interaction

Since the invention of chirped pulse amplification (CPA) in 1985 the available laser intensity has risen by several orders of magnitude [Gib05]. This opens a comparably easy way to investigate the interaction of strong electromagnetic fields with different states of matter and the plasmas generated thereby. Scientific interest in this matter refers not only to the understanding of the fundamental interaction, but especially to future applications using the electrons and ions, accelerated in the process, or the X-ray radiation generated.

This chapter gives a step-by-step description of the physical interaction of high-intensity lasers with matter, starting with the interaction of strong electromagnetic fields with a single atom or a single electron and resulting in acceleration mechanics for ions.

### 2.1 Single atom-laser interaction

A high-intensity laser pulse with propagation direction  $\vec{e}_z$  and linear polarization in  $\vec{e}_y$  direction can be described as an oscillating electromagnetic wave with the vector potential

$$\vec{A}_L(z, t) = \vec{e}_y A_0 \sin(k_L z - \omega_L t) . \quad (2.1.1)$$

This plane wave laser pulse has an amplitude of  $A_0$ , a laser frequency of  $\omega_L/2\pi$  and a wave number of  $k_L = 2\pi n_r/\lambda_L$  with the refractive index  $n_r$  and the laser wavelength  $\lambda_L$ . The electric field  $\vec{E}_L$  and the magnetic field  $\vec{B}_L$  of the laser pulse can be derived from the vector potential [Mes04a]:

$$\vec{E}_L = -\frac{\partial \vec{A}_L}{\partial t} = \vec{E}_0 \cos(k_L z - \omega_L t) = \vec{e}_y \omega_L A_0 \cos(k_L z - \omega_L t) \quad (2.1.2)$$

$$\vec{B}_L = \vec{\nabla} \times \vec{A}_L = \vec{B}_0 \cos(k_L z - \omega_L t) = \vec{e}_x \frac{n_r}{c} E_0 \cos(k_L z - \omega_L t) \quad (2.1.3)$$

Therein  $c = \frac{1}{\sqrt{\mu_0 \epsilon_0}} = \frac{\omega_L}{2\pi} \lambda_L$  is the speed of light in vacuum with the dielectric constant  $\mu_0$  and vacuum permittivity  $\epsilon_0$ . The laser intensity  $I_L$  is the absolute value of the Poynting vector  $\vec{S} = \vec{E} \times \vec{B}/\mu_0$  averaged over a laser period indicated by the angle brackets  $\langle \rangle$  [Mes04a]

$$I_L = \langle |\vec{S}| \rangle = \frac{1}{\mu_0} \langle |\vec{E}_L \times \vec{B}_L| \rangle = \frac{\epsilon_0 c E_0^2}{2}. \quad (2.1.4)$$

Since the energy of the single laser photons is not high enough for a direct ionisation of the atoms via the photo effect, the ionisation is caused by the interaction of the electromagnetic laser field and the binding field of the atom. The laser intensity has to exceed the atomic binding intensity  $I_a$  between an atomic nucleus and its electron to ionise the atom by negating the binding field. For an estimation of the laser intensity necessary for an atomic ionisation, a hydrogen atom is considered. Using the Bohr radius

$$a_B = \frac{4\pi\epsilon_0 \hbar^2}{m_e e^2} = 5.3 \times 10^{-9} \text{ cm}, \quad (2.1.5)$$

with the reduced Planck constant  $\hbar$ , as the distance between atomic nucleus and electron, the atomic binding field strength for the hydrogen atom is [Gib05]



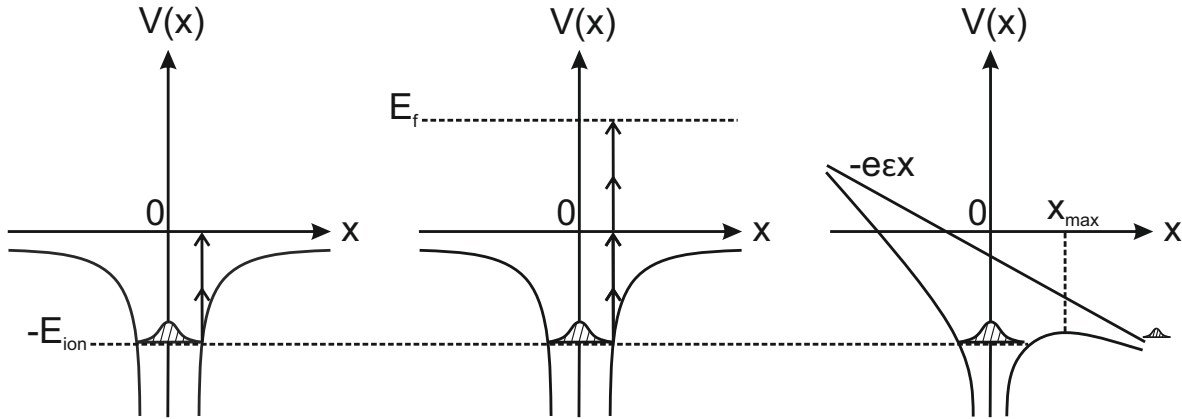


**Figure 2.1** – The left side shows the principle of multi photon ionisation (MPI): Multiple (here two) photons are absorbed simultaneously to match the ionisation energy  $E_{\text{ion}}$ . The center shows the case of above threshold ionisation (ATI), where even more photons are absorbed resulting in a higher kinetic energy  $E_f$  of the ionised electron. The right side shows the influence of a strong electric field on the binding potential leading to tunnel ionisation. Image taken from [Gib05], edited.

$$E_a = \frac{e}{4\pi\epsilon_0 a_B^2} \cong 5.1 \times 10^7 \frac{\text{V}}{\text{cm}} . \quad (2.1.6)$$

This results in an atomic binding intensity and thus a lower limit for the laser intensity for the ionisation of the atom of [Gib05]

$$I_a = \frac{\epsilon_0 c E_a^2}{2} \cong 3.51 \times 10^{16} \frac{\text{W}}{\text{cm}^2} . \quad (2.1.7)$$

However, a lower laser intensity is already sufficient for the ionisation of atoms, because of the two following mechanisms. The first one is the multi photon ionisation (MPI) and uses the particle concept. While the energy of a single laser photon is not sufficient to ionise the atom, multiple ( $n$ ) photons may be absorbed by the electron at once. This is possible for high photon densities corresponding to laser intensities  $> 10^{10} \text{ W/cm}^2$  [Gib05]. It is possible that more than the  $n$  necessary photons are absorbed simultaneously. This is called Above Threshold Ionisation (ATI). Figure 2.1 shows a sketch of MPI on the left

side and a sketch of ATI in the centre. With  $s$  additionally absorbed photons the kinetic energy of the ionised electron is

$$E_e = (n + s)\hbar\omega_L - E_{\text{ion}} \quad (2.1.8)$$

with the ionisation energy  $E_{\text{ion}}$ . For even stronger laser intensities the second mechanism, tunneling ionisation, kicks in. In this regime the electric field of the laser has become strong enough to influence the atomic binding potential to

$$V(x) = -\frac{Ze^2}{x} - e\epsilon x \quad (2.1.9)$$

with the atomic number  $Z$  and the absolute permittivity  $\epsilon$  [Gib05]. The right side of figure 2.1 shows a sketch of the resulting potential. The new potential wall is low enough for the electrons to leave the atoms by tunneling through the binding potential. A laser intensity of  $I_{\text{app}} \cong 1.4 \times 10^{14} \text{ Wcm}^{-2}$  [Gib05] is necessary for the ionisation of hydrogen atoms. A separation factor for the two mechanisms

$$\alpha = \omega_L \sqrt{\frac{2E_{\text{ion}}}{I_L}} \quad (2.1.10)$$

can be introduced [Gib05]. For  $\alpha > 1$  MPI and ATI dominate, but with stronger laser intensities resulting in  $\alpha < 1$  tunneling ionisation becomes the leading process.

## 2.2 Electron-laser interaction

Once separated from the ions, the electrons start to move in the electromagnetic field of the laser pulse. This is described by the Lorentz force and the energy equation

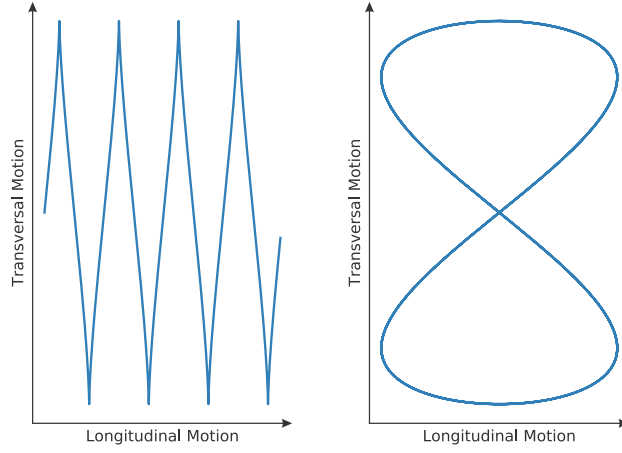


**Figure 2.2** – Motion of relativistic electrons in the electric field of a plane wave laser. On the left side the motion is shown in the laboratory frame and on the right side the same motion is depicted in the average rest frame [Man19].

$$\vec{F}_L = \frac{d\vec{p}}{dt} = \frac{d}{dt}\gamma m\vec{v} = -e \left( \vec{E}_L + \frac{1}{c}\vec{v} \times \vec{B}_L \right) \quad (2.2.1)$$

$$\text{and} \quad \frac{d}{dt}(\gamma mc^2) = -e(\vec{v} \cdot \vec{E}_L) \quad (2.2.2)$$

using the electron velocity  $\vec{v}$ , the electron mass  $m$ , the speed of light in vacuum  $c$  and the relativistic Lorentz factor of the electron  $\gamma$  [Gib05]. For a laser as described with formula 2.1.1 the electron motion results in

$$y = -\frac{a_0 c}{\omega_L} \sin \phi \quad (2.2.3)$$

$$z = \frac{a_0^2 c}{4\omega_L} \left( \phi + \frac{1}{2} \sin 2\phi \right) \quad (2.2.4)$$

with the relativistic laser amplitude  $a_0 > 1$  and the laser phase  $\phi$  [Gib05]. These equations of motions are depicted in figure 2.2. The motion is, evaluated in the laboratory frame, an oscillation transverse to the laser propagation direction and a drift parallel to it. The motions turns into a figure of eight in the average rest frame.

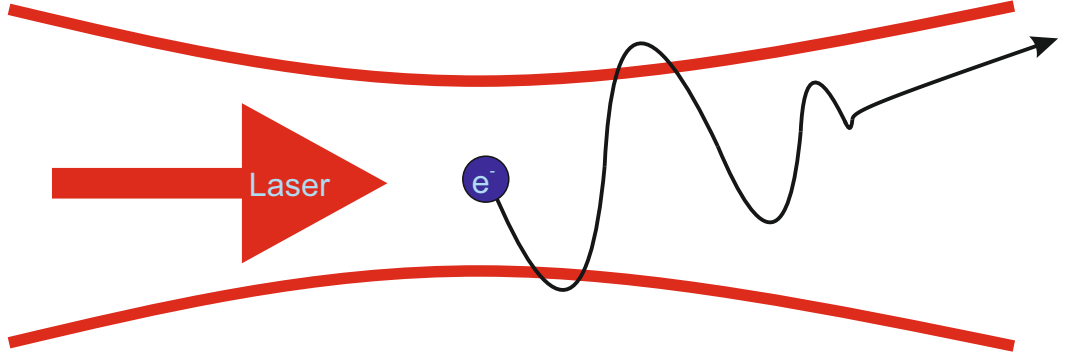


**Figure 2.3** – Schematic view of the relativistic electron motion in a focused laser pulse. The electrons show an oscillation in the polarisation plane of the laser combined with a drift in the laser propagation direction and leave the laser focus due to the ponderomotive force [Man19] (based on [Gib05]).

Since focused laser pulses show strong gradients in time and space, they are not plane waves and another kind of force has to be considered. The ponderomotive force

$$\vec{F}_{\text{pond}} = -\frac{e^2}{4m\omega_L^2\bar{\gamma}}\vec{\nabla}\left(\vec{E}_L^2(x)\right) \quad (2.2.5)$$

using  $\bar{\gamma} = \sqrt{1 + a_0^2}$  takes this into account and acts in the direction of the electric field gradient [Gib05]. The electrons are therefore pushed out of the laser focus where the laser intensity is at maximum. This results in an electron motion as shown in figure 2.3. The electrons show their usual oscillation combined with a strong drift in laser propagation direction and leave the laser focus under the angle  $\theta$  relative to the laser propagation direction.

### Laser wakefield acceleration

The forces mentioned beforehand, namely the Lorentz force and the ponderomotive force, also act on the ionised atomic nuclei. However, the mass of atomic nuclei is at least a factor  $m_p/m_e \approx 1836$  higher than the electron mass, reducing the effective motion caused by the laser pulse to an insignificant order. While the ions stay at their initial positions during the laser target interaction, the electrons are accelerated by the ponderomotive

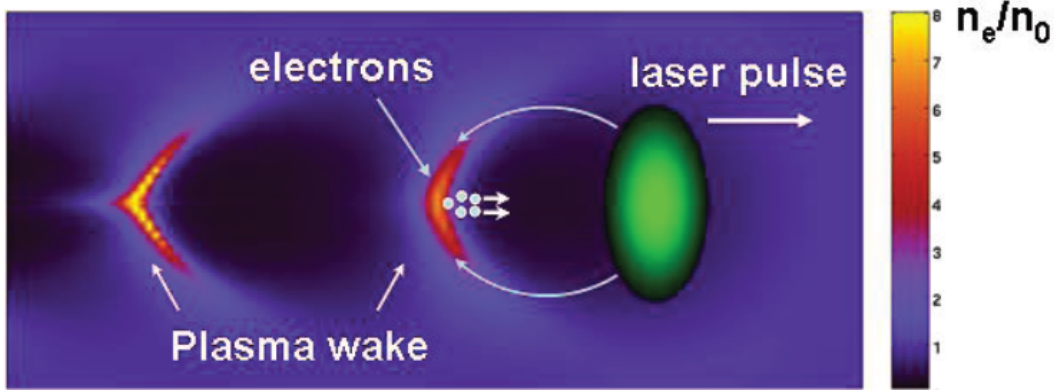


**Figure 2.4** – Schematic view of the laser wakefield acceleration. The color scale represents the electron density. Nearly electron free bubbles can be seen behind the propagating laser pulse separated by electron bunches. Only a few electrons are injected into the bubbles and accelerated as indicated by the white arrows [M<sup>+</sup>13].

force causing a charge separation moving behind the laser pulse through the target medium. Directly behind the propagating laser pulse a bubble free of electrons is formed as long as the laser intensity is high enough [M<sup>+</sup>08]. The electrons which occupied this area before move along the surface of the bubble to its rear side while some of the electrons are injected into the bubble. This injection is highly dependent on the plasma density, the plasma density structure and the initial positions of the electrons with regard to the incoming laser pulse. In general, higher densities and initial positions close to the laser propagation axis result in a higher injection rate [M<sup>+</sup>13]. The electron motion results in a strong charge separation between the bubble (positive from the stationary ions) and the region at the rear side of the bubble where most of the electrons accumulate. Once the force of this charge separation exceeds the ponderomotive force, the electrons oscillate with the plasma frequency  $\omega_P = \sqrt{\frac{n_e e^2}{\epsilon_0 m_e}}$  while following the propagation of the laser pulse through the plasma [M<sup>+</sup>13]. Figure 2.4 illustrates this process. The electrons injected into the bubble are accelerated by the charge separation and may even become faster than the laser pulse in the medium. These electrons reach the centre of the bubble where the electric field strength of the charge separation changes the direction. Depending on the laser pulse parameters and the target density, energies up to the GeV scale were already achieved [M<sup>+</sup>13], while the typical energy range is in the order of 10 MeV. The indirect acceleration of ions caused by macroscopic charge separation is discussed in the next section.

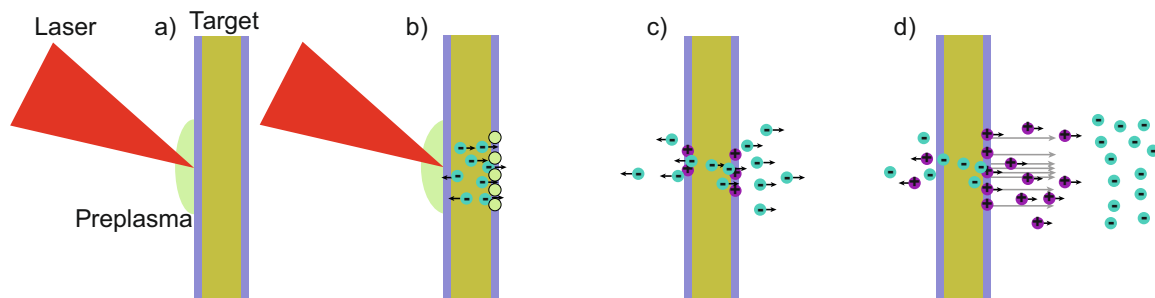


**Figure 2.5** – Step by step view of target normal sheath acceleration (TNSA). a) shows the formation of a pre-plasma while the pre-pulse of the laser hits the target. In b) the main laser pulse arrives at the target and heats the electrons. Most of the hot electrons are pushed to the rear surface of the target and leave it as shown in c). This leads to a charge separation between ions and electrons, resulting in a strong electric field (indicated as grey arrows in d)) which in turn accelerates the ions normal to the target [Sch18].

## 2.3 Proton acceleration mechanisms

### Target Normal Sheet Acceleration

The most common laser induced acceleration mechanism for ions is the Target Normal Sheet Acceleration (TNSA). Figure 2.5 shows the process with a thin foil target. First, the laser pre-pulse generates a pre-plasma at the surface of the target. Then the main laser pulse interacts with this pre-plasma and heats the electrons of the target material. These hot electrons may now leave their original position and even the whole target at the rear side [Sch08]. This is leading to a charge separation, since the positively charged ions are too massive to move on the same time scale. The charge separation in turn generates an electric field of very high field strength which then accelerates the ions normal to the target surface.

Although ion energies typically reached with TNSA and thin foil targets are in the range of 50 MeV [S<sup>+</sup>00], the approach has some fundamental drawbacks. A fraction of the hot electrons may escape from the plasma through the solid target orthogonal to the laser propagation direction reducing the accelerating electric field strength. In addition, the plasma generated causes a hole in the foil, leaving it unsuitable for another interaction at the same spot. Even with tape targets, which can be moved between

shots, the repetition rate is very limited. Not all of the target material blown away by the laser pulse is part of the generated plasma. Some amount simply fractures off the foil as debris and may damage optical components in the interaction chamber. Since foils are usually not made of a single ion species but of at least two (e.g.  $CH$ ), different ion species are accelerated at once, complicating the extraction of particular ions.

Many of these drawbacks can be circumvented by using a cluster jet target instead of a foil. A cluster jet delivers a constant flow of mass limited target material with high speed of several hundred m/s, enabling high repetition rates and preventing a transversal loss of electrons. The target material is made of a single species (usually  $H_2$ ) and any possible debris just vaporises. However, the acceleration mechanism changes. For the interaction of a short laser pulse with a cluster, which is defined as a loose formation of approximately  $100 - 10^6$  particles bound only by the van der Waals force, the Coulomb explosion is the dominant mechanism and will be described in more detail hereinafter.

### Coulomb explosion

The interaction of a short laser pulse with a cluster of atoms is essentially an interaction of the electromagnetic field with the bound electrons. A sketch of the interaction is shown in figure 2.6. The laser pulse heats the electrons of the cluster to relativistic kinetic energies of

$$E_{\text{kin,e}} = \sqrt{m_e^2 c^4 + p_{\parallel}^2 c^2 + p_{\perp}^2 c^2} - m_e c^2 \quad (2.3.1)$$

with the two momenta parts  $p_{\parallel} = m_e c a_0^2 / 2$  and  $p_{\perp} = m_e c a_0$ , the electron mass  $m_e$  and the normalised laser amplitude  $a_0$  [N<sup>+</sup>01]. The kinetic energy of the electrons is related to the electrostatic potential of the ions as [S<sup>+</sup>04]

$$E_{\text{kin,e}} = p_{\parallel} c + e\phi \quad (2.3.2)$$

with the electrostatic potential of the ions

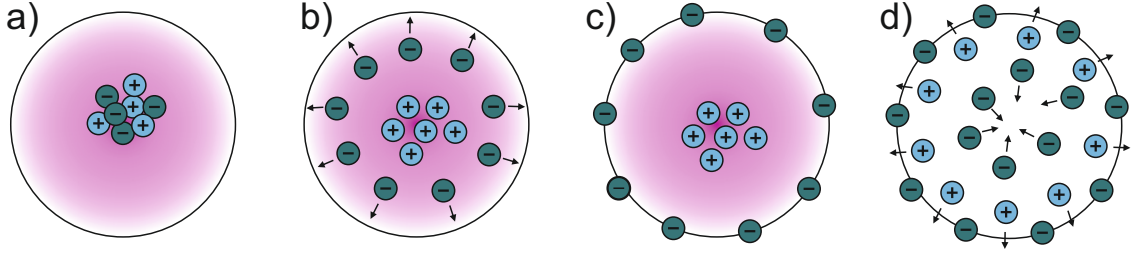


**Figure 2.6** – Sketch of the Coulomb explosion of a cluster. The time scale is from left to right or from a) to d), respectively. In a) the cluster is hit by the laser pulse (purple background). The laser pulse ionises the cluster in b) resulting in a positively charged proton cluster and separated electrons as shown in c). In d) the laser pulse has passed the cluster and the ions drift apart due to the Coulomb repulsion [Sch18].

$$\phi(r) = \frac{Ne}{4\pi\epsilon_0 R} \left( \frac{3}{2} - \frac{r^2}{2R^2} \right). \quad (2.3.3)$$

Therein  $e$  is the elementary charge,  $R$  is the radius of the cluster,  $N = \frac{4}{3}\pi R^3 n$  is the number of ions in the cluster and  $n$  is the particle density in the cluster. The electrons leave the cluster once their kinetic energy is much bigger than the binding energy to the ions [N<sup>+</sup>01]

$$E_{\text{kin,e}} \approx \frac{m_e c^2 a_0^2}{2} \gg e\phi_{\text{max}} = \frac{e^2 n R^2}{3\epsilon_0}. \quad (2.3.4)$$

This defines the minimal laser amplitude necessary

$$a_0 = \frac{eE}{m_e \omega_L c} > \left( \frac{2e^2 n}{3\epsilon_0 m_e c^2} \right)^{1/2} R \quad (2.3.5)$$

to remove all electrons from the cluster in  $t = 2R/c \ll \tau$ , with the laser pulse duration  $\tau$  [S<sup>+</sup>04]. This leaves a highly charged cluster of positive ions starting to drift apart because of the Coulomb repulsion in a pico second time scale. Ions closer to the surface



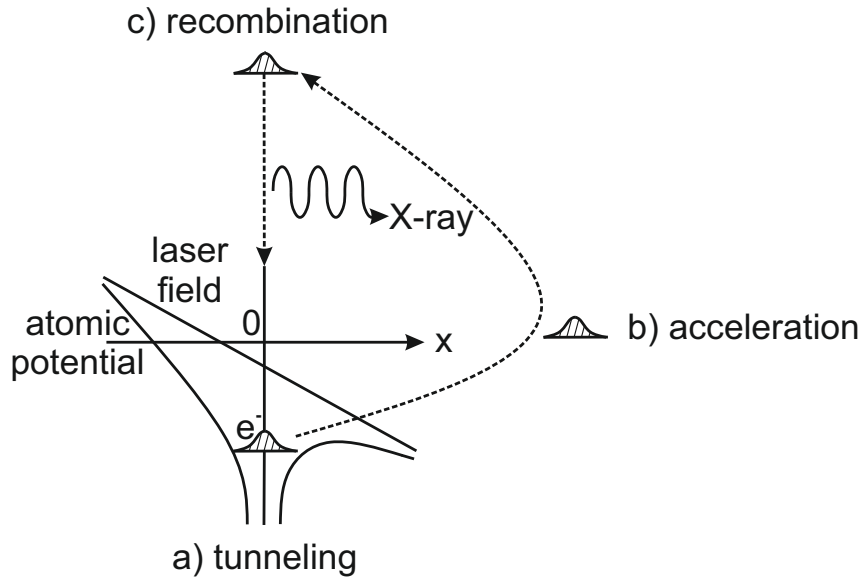


**Figure 2.7** – Principle of higher harmonic generation. In a) atoms are ionised by tunnel ionisation as shown in figure 2.1. The free electrons are then accelerated by the laser field in b) and may recombine with the atomic nucleus while emitting X-ray radiation in c) [Gri18] based on [DPM15].

have higher potential energy which will be transformed to kinetic energy by the Coulomb explosion. The maximal possible ion energy is given for ions at the surface ( $r = R$ )

$$E_{\max} = \frac{Ne^2}{4\pi\epsilon_0 R}. \quad (2.3.6)$$

## 2.4 X-ray generation mechanisms

Similar to proton acceleration, the generation of X-ray radiation in the laser-cluster interaction is dependent on the laser-electron interaction. After ionising the atoms as discussed in section 2.1 the electrons are accelerated by the laser field as discussed in section 2.2. The figure of eight motion brings the electrons back to the positively charged ions where they may recombine under X-ray emission [Gib05]. This process is called Higher Harmonics Generation and is shown in figure 2.7.

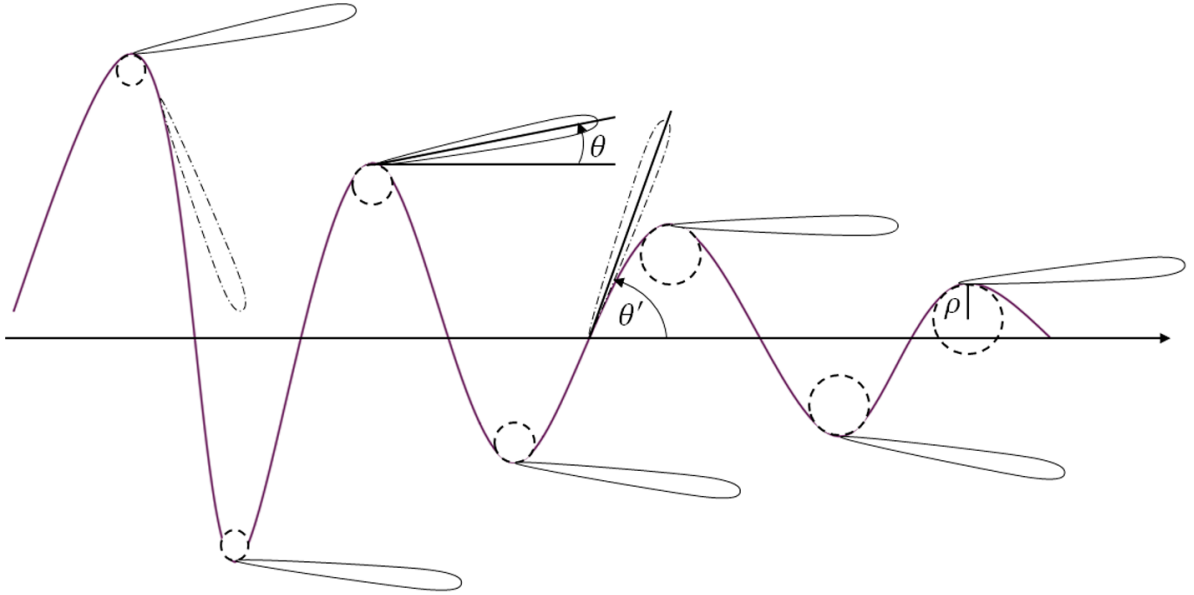


**Figure 2.8** – Two dimensional sketch of the generation of betatron radiation. An electron oscillating in the electric field of the stationary ions emits X-ray radiation at every turning point of its oscillation under an angle  $\theta$  with respect to the electrons drift direction [PP17].

Simultaneously, another mechanism produces X-ray radiation. Once ionised, the electrons perform a figure of eight movement (cf. section 2.2) in the potential of the stationary ions with a frequency called betatron frequency

$$\omega_b = \frac{\omega_P}{\sqrt{2\gamma}} \quad (2.4.1)$$

with the plasma frequency  $\omega_P = \sqrt{\frac{n_e e^2}{\epsilon_0 m_e}}$  and the Lorentz factor  $\gamma$ . X-ray radiation is emitted at each turning point of the electron movement [PP17]. This radiation is called betatron radiation and is a kind of bremsstrahlung similar to synchrotron radiation. Figure 2.8 shows a two dimensional sketch of this process.

A single electron of Lorentz factor  $\gamma$  emits for  $\theta\gamma \gg 1$  and in the asymptotic limit a synchrotron-like spectrum

$$\frac{d^2 I}{d\Omega d\omega} = \frac{e^2}{3\pi^2 c} \left(\frac{\omega\rho}{c}\right)^2 \left(\frac{1}{\gamma^2} + \theta^2\right) \left[ K_{2/3}^2(\zeta) + \frac{\theta^2}{(1/\gamma^2) + \theta^2} K_{1/3}^2(\zeta) \right] \quad (2.4.2)$$

with  $\zeta = \frac{\omega\rho}{3c}(1/\gamma^2 + \theta^2)^{3/2}$ , the observation angle  $\theta$ , the radius of curvature of the electron trajectory  $\rho$ , the frequency of the emitted radiation  $\omega$  and the modified Bessel functions  $K_{1/3}$  and  $K_{2/3}$  [PP17]. This means X-rays with a wide energy spectrum are generated in laser forward direction with only a small divergence.



## 3 Cryogenic cluster jet targets

Cryogenic cluster jet targets are widely used in nuclear and particle physics as internal targets at particle accelerators. Their combination of medium density ( $10^{15} - 10^{19} \text{ cm}^{-3}$ ), constant flow of target material and stability over very long time scales makes them very good candidates for internal targets. Since 1996 [D<sup>+</sup>96], cluster jet targets have been used in plasma physics as well. Especially the debris-free character of cluster jet targets and the possibility for high repetition rates are greatly appreciated. This chapter contains an explanation of the working principle of cluster jet targets, introduces the Münster Cluster Jet Target for Düsseldorf (MCT-D) and shows its characterisation.

### 3.1 Working principle and gas flow theory

The most important part of every cluster jet target is a Laval nozzle, which consists of a convergent inlet zone and a divergent outlet zone. A cluster jet is generated by pressing pre-cooled gas or liquid with a high backing pressure (10 – 20 bar) through the nozzle into a vacuum. This is shown in figure 3.1. The gas accelerates in jet direction while passing through the nozzle, reaching sonic speed at the narrowest section. If the gas is below its inversion temperature, it will cool down further due to the Joule-Thomson effect [NN05] while expanding adiabatically in the divergent outlet. This results in very low relative velocities between the gas atoms and enables the formation of condensation germs by three body collisions. In these interactions two of the atoms are bound together by van der Waals forces while transferring their relative momenta to the third atom. Other atoms may now attach to the condensation germ of already higher mass and form a cluster of atoms. Typical clusters contain between 100 and  $10^6$  particles.

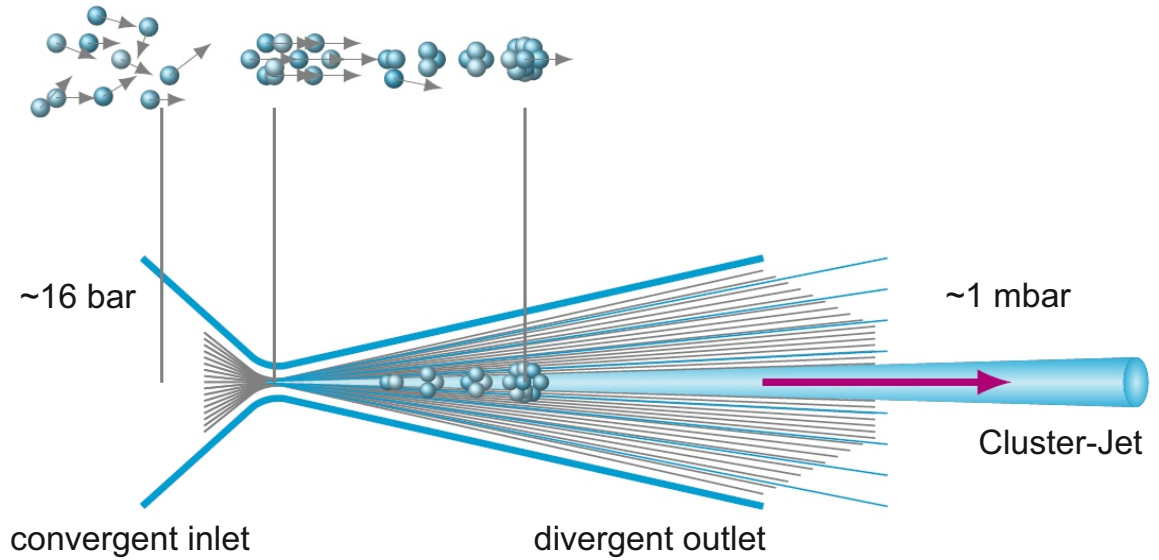


**Figure 3.1** – Schematic view of a Laval nozzle and the clustering process. The pre-cooled gas enters from the left through the convergent inlet zone, is pressed through the narrowest section and leaves the nozzle through the divergent outlet zone. The relative velocities between the gas atoms decrease while passing through the nozzle until three body interactions in the outlet zone may generate cluster condensation germs as shown at the top. Generated by E. Köhler and edited by S. Grieser, edited.

For theoretical calculation of density and gas flow of cluster jet targets a perfect gas can be assumed. Calculations with real gases give better results with a higher precision and for a wider parameter regime [Täs12], but for an estimation of the cluster jet density at stagnation conditions in the gaseous regime the assumption of a perfect gas is sufficient. For perfect gases the ideal gas law

$$pV = nRT \quad (3.1.1)$$

$$c_p - c_V = nR \quad (3.1.2)$$

is valid and the heat capacities  $c_V$  and  $c_p$  are assumed to be constant [NN05]. Thereby  $p$  is the pressure of the gas of volume  $V$ , of temperature  $T$  and with the amount of substance  $n$ .  $R = 8.314456(10) \frac{\text{J}}{\text{molK}}$  [MTN08] is the universal gas constant. In addition

to the ideal gas law, the energy is assumed to be conserved

$$h_0 + \frac{v_0^2}{2} = h + \frac{v^2}{2} \quad (3.1.3)$$

with the current and reference velocities  $v$  and  $v_0$  and the current and reference enthalpies  $h$  and  $h_0$ . The reference point is chosen to be upstream of the nozzle, where the gas is approximately at rest ( $v_0 = 0$ ). The current velocity can be calculated with the perfect gas equation for the enthalpy

$$c_p = \frac{\kappa}{\kappa - 1} \frac{R}{M} \quad (3.1.4)$$

$$h = c_p T \quad (3.1.5)$$

$$= \frac{\kappa}{\kappa - 1} \frac{R}{M} T \quad (3.1.6)$$

$$h_0 = \frac{\kappa}{\kappa - 1} \frac{R}{M} T_0 \quad (3.1.7)$$

where  $M$  is the molar mass of the gas and  $\kappa = \frac{c_p}{c_v} = \frac{Z+2}{Z}$  [Dem09] is the heat capacity ratio with the number of degrees of freedom  $Z$ . Since the gas cools down while passing the nozzle, the temperature downstream of the nozzle  $T$  can be neglected compared to the gas temperature upstream of the nozzle  $T_0$ . Using  $T \approx 0$  and the equations 3.1.6 and 3.1.7 leads from equation 3.1.3 to an approximation of the gas and cluster velocity:

$$v = \sqrt{2c_p(T_0 - T)} \quad (3.1.8)$$

$$\approx \sqrt{\frac{2\kappa}{\kappa - 1} \frac{RT_0}{M}} \quad (3.1.9)$$

This describes measurements of the cluster velocity in the gaseous regime quite well [Täs12], but results in a huge discrepancy at liquid stagnation conditions. The measured cluster velocities drop strongly at the phase transition from gaseous to liquid which is

not included in calculations with a perfect gas.

The mass flow  $\dot{m}$  through the nozzle outlet or through the narrowest sectional area (marked by \*) can be written as the product of their respective densities ( $\rho, \rho^*$ ), velocities ( $v, v^*$ ) and sectional areas ( $A, A^*$ )

$$\dot{m} = A\rho v \quad (3.1.10)$$

$$\text{and } \dot{m}^* = A^*\rho^*v^* . \quad (3.1.11)$$

Taking the adiabatic flow of the gas into account, one finds  $\rho^* = \rho_0 \left(\frac{2}{\kappa+1}\right)^{1/(\kappa-1)}$  with the density upstream of the nozzle  $\rho_0 = \frac{p_0 M}{RT_0}$  and  $v^* = \sqrt{\frac{2\kappa RT_0}{(\kappa+1)M}}$  [Täs12]. This can be used to rewrite

$$\dot{m}^* = A^*\rho^*v^* \quad (3.1.12)$$

$$= A^*\rho_0 \left(\frac{2}{\kappa+1}\right)^{\frac{1}{\kappa-1}} \sqrt{\frac{2\kappa}{\kappa+1} \frac{RT_0}{M}} \quad (3.1.13)$$

$$= A^*p_0 \sqrt{\kappa \frac{M}{RT_0}} \left(\frac{2}{\kappa+1}\right)^{\frac{\kappa+1}{2(\kappa-1)}} . \quad (3.1.14)$$

Since there is no matter lost in the nozzle, the two mass flows should be equal  $\dot{m} = \dot{m}^*$ . This gives a formula for the density of the cluster jet at the nozzle exit

$$\rho_{\text{nozzle exit}} = \frac{A^*p_0}{Av} \sqrt{\frac{M\kappa}{RT_0}} \left(\frac{2}{\kappa+1}\right)^{\frac{\kappa+1}{2(\kappa-1)}} . \quad (3.1.15)$$

However, the cluster velocity  $v$  can only be approximated for stagnation conditions in the gaseous regime. Using the measured volume flow  $q_V$  upstream of the cooling section and the nozzle instead is a more precise way to calculate the density of the cluster jet. It can be written as



$$q_V = \dot{m} \frac{RT_N}{Mp_N} \quad (3.1.16)$$

with the pressure and temperature at normal conditions  $p_N = 1.01325 \text{ bar}$  and  $T_N = 273.15 \text{ K}$ . This leads to the density at the nozzle outlet

$$\rho_{\text{nozzle exit}} = \frac{p_N}{AT_N} \sqrt{\frac{\kappa - 1}{2\kappa} \frac{M^3}{R^3} \frac{q_V}{\sqrt{T_0}}} \quad (3.1.17)$$

Due to the divergent nozzle exit area, the cluster jet has a certain divergence, too. This reduces the density of the jet with the distance to the nozzle. Assuming a ballistic motion of the clusters, the density at an interaction point in distance  $d$  to the nozzle can be approximated by

$$\rho_{\text{interaction point}} = \frac{\rho_{\text{nozzle exit}}}{\left( \frac{2 \tan(\alpha_{1/2})(d+d_i+d_N/(2 \tan(\alpha_{1/2})))}{d_o} \right)^2} \quad (3.1.18)$$

with the distance from the narrowest section to the nozzle outlet  $d_i$ , the narrowest diameter  $d_N$ , the nozzle outlet diameter  $d_o$  and the half opening angle of the divergent nozzle zone  $\alpha_{1/2}$ . This is only valid as an approximation of the expected cluster jet density at short distances  $d$  since E. Köhler [Köh15] already showed that the cluster jet opening angle differs slightly from the opening angle of the nozzle.

### Cluster size estimation for clustering gases

The cluster sizes can be estimated using the empirical Hagena formula. The Hagena parameter

$$\Gamma^* = \frac{\hat{k} (p/\text{mbar}) \left( \frac{0.74 (d_n/\mu\text{m})}{\tan(\alpha_{1/2})} \right)^{0.85}}{(T/\text{K})^{2.29}} \quad (3.1.19)$$

with the gas dependent constant  $\hat{k}(H_2) = 184$  [SDT98] characterises the cluster process [Hag87]. While low values of the Hagedorn parameter  $\Gamma^* < 200$  mean no clustering at all, clusters with more than 100 atoms per cluster are expected for high values  $\Gamma^* > 1000$ . The Hagedorn scaling law can be used to calculate the number of atoms per cluster

$$\bar{N} = A_N \left( \frac{\Gamma^*}{1000} \right)^{\gamma_N} \quad (3.1.20)$$

with the two empirical constants  $A_N = 33$  and  $\gamma_N = 2.35$  for  $\Gamma^* > 1800$  [Hag92]. Since these constants were found for nitrogen and noble gases, a correction for hydrogen to  $A_N(H_2) = 86(3)$  has been suggested by E. Köhler [Köh15]. The average cluster diameter  $d_{\text{Cl.}}$  can be calculated by considering the cluster mass  $M_{\text{Cl.}}$ . The cluster mass can, on the one hand, be written as the product of particle number  $N$  and molar mass  $m$ , and on the other hand as product of volume  $V = \frac{4}{3}\pi \left(\frac{d_{\text{Cl.}}}{2}\right)^3$  and density  $\rho_{\text{Cl.}}$ . The density of the clusters is assumed to be the density of liquid hydrogen  $\rho_{\text{Cl.}} = \rho_\ell = 70.6 \text{ kg/m}^3$ . The cluster diameter can now be calculated by equating these two ways of writing the cluster mass and rearrange the resulting equation:

$$M_{\text{Cl.}} = Nm = \frac{4}{3}\pi \left(\frac{d_{\text{Cl.}}}{2}\right)^3 \rho_{\text{Cl.}} \quad (3.1.21)$$

$$\Leftrightarrow d_{\text{Cl.}} = 2 \left(\frac{3mN}{4\pi\rho_{\text{Cl.}}}\right)^{1/3} \quad (3.1.22)$$

### Cluster size estimation for clustering liquids

Pressing liquids through a narrow nozzle is characterised by the dimensionless Weber number

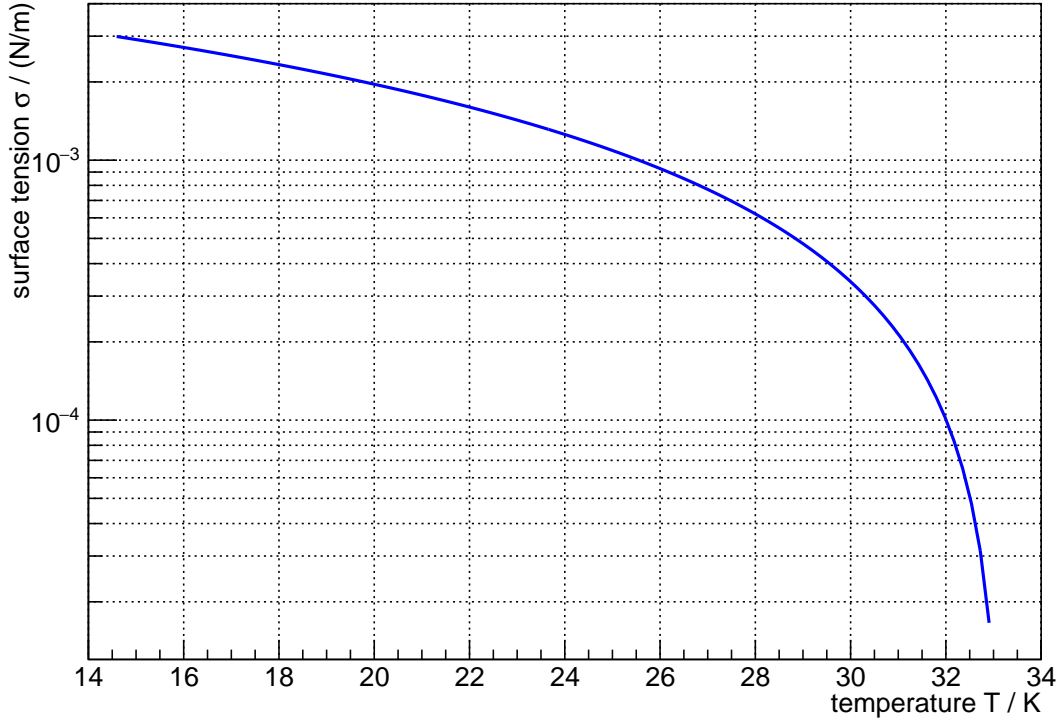


**Figure 3.2** – Surface tension of hydrogen  $\sigma(T) = \sigma_0(1 - T/T_C)^n$  over temperature with  $\sigma_0 = 0.0061$  N/m and  $n = 1.23$  as found in [BP66] and with the critical temperature  $T_C = 33.18$  K.

$$We = \frac{\rho_{Cl}.v^2L}{\sigma(T)} \quad (3.1.23)$$

with the temperature dependent surface tension  $\sigma(T)$  (cf. figure 3.2) and a characteristic length of the system  $L$  for which the narrowest inner diameter of the Laval nozzle was used [LM17]. The Weber number is the ratio of inertial to surface tension forces. Thus low Weber numbers indicate the formation of drops as used in droplet targets (cf. [Har19]), while large Weber numbers indicate an atomisation of the liquid. C.C. Miesse found the transition to atomisation at  $We_{Atomisation} > 245$  [Mie55]. The cluster jet target used in the scope of this work (cf. section 3.2) operates at typical Weber numbers of  $We \approx 570000 \gg We_{Atomisation}$  using the density of liquid hydrogen  $\rho_{Cl.} = 76.3$  kg/m<sup>3</sup>, the narrowest inner diameter of the nozzle used

$L = d_N = 42 \mu\text{m}$ , the surface tension  $\sigma(28 \text{ K}) = 6.2(6) \times 10^{-4} \text{ N/m}$  and the cluster velocity  $v(16 \text{ bar}, 28 \text{ K}) = 332(17) \text{ m/s}$  [Täs12] at typical operation parameters. This indicates a very turbulent flow and an atomisation of the liquid.

Although the atomisation process is not fully understood yet, two sub-processes can be described quite well. The first process is the atomisation by pressure gradient along the nozzle. The pressure gradient leads to a change in the capillary pressure, which in turn leads to Kelvin-Helmholtz instabilities in the fluid. These instabilities cause a breakup of the fluid into small droplets with a maximum possible diameter of [Mes04b]

$$d_{\text{max,p}} = 2\sqrt{\frac{\sigma(T)}{\Delta p}}. \quad (3.1.24)$$

Therein  $\Delta p = 0.89 \text{ bar/mm}$  is the pressure gradient along the nozzle, which corresponds to a drop of pressure from  $p_0 = 16 \text{ bar}$  to  $p_{\text{ic}} = 1 \text{ mbar}$  over the length of the nozzle  $\ell_{\text{nozzle}} = 18 \text{ mm}$ . The pressure downstream of the nozzle results from the flow of hydrogen through the nozzle in combination with the vacuum pumping system presented in section 3.2.

The second process is the atomisation by the aerodynamic force of the surrounding medium in which the liquid expands and therefore takes place after the primary breakup. The liquid drops leaving the nozzle shatter on the surrounding gas molecules into even smaller pieces. This process restricts the maximum possible droplet or cluster diameter to [Mes04b]

$$d_{\text{max,A}} = \frac{8\sigma(T)}{c_w \rho_{\text{ic}} v^2} \quad (3.1.25)$$

with the drag coefficient of a sphere  $c_w = 0.45$  and the gas density downstream of the nozzle  $\rho_{\text{ic}} = 8(1) \times 10^{-5} \text{ kg/m}^3$ , which corresponds to a pressure of  $p_{\text{ic}} = 1 \text{ mbar}$  of

hydrogen.

To identify the leading sub-process, both maximum possible cluster diameters are calculated for the same typical operation parameters already used beforehand. The breakup due to aerodynamic forces limits the cluster sizes to below  $d_{\max,A} = 1.25(24)$  mm while the breakup due to the pressure gradient already sets a limit at  $d_{\max,P} = 5.28(26)$   $\mu\text{m}$ . This shows that the aerodynamic forces can be neglected for the setup used, because the corresponding size limit is three orders of magnitude higher than the limit set by the primary breakup process.

## 3.2 The MCT-D

To realise the cluster process mentioned beforehand (c.f. section 3.1), a new cluster source was built. The Münster Cluster Jet Target for Düsseldorf (MCT-D) was built especially for the operation at the ARCTURUS laser system of the University of Düsseldorf and for research concerning laser cluster interaction. Previous measurements [Gri18, G<sup>+</sup>19, A<sup>+</sup>19] influenced the design of the MCT-D as they verified the physical process of the proton acceleration as a Coulomb explosion and found a strong increase of proton energy with lower temperature. A schematic sketch of the MCT-D can be found in figure 3.3.

The hydrogen gas used for the cluster process is required to have several characteristics: A high pressure of above 10 bar, a low temperature of below 34 K and a very high purity. The purity is necessary to prevent clogging of the narrow nozzle ( $d_{\min} = 42$   $\mu\text{m}$ ), because nearly every impurity in the gas freezes at the operation temperature sealing the nozzle. In order to reach the required purity only hydrogen bottles with a purity of 99.999% were used. In addition, a chemical purifier cartridge in the hydrogen supply line reduced all impurities except for nitrogen to less than 100 parts per trillion (ppt). The exact specification of the purification cartridge and most of the hardware concerning the MCT-D gas system can be found in table 3.1.

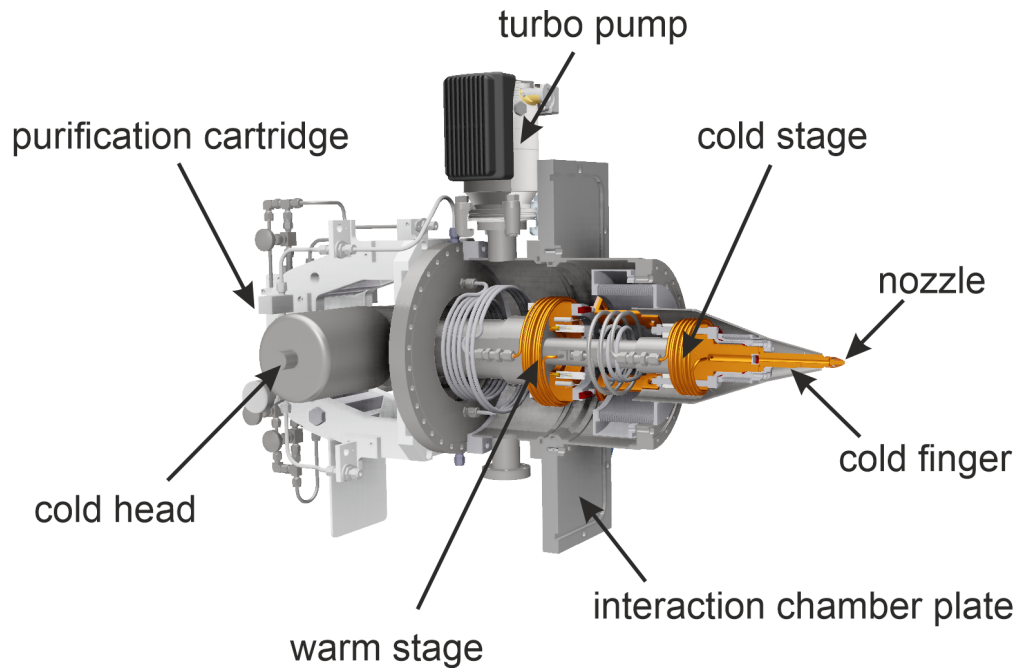


**Figure 3.3** – Schematic view of MCT-D. The gas enters the cluster source from the backside after passing through the purification cartridge, the pressure controller and the flow meter. Afterwards it is pre-cooled at the warm stage and reaches operation temperature at the cold stage. The cooled gas or liquid is then pressed through the nozzle generating a cluster jet. Picture generated by D. Veith.

**Table 3.1** – Specifications of the MCT-D hardware used in the gas and cooling system. There are two temperature diodes and two heater cartridges at the warm stage (WS) and at the cold stage (CS), respectively. At any given time one of each is in use and the other in reserve.

component	specification
purification cartridge	SAES MicroTorr 904
cold head	Leybold COOLPOWER 10 MD
compressor	Leybold COOLPAK 6000 H
temperature diodes	Lake Shore DT-670B-MT
heater cartridges CS	Lake Shore HTR-50 (50 $\Omega$ , 50 W)
heater cartridges WS	Lake Shore HTR-25-100 (25 $\Omega$ , 100 W)
flow meter	Brooks SLA 5860
pressure controller	Brooks SLA 5810
baratron	MKS 722B

### Cooling system

The required low temperatures are provided by a two stage cold head in combination with a compressor and closed-loop high-pressure helium circuit. The two stages of the cold head are separated by a displacer, whose movement causes an expansion and compression of the helium in the two volumes leading to a heat exchange with the compressor due to the Gifford-McMahon process. This system is able to reach  $T_{\text{WS}} = 30.0(5)$  K at the first (warm) stage of the cold head and  $T_{\text{CS}} = 10.0(5)$  K at the second (cold) stage after around two and a half hours of cooling time. The temperature is monitored with two temperature diodes per cold head stage. Since the cooling power of the cryostat can only be adjusted very roughly by changing the compression frequency, each stage features two heater cartridges respectively, with 50 W each at the cold stage and 100 W each at the warm stage. A temperature controller (Lake Shore Model 336) regulates the heating power using a proportional integral (PI) controller to reach the desired temperature. The gas pipe is coiled around copper blocks at the two cold head stages. While the gas pipe is made of copper at the two cold head stages, it is made of stainless steel in between and upstream of the warm stage. This decouples the two cold head stages from each other and from the supply pipe due to the low thermal conductivity of stainless steel  $\lambda_{\text{SS}} = 15$  W/(Km) [Kuc94]. Inversely, it ensures good thermal conduction at the two cold head stages due to the high thermal conductivity of copper  $\lambda_{\text{Co}} = 399$  W/(Km) [Kuc94]. Directly connected to the cold stage is a cold finger extending into the interaction vacuum chamber. The cold finger mounts the Laval nozzle, where the clustering process takes place. Measurements with another temperature diode temporary mounted at the tip of the cold finger, as close to the nozzle as possible, showed a temperature difference between cold stage and nozzle of 1.8(2) K at typical operation temperatures. Temperature values in the following chapters are always the temperature of the cold stage, beside of plots and calculation where the nozzle temperature is used.

### Pressure system

The high pressure is realised with two stages. A pressure regulator directly at the gas bottle lowers the filling pressure to an output pressure of 18 – 20 bar and a pressure regulator can be used to tune the pressure at the nozzle between 2 and 16 bar. The

pressure regulator is controlled by a Brooks Model 0254 Secondary Electronics with integrated PI controller. A flow meter measuring the flow of the gas to detect nozzle clogging is controlled by the same model. More details on this can be found in the description of the slow control software below. Next to the regular gas pipe leading to the nozzle, there is another gas pipe leading back from the nozzle following the same coils around the cold head and material changes as the regular gas pipe. This gas pipe leads to a baratron monitoring the actual pressure at the nozzle and further to a pressure release valve. This valve is necessary for the operation with liquid hydrogen at very low temperatures, because the liquid vaporises to gas of very high pressures when the cluster source is heated to temperatures beyond the vapour pressure curve. These high pressures may damage the gas pipes and should be reduced through the pressure release valve immediately. A sketch of the whole gas and cooling system can be found in figure 3.4. Pressure values in the following chapters are always the pressure at the pressure controller while the pressure at the baratron is a few percent lower, beside of plots and calculation where the more accurate baratron pressure is used.

#### **Vacuum system**

The MCT-D features an isolation vacuum chamber enclosing the cryostat. This is necessary, because the very high flow rates using liquid hydrogen of up to  $10 \ell_{\text{N}}/\text{min}$  result in a relatively high pressure ( $\approx 1 \text{ mbar}$ ) in the interaction chamber, despite the powerful roots pumps opposite to the cluster source. This vacuum is insufficient to thermally isolate the cryostat to reach temperatures low enough for a stable operation in the liquid regime. Figure 3.5 shows a cross section of MCT-D with the isolation vacuum chamber highlighted in blue. A conical cold shield thermally connected to the warm stage shields the cold finger from heat radiation. The front of the isolation vacuum chamber is thermally connected to the warm stage, too. Bellows are used to decouple this area from the cold stage and from the rest of the vacuum chamber at room temperature. Since the isolation chamber is pumped by a separate turbo pump combined with a fore pump (c.f. table 3.2), the vacuum is  $p_{\text{IC}} \approx 2 \cdot 10^{-6} \text{ mbar}$  independent of the operation conditions. Only the cold finger and the nozzle protrude into the the interaction chamber and thus into the worse vacuum reducing the effect of the operation conditions on the achievable minimal temperature.



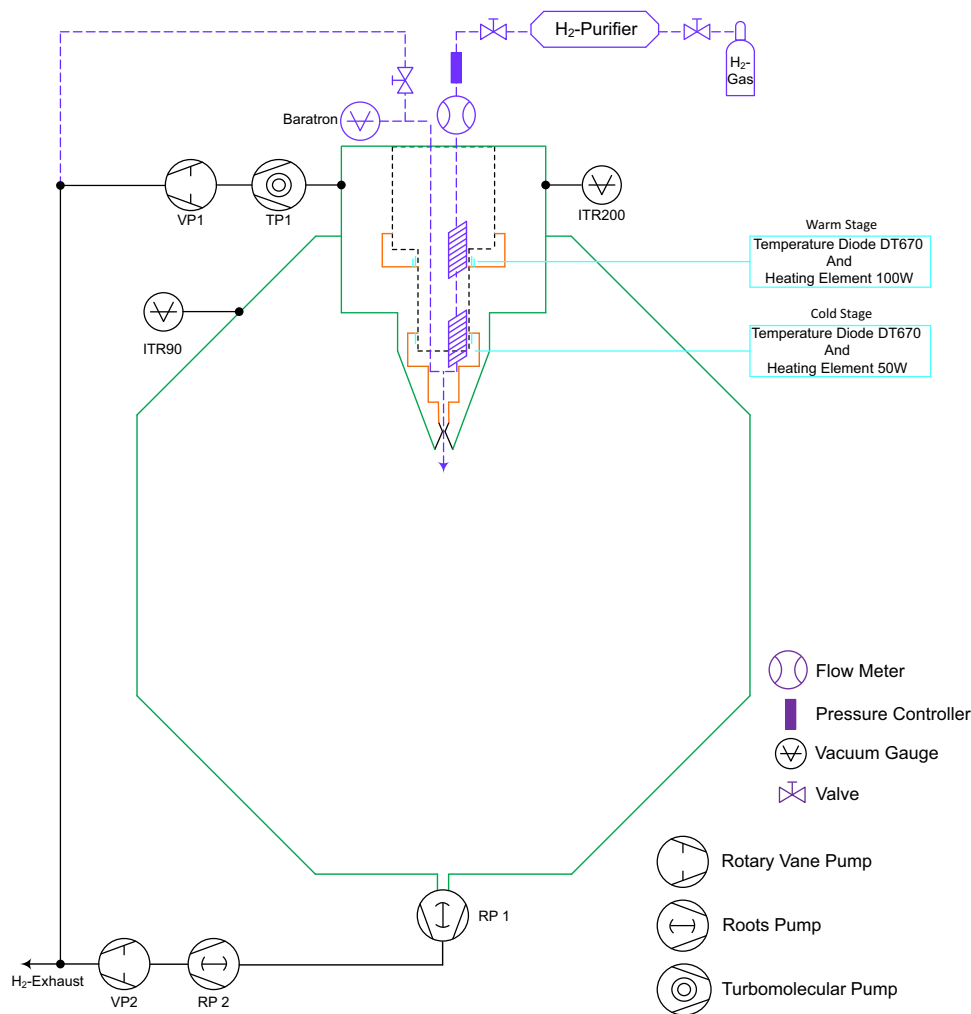


**Figure 3.4** – Schematic view of the MCT-D gas and vacuum system. The cluster source is mounted on the octagonal interaction chamber and the roots pumps are mounted on the opposite side. The gas is lead through the purification cartridge, the pressure controller and the flow meter before entering the isolation vacuum chamber. Therein, the gas is cooled down to operation temperature and exits the cluster source as a cluster jet through the nozzle.

### Slow control software

A slow control software for the target has been written in LabVIEW. Figure 3.6 shows a screenshot of the user interface. The software communicates on a five second basis with the vacuum gauges via a Leybold Centre Three, the flow meter and the pressure

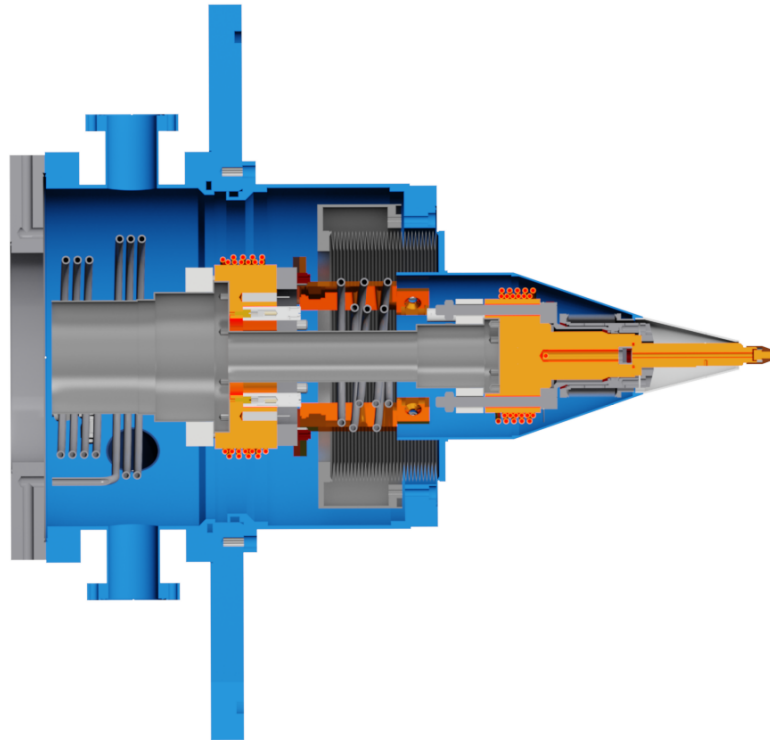


**Figure 3.5** – Cross section of MCT-D. The isolation vacuum chamber is highlighted in blue. While nozzle and cold finger are at the temperature of the cold stage, the tip of the isolation vacuum chamber and the radiation shield is at the temperature of the warm stage and decoupled from the cold stage by a bellow. Furthermore it is decoupled from the rest of the isolation vacuum chamber, which is on room temperature, by another bellow. Picture generated by D. Veith.

**Table 3.2** – Specification of the vacuum gauges and pumps at the isolation chamber (IC) and the interaction chamber (IAC). The pump nomenclature is in agreement with figure 3.4.

component	specification	nominal pumping speed
vacuum gauge IC	Leybold Ionivac ITR200	
turbo pump TP1	Leybold TURBOVAC 90i	324 m <sup>3</sup> /h
fore pump VP1	Leybold TRIVAC D 25 B	25.7 m <sup>3</sup> /h
vacuum gauge IAC	Leybold Ionivac ITR90	
roots pump RP1	Leybold RUVAC WH 7000	7800 m <sup>3</sup> /h
roots pump RP2	Leybold RUVAC WSU 1001	1000 m <sup>3</sup> /h
fore pump VP2	Leybold SOGEVAC SV 300	240 m <sup>3</sup> /h

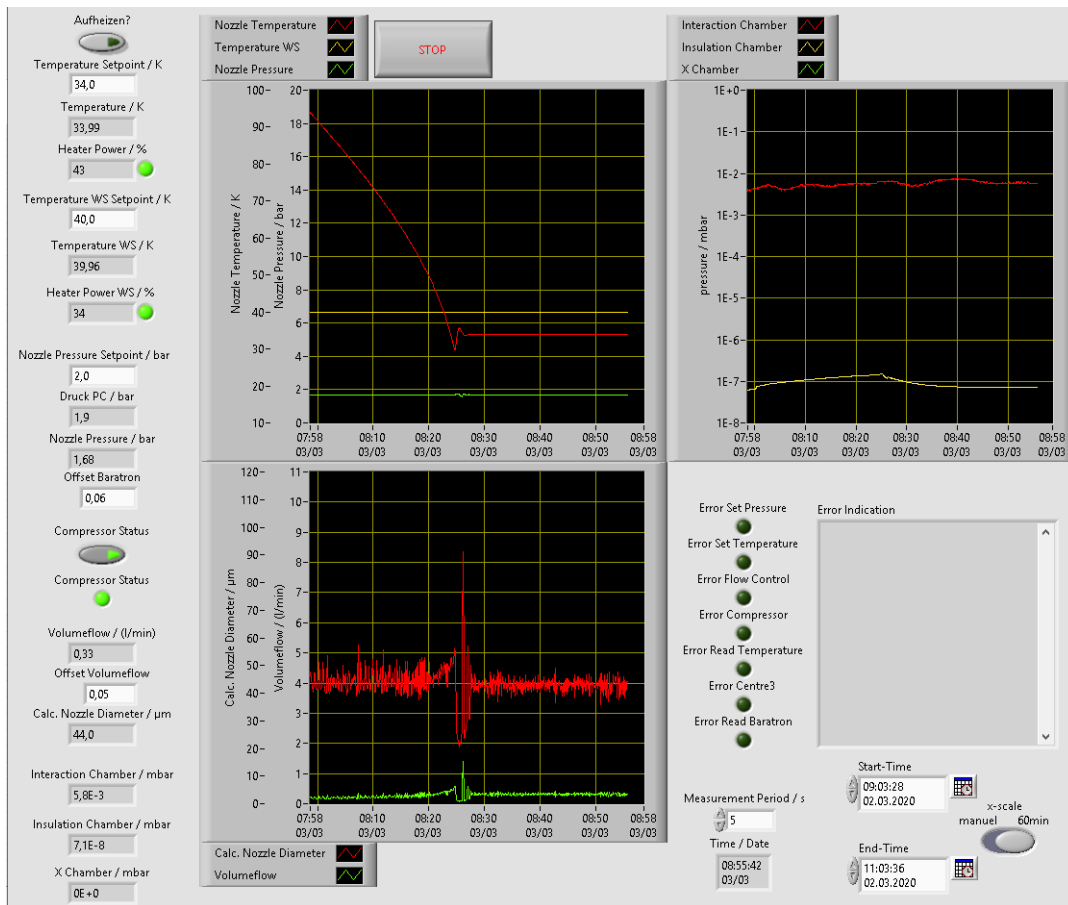


**Figure 3.6** – The user interface of the slow control. All measured values are displayed on the left side directly next to their set-point values. The three live graphs show the trend of the measured values and in the bottom right corner are some lights and a text box indicating errors. Below the text box is the time control for the live graphs with manual start and end times.

controller via the Brooks Model 0254 and with the temperature controller LakeShore Model 336. A direct communication with the mentioned hardware has not been chosen to increase the safety of the system in case of a computer failure. All measured values are displayed in the user interface of the slow control software and for each value a graph of the trend of the last 60 minutes is drawn. This time interval can be adjusted to a user-defined time span. A log file with all measured values is generated for each day using the date as the name of the file. Every cycle of the software writes another line in the same file. The measured temperature  $T$ , volume flow  $q_V$  and pressure  $p$  are used to calculate the narrowest nozzle diameter  $d_N$  by using

$$q_V = \dot{m}^* \frac{R T_N}{M p_N} \quad (3.2.1)$$

and formula 3.1.14 with the narrowest sectional area  $A^* = \pi d_N^2/4$  to attain

$$q_V = p_0 A^* \frac{T_N}{p_N} \sqrt{\frac{\kappa R}{m T_0}} \left( \frac{2}{\kappa + 1} \right)^{\frac{\kappa+1}{2(\kappa-1)}} \quad (3.2.2)$$

$$\Leftrightarrow d_N = 2 \sqrt{\frac{q_V p_N}{\pi p_0 T_N}} \sqrt{\frac{M T_0}{\kappa R}} \left( \frac{2}{\kappa + 1} \right)^{\frac{\kappa-1}{\kappa+1}}. \quad (3.2.3)$$

This value is displayed and logged in exactly the same way as the values measured directly. If an impurity in the gas freezes in the nozzle and starts to clog it up, the volume flow will drop resulting in a lower calculated nozzle diameter. This can be used to detect a clogging of the nozzle independent of pressure and temperature.

The slow control can also be used to send set point values to the PI controllers for temperature and pressure. The compressor for the gas cooling can be switched on and off by the slow control software, too. A light indicates the current state of the compressor. Since the operation with hydrogen is dangerous because of the easily mixed and highly explosive oxyhydrogen, all measured values are supervised by another software written by B. Hetz. Should at least one of the measured values no longer be in an acceptable range, this software sends an e-mail to the person responsible. This may indicate e.g. the blackout of a vacuum pump or other deficiencies needing immediate attention of the experimentalist.

### Performance and stability

The newly built MCT-D was tested concerning its performance, namely the lowest achievable temperature for a given pressure and its stability over a few hours of operation at constant parameters. The minimal viable temperature was found by cooling down the MCT-D at a certain pressure until the temperature reached its lowest value while

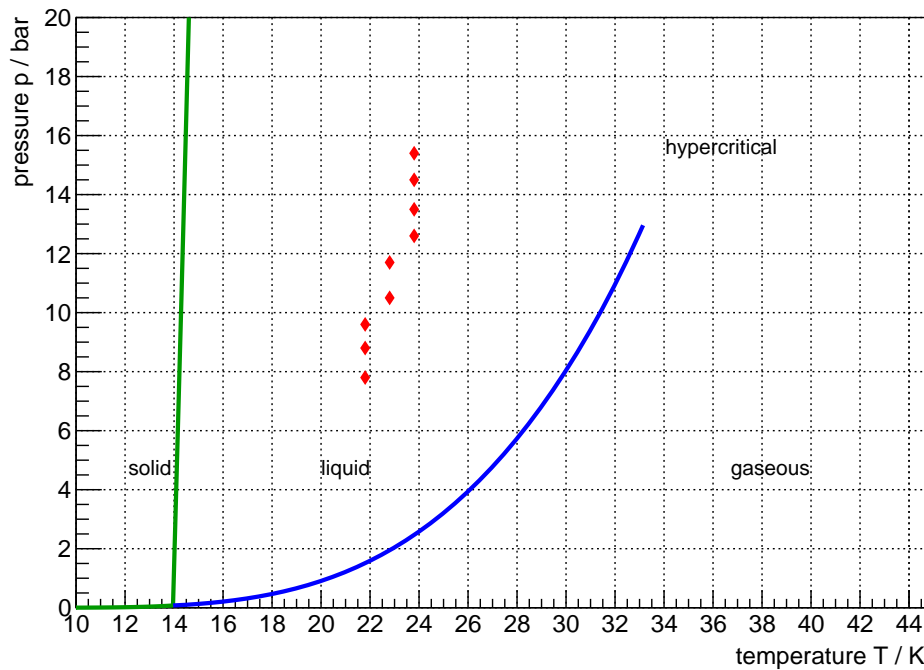


**Figure 3.7** – Phase diagram of hydrogen. The lowest nozzle temperatures achievable for each pressure with stable performance are marked in red.

the heating was switched off. Since the stability is greatly improved by using a small percentage of the heating power available, the temperature set-point was set to a value slightly above the lowest possible temperature. This was monitored for 30 minutes to confirm stable operation. The lowest temperature found can be seen in figure 3.7. This measurement shows that the MCT-D can be operated even at high pressures deep in the liquid phase fulfilling the desired parameters. Compared with the MCT-1S used beforehand an improvement in the minimal stable temperature from 50 K at 16 bar [Gri18] to 22.0(6) K at 16 bar has been achieved.

The stability of MCT-D was investigated by monitoring all measured values at constant operation parameters for four hours, which is a lot longer than the planned measurements. This was investigated for two different sets of pressure and temperature, once in the liquid phase and once with gaseous hydrogen. The three most important parameters are temperature and pressure for the stability of the cluster sizes and the interaction chamber vacuum, since this is very sensitive to fluctuations in the gas flow rate and

thus the density of the cluster jet. Figure 3.8 shows the plotted log files of the stability measurements. The blue data corresponds to gaseous hydrogen and the green data corresponds to liquid hydrogen upstream of the nozzle. The mean values of the shown measured values over the whole stability measurements are listed with the corresponding standard deviations in table 3.3. All measured values stay very constant over the whole measurement. The temperature diodes have a specified reproducibility of  $\pm 10$  mK at 4.2 K [LSC21] while the measured standard deviations are 5 mK at 38 K and 20 mK at 22 K. While the values taken at the lower temperature fit very well for a slightly fluctuating temperature value, the standard deviations of the values taken at the higher temperature is smaller than the specified reproducibility. This may be caused by a reduction of the displayed and saved digits by the slow control software. The baratron has a accuracy of 0.5% but no specified reproducibility [Inc16]. The measured standard deviations of 0.08% at 38 K and 0.8% at 22 K are in the same range as the specified accuracy and low enough to guarantee a very stable operation. The flow meter has a specified repeatability of 0.2% [Ins13] which is slightly below the measured standard deviations of 1.2% at 38 K and 0.5% at 22 K, which again fits very well for a slightly fluctuating gas flow. The vacuum gauge used has as specified repeatability of 5% [Ley16], while the measured standard deviations are 0.4% at 38 K and 0.2% at 22 K. This may again be caused by a reduction of the displayed and saved digits by the slow control software. Altogether, the stability of the MCT-D is more than sufficient in both hydrogen states.

**Table 3.3** – Mean values and standard deviations of the measured values of the two stability measurements shown in figure 3.8.

	12 bar / 38 K	16 bar / 22 K
temperature CS / K	37.996(5)	22.000(20)
gas pressure / bar	11.58(1)	15.48(13)
gas flow / (l/min)	1.62(2)	10.47(5)
interaction chamber vacuum / mbar	0.01709(6)	0.1000(2)

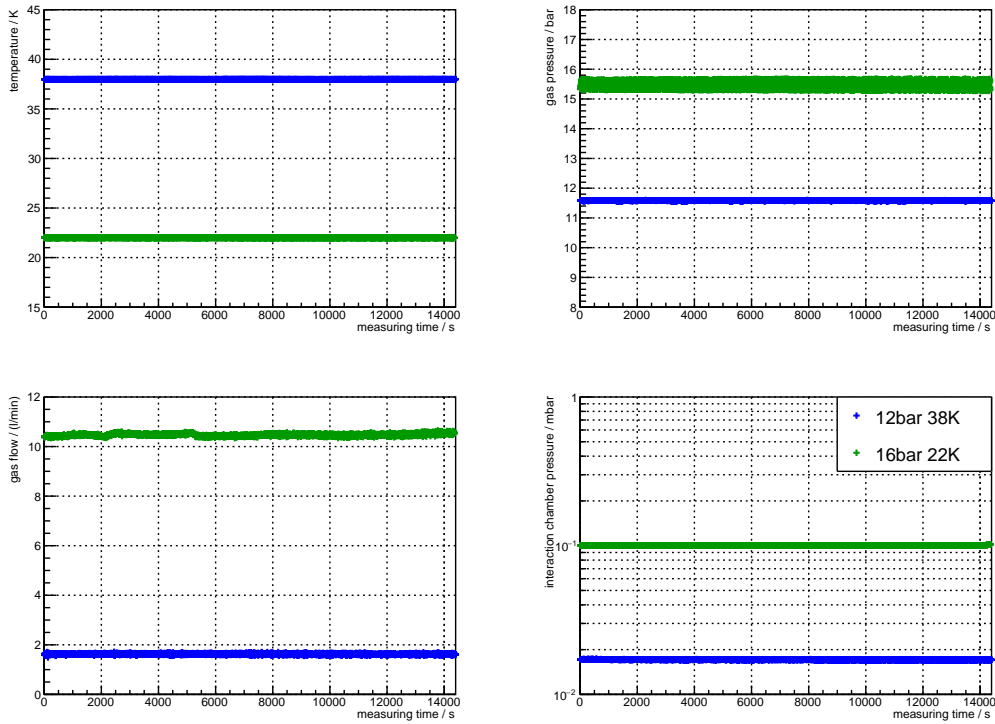


**Figure 3.8** – Measured values of two stability measurements, each over four hours long. The green data corresponds to a measurement in the liquid regime at 16 bar and 22 K and the blue data corresponds to a measurement in the gaseous regime at 12 bar and 38 K. Shown are the temperatures of the cold stage (top left), the gas pressure upstream of the nozzle (top right), the gas flow through the nozzle (bottom left) and the pressure in the interaction chamber (bottom right).

### 3.3 Cluster jet density estimation

The density of the cluster jet provided by the MCT-D can be estimated with an interferometric measurement performed with a Michelson interferometer. Therein, a collimated laser beam of wavelength  $\lambda = 532 \text{ nm}$  is enlarged in diameter and split into two beams of equal intensity by a beam splitter. Both beams are reflected by mirrors back to the beam splitter, from where they are guided to a CCD camera taking an image of the interference pattern. One of the beams penetrates the cluster jet on its way to and back from the mirror. Figure 3.9 shows a schematic sketch of the setup. The cluster jet has a density dependent refraction index

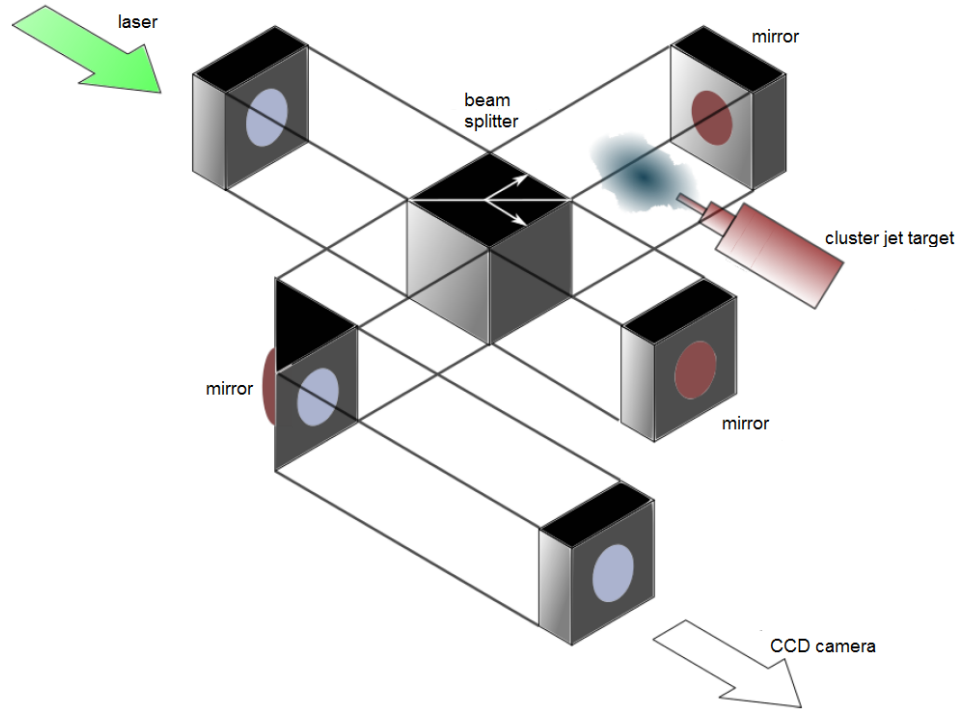


**Figure 3.9** – Schematic sketch of the Michelson interferometer setup. The incoming green laser beam is split into two beams of equal intensity, which interfere after one of them passed the cluster jet. A CCD camera was used to take pictures of the interference pattern [Sch20], edited.

$$\frac{\Delta n}{\rho} = \frac{n - 1}{\rho} = k_{\text{GD}} = \text{const.} \quad (3.3.1)$$

with the Gladstone-Dale constant  $k_{\text{GD}}(\text{H}_2) = 1.55 \frac{\text{cm}^3}{\text{g}}$  [Mer12] causing an optical path length difference between the two laser beams of

$$\Delta L = 2 \int \Delta n(z) dz . \quad (3.3.2)$$

The electric field strength of the incoming laser beam  $E(\vec{r}) = |E| e^{i(\vec{k} \cdot \vec{r} - \omega t + \Phi)}$  can be used to calculate the interference intensity



$$E_1(z, t) + E_2(z, t) = (|E_1| e^{i\Phi_1} + |E_2| e^{i\Phi_2}) e^{i(k_z z - \omega t)} \quad (3.3.3)$$

$$= |E_{\text{total}}| e^{i(k_z z - \omega t)} \quad (3.3.4)$$

$$I \propto |E_{\text{total}}|^2 = |E_1|^2 + |E_2|^2 + 2 |E_1| |E_2| \cos \Delta\Phi \quad (3.3.5)$$

with the phase difference  $\Delta\Phi$  between the two interfering laser beams [Sch13]. This phase difference can be seen in the images taken with the CCD camera as small shifts of the interference fringes and it is related to the optical path difference and the cluster jet density as

$$\Delta\Phi = \frac{2\pi}{\lambda} \Delta L = 2 \frac{2\pi}{\lambda} \int \Delta n \, dz \quad (3.3.6)$$

$$= \frac{4\pi k_{\text{GD}}}{\lambda} \int \rho \, dz . \quad (3.3.7)$$

The areal density of the cluster jet can be determined by the phase shift in the interference fringes as

$$\rho_{\text{A}} = \int \rho \, dz = \frac{\Delta\Phi \lambda}{4\pi k_{\text{GD}}} . \quad (3.3.8)$$

Figure 3.10 shows an interference pattern taken at stagnation conditions of 16 bar and 24 K and at a gas flow of 10  $\ell/\text{min}$ , which corresponds to the maximum possible cluster jet density. Although huge fringe sizes were chosen to maximise the sensitivity, no shifts in the fringes were observed. A shift of around 40 pixel should be clearly visible as the distance between the two fringes is around 800 pixel. This would correspond to a phase shift of  $\pi/20$ , which would be caused by an areal density of  $\rho_{\text{A,max}} = 2.5 \times 10^{17} \text{ cm}^{-2}$ . This can be converted into a peak density of  $\rho_{\text{max}} = 1.7 \times 10^{18} \text{ cm}^{-3}$  as an upper limit of the reachable target density by assuming a Gaussian shaped density profile. The prediction for the same stagnation conditions according to formula 3.1.17 is  $\rho_{\text{theo}} = 8.5 \times 10^{17} \text{ cm}^{-3}$

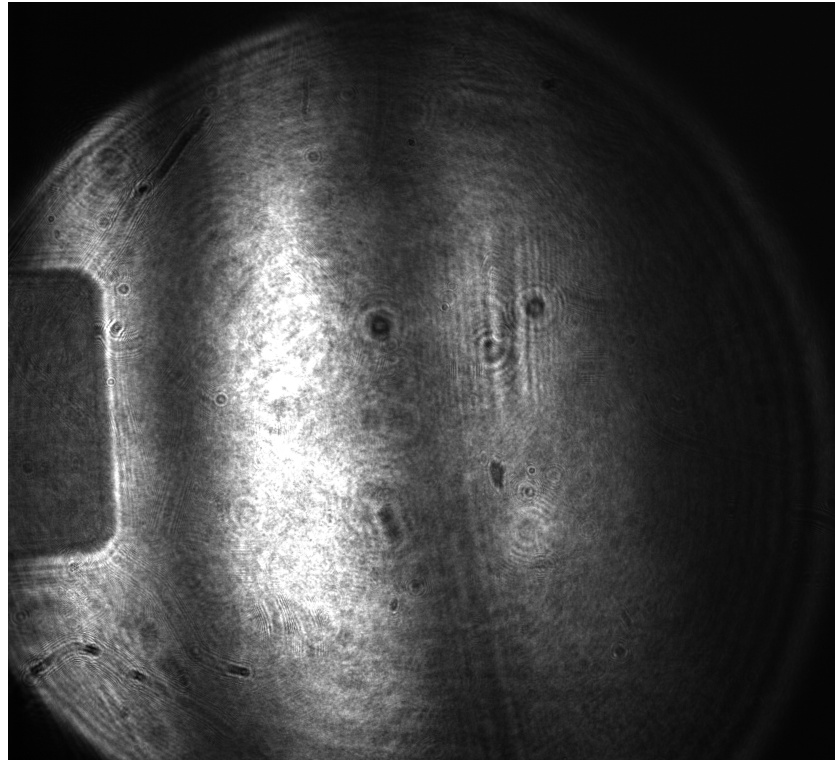


**Figure 3.10** – Interference pattern taken at stagnation conditions of 16 bar and 24 K and at a gas flow of 10  $\ell$ /min. Although the fringe sizes chosen were very large, no shift in the fringes can be observed.

and thus well below this limit.

### 3.4 Cluster size determination using Mie-Scattering

Since the cluster size is very important for the Coulomb explosion (e.g. formula 2.3.6), two different types of measurements were done to determine the cluster size distribution of the cluster jet used. The first type is a scattering experiment based on Mie-scattering. This uses the asymmetric scattering pattern, created by a laser scattering at objects of comparable size to the laser wavelength, to determine the cluster sizes and is presented in this section. The second measurement uses ultra-short laser pulses to take photos of the cluster jet, where the larger clusters can be seen as shadows on the pictures. These

measurements are presented in the next section.

The elastic scattering of a plane wave at a spherical inhomogeneity can be described by Mie theory [Hah09]. This results in a scattering pattern dependent on the polarisation of the incident light and on the diameter of the scattering body. The scattering intensity observed at a distance  $r$  from the interaction point is

$$I_{\text{scat}} = \frac{I_0}{r^2} \sigma_{\text{scat}} \quad (3.4.1)$$

with the incident intensity  $I_0$  and the polarisation dependent scattering cross-section [BH08, Hah09]

$$\sigma_{\text{scat S1,S2}} = \frac{\lambda^2}{4\pi^2} i_{\text{S1,S2}}. \quad (3.4.2)$$

Therein S1 and S2 are the two linear polarisations of the incident light. S1 represents an oscillation of the electric field orthogonally to the plane of incidence and S2 represents an oscillation of the electric field parallel to the plane of incidence. The angular dependency of Mie scattering is hidden in the intensity functions  $i_{\text{S1,S2}}$ . These can be written as

$$i_{\text{S1}}(\alpha, \theta) = \left| \sum_{n=1}^{\infty} \frac{2n+1}{n(n+1)} [a_n(\alpha)\pi_n(\cos\theta) + b_n(\alpha)\tau_n(\cos\theta)] \right|^2 \quad (3.4.3)$$

$$i_{\text{S2}}(\alpha, \theta) = \left| \sum_{n=1}^{\infty} \frac{2n+1}{n(n+1)} [b_n(\alpha)\pi_n(\cos\theta) + a_n(\alpha)\tau_n(\cos\theta)] \right|^2 \quad (3.4.4)$$

with the scattering angle  $\theta$  relative to the incoming laser direction and the angular functions

$$\pi_n(\cos \theta) = \frac{P_n(\cos \theta)}{\sin \theta} \quad (3.4.5)$$

$$\tau_n(\cos \theta) = \frac{d}{d\theta} P_n(\cos \theta) \quad (3.4.6)$$

which can be built from Legendre polynomials  $P_n(\cos \theta)$  and with [Hah09]

$$a_n = \frac{S_n(\alpha)S'_n(\alpha) - mS'_n(\alpha)S_n(m\alpha)}{\phi_n(\alpha)S'_n(m\alpha) - m\phi'_n(\alpha)S_n(m\alpha)} \quad (3.4.7)$$

$$b_n = \frac{mS'_n(\alpha)S_n(\alpha) - S_n(m\alpha)S'_n(\alpha)}{m\phi_n(\alpha)S'_n(m\alpha) - \phi'_n(\alpha)S_n(m\alpha)}. \quad (3.4.8)$$

Therein primed values are derivatives and the dependency on the size of the scattering body is in the size parameter  $\alpha = 2\pi d_{\text{obj}} n_0 / \lambda$  with the scattering object diameter  $d_{\text{obj}}$ , its index of refraction  $n_0$  and the wavelength of the incident light  $\lambda$ .  $\phi_n$  and  $S_n$  are Ricatti-Bessel functions expressed by Bessel functions of the first kind  $J_n$  or Hankel functions of the second kind  $H_n$ , respectively:

$$\phi_n(x) = \left(\frac{\pi x}{2}\right)^{1/2} H_{n+1/2}(x) \quad (3.4.9)$$

$$S_n(x) = \left(\frac{\pi x}{2}\right)^{1/2} J_{n+1/2}(x) \quad (3.4.10)$$

Figure 3.11 shows the scattering patterns for three objects of different size. A strong dependency on the scattering object's size can be seen in the total scattering amplitude and in the asymmetry of the scattering patterns.

The clusters in a cluster jet as the one generated by the MCT-D (cf. section 3.2) are not of a uniform size, but follow a distribution function. The particle size distribution is well described by a Nukiyama-Tanasawa function for clustering gases and by a logarithmic normal distribution for clustering liquids [ME51]. The logarithmic normal function is defined as

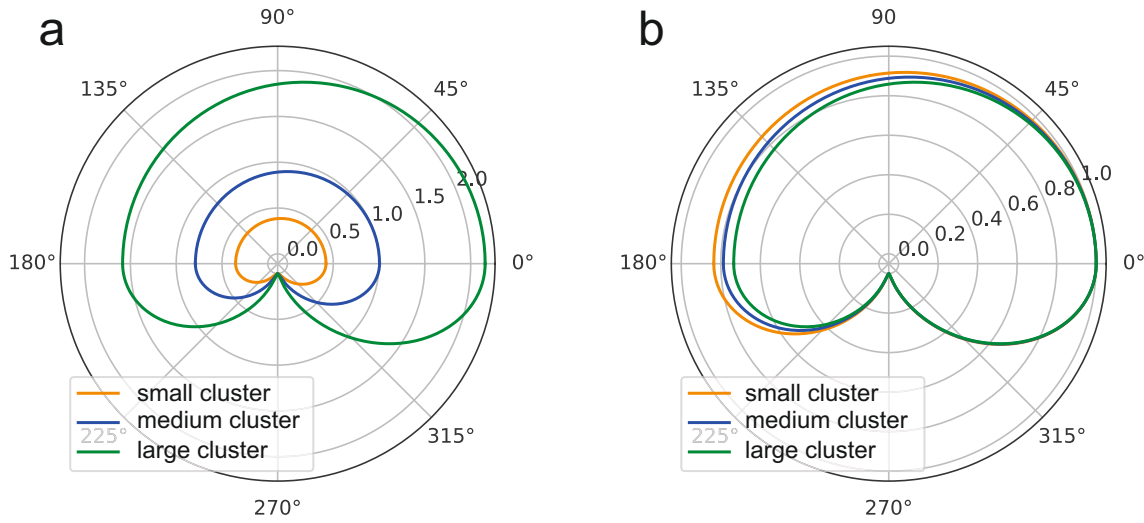


**Figure 3.11** – Calculated scattering patterns for three different scattering object (or cluster) sizes. The top side of the polar plots ( $0^\circ$  to  $180^\circ$ ) shows the scattering pattern for S1 polarised laser light and the bottom side of the polar plots ( $180^\circ$  to  $360^\circ$ ) shows the scattering pattern for S2 polarised laser light. The left side shows the three patterns with the same axis and visualises the increase of the absolute scattering intensity with the size of the scattering object and the right side shows the three scattering patterns normalised individually. This shows the increase of the asymmetry with increasing scattering object diameter [Man19].

$$f(x, \mu, \sigma) = \frac{1}{x\sigma\sqrt{2\pi}} \exp\left\{-\frac{(\ln(x) - \mu)^2}{2\sigma^2}\right\} \quad (3.4.11)$$

with the parameters  $\mu$  and  $\sigma$  and the Nukiyama-Tanasawa function is given as

$$f(x, S) = \frac{3x^2}{\Gamma\left(\frac{5}{3}\right)^3 S^3} \exp\left(-\frac{x^3}{\Gamma\left(\frac{5}{3}\right)^3 S^3}\right) \quad (3.4.12)$$

with the gamma function  $\Gamma\left(\frac{5}{3}\right)$  and the Sauter mean diameter  $S$ . The mean of the a particle distribution  $f_{PD}$  can be calculated to

$$\bar{N} = \langle x \rangle = \frac{\int_{-\infty}^{\infty} x f_{\text{PD}}(x) dx}{\int_{-\infty}^{\infty} f_{\text{PD}}(x) dx} \quad (3.4.13)$$

and the standard deviation is calculated to

$$\tilde{\sigma} = \sqrt{\frac{\int_{-\infty}^{\infty} x^2 f_{\text{PD}}(x) dx}{\int_{-\infty}^{\infty} f_{\text{PD}}(x) dx} - \langle x \rangle^2}. \quad (3.4.14)$$

The Mie-scattering pattern of particles of a certain size distribution  $f_{\text{PD}}$  is calculated by integrating the product of the Mie scattering intensity (c.f. equation 3.4.1) and the size distribution over the particle sizes

$$I_{\text{scat, PD}} = V_0 \int_0^{\infty} I_{\text{scat}}(\theta, \alpha(N)) f_{\text{PD}}(N, \bar{N}, \tilde{\sigma}) dN. \quad (3.4.15)$$

Measurements of Mie-scattering patterns have been taken under various stagnation conditions of the cluster source. Figure 3.12 shows a sketch of the experimental setup. An S1 polarised laser illuminates the cluster jet and is dumped behind it. A detector, rotatable around the interaction point, consisting of a converging lens coupled via glass fibre to a photo multiplier is used to record the scattering pattern between  $9^\circ$  and  $165^\circ$ . A  $\lambda/2$  wave plate can be inserted in the optical path of the laser to change the polarisation from S1 to S2.

In the scope of a Master thesis a fitting program for formula 3.4.15 was developed by Christian Mannweiler [Man19]. The results of the best fits found by Christian Mannweiler are summarised at the end of this section in table 3.4 for stagnation conditions in the gaseous regime and in table 3.5 for stagnation conditions in the liquid regime. Figure 3.13 shows two example measurements, one for each regime. The evaluated cluster size distributions are shown in the same figure at the right side. The measurements in the gaseous regime show an only slightly asymmetric diffraction pattern resulting in a

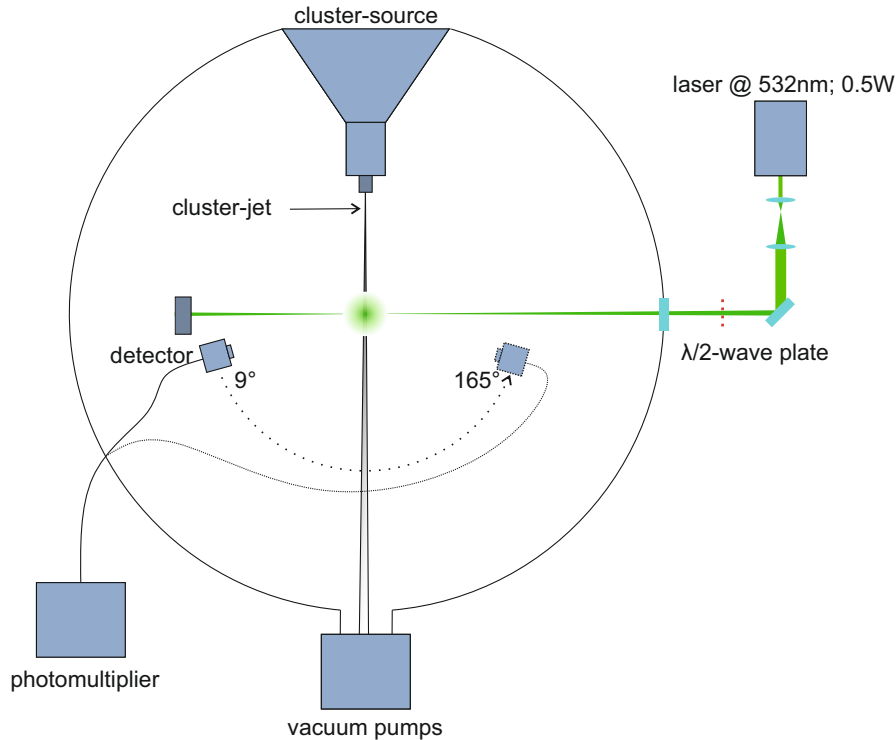


**Figure 3.12** – Sketch of the experimental setup used for Mie-scattering. A laser illuminates the cluster jet and is dumped behind the jet. A  $\lambda/2$  wave plate may be inserted in the optical path to change the laser polarisation. The detector is a collecting lens connected to a glass fibre leading out of the vacuum chamber to a photo multiplier. The detector can be rotated around the illuminated spot to collect a scattering pattern [Man19].

clear cluster size distribution. But the measurements in the liquid regime show very dominant forward scattering. This originates from a few very large clusters generated by the atomisation process (cf. section 3.1) and increases the difficulty to evaluate the cluster size distribution of the smaller clusters. Therefore only the measurements at stagnation conditions in the gaseous regime are treated further.

The Hagen scaling law (cf. formula 3.1.20) predicts the mean cluster size of a cluster jet. However, the Hagen scaling law has been found using noble gas cluster jets and the MCT-D uses hydrogen instead. Figure 3.14 shows the mean cluster sizes found in the Mie measurements in the gaseous regime plotted against their calculated Hagen parameter  $\Gamma^*$ . The mean cluster size prediction by formula 3.1.20 is plotted in red, while a correction of the parameter  $A_N = 33 \rightarrow 25(5)$  found by a best fit to the data

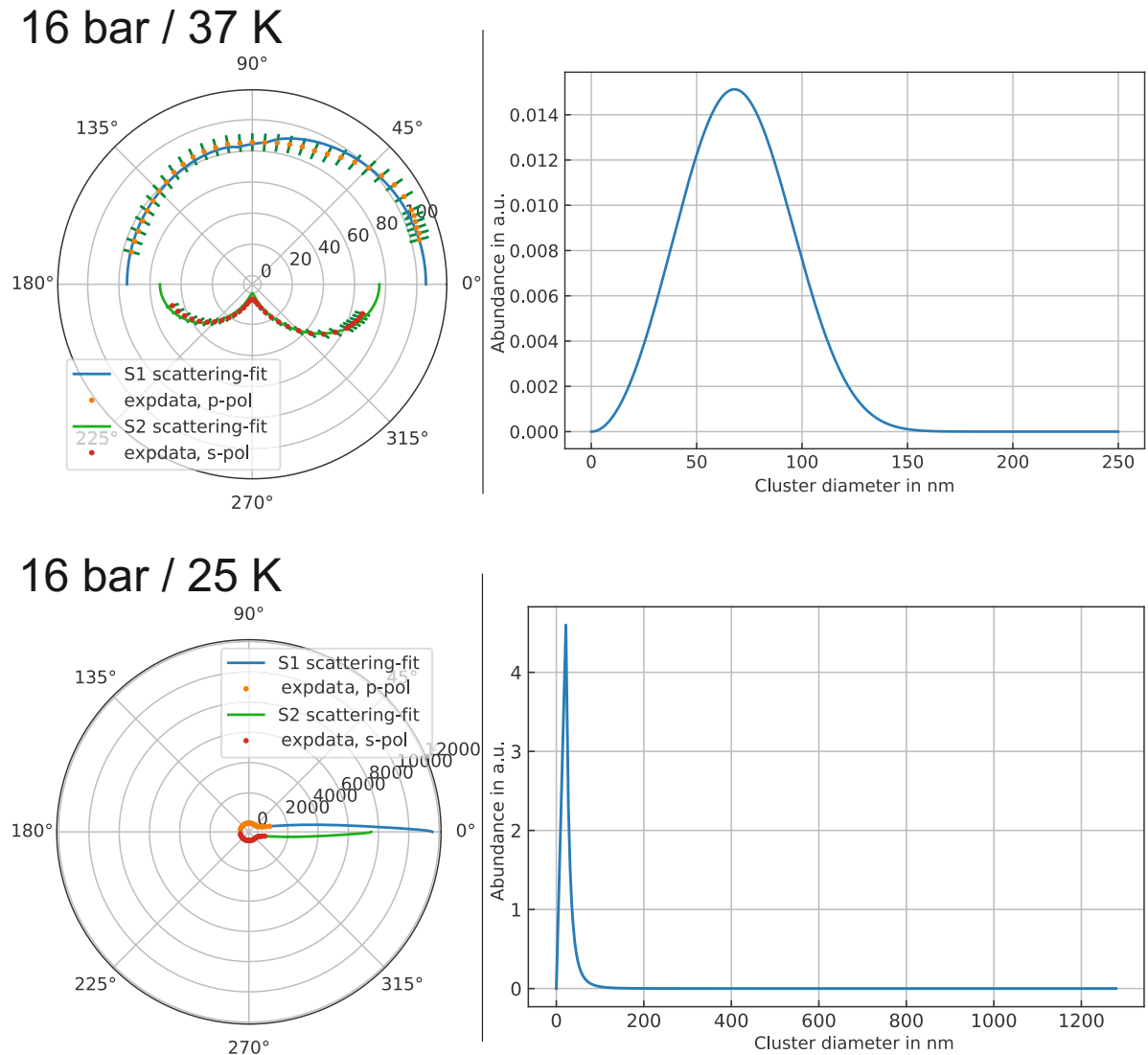


**Figure 3.13** – Examples for Mie measurements of the cluster jet generated by the MCT-D. The left side shows the taken data and the fitted function and the right side shows the evaluated cluster size distribution. The measurement shown in the top was taken with stagnation conditions in the gaseous regime and the measurement in the bottom was taken with stagnation conditions in the liquid regime [Man19].

is plotted in blue. The two high points above 100 nm cluster diameter are not part of the fit, since they belong to stagnation conditions in the hypercritical regime. Another hydrogen correction for the Hagen scaling law found by E. Köhler [Köh15] in another parameter regime is shown in green. She used an electron gun to charge single clusters



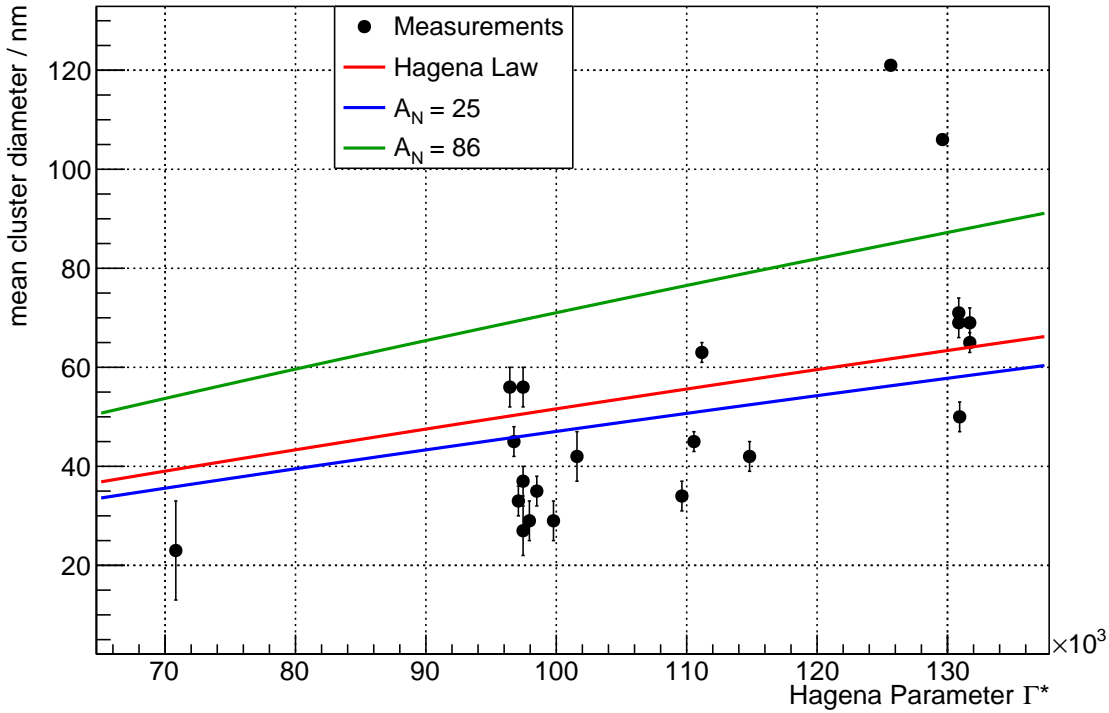


**Figure 3.14** – Results of the Mie measurements with stagnation conditions in the gaseous regime plotted against their calculated Hagena parameter. The Hagena scaling law is shown in red and the two corrected versions are shown in blue (this work) and green (E. Köhler [Köh15]).

in the jet and selected them with an electric field by specific charge. The evaluated mean cluster diameters fluctuate stronger around the best fit than indicated by their estimated uncertainties. However, the evaluated uncertainties include only the performed fit uncertainty and leave other additional uncertainties unattended. E.g. the different standard deviations of the found cluster size distributions are completely ignored for this evaluation. With the correction of the Hagena scaling law to the cluster jet target in use, a prediction of the mean cluster sizes at different stagnation conditions in the gaseous regime is possible without direct measurements.

**Table 3.4** – Mean diameter and standard deviation of cluster size distributions calculated from the parameters of a fit of a Nukiyama-Tanasawa function at the measured Mie-scattering patterns for various stagnation conditions in the gaseous regime [Man19].

temperature / K	pressure / bar	mean diameter / nm	st. dev. / nm
31	8	45(3)	17(1)
32	10	63(2)	23(1)
33	12	121(1)	44(1)
34	10	56(4)	20(2)
34	10	56(4)	20(2)
34	10	27(5)	10(2)
34	10	37(3)	14(1)
35	12	45(2)	16(1)
35	14	106(1)	38(1)
37	12	29(4)	10(1)
37	12	33(3)	12(2)
37	14	42(3)	15(1)
37	16	71(3)	26(1)
37	16	65(2)	24(1)
37	16	69(3)	25(1)
37	16	69(3)	25(1)
39	15	43(5)	16(2)
39	18	50(3)	18(1)
40	16	34(3)	12(1)
42	16	35(3)	13(2)
42	16	29(4)	10(2)
43	12	23(10)	8(4)

**Table 3.5** – Mean diameter and standard deviation of cluster size distributions calculated from the parameters of a fit of a logarithmic normal distribution at the measured Mie-scattering patterns for various stagnation conditions in the liquid regime [Man19].

temperature / K	pressure / bar	mean diameter / nm	st. dev. / nm
22	4	38(10)	40(10)
22	7	39(14)	40(14)
22	10	114(42)	93(24)
22	13	16(5)	14(7)
22	16	22(3)	21(4)
25	7	34(7)	37(8)
25	10	14(4)	10(6)
25	13	16(5)	13(7)
25	16	15(5)	12(7)
25	18	14(2)	6(3)
28	10	41(11)	43(10)
28	13	23(6)	24(7)
28	16	20(5)	19(7)
28	18	18(6)	17(8)
31	13	125(24)	102(13)
31	16	48(12)	50(11)
34	16	184(10)	105(4)

### 3.5 Cluster size determination using shadowgraphy

Under stagnation conditions in the liquid regime larger clusters with a diameter of several micrometers form in the atomisation process (c.f. formula 3.1.24). These clusters dominate in the Mie-scattering patterns due to their bigger size making the reconstruction of the cluster size distribution with the setup used impossible. A further characterisation of the cluster jet is done with a shadowgraphy measurement. For this, the main ARCTURUS laser pulse is used without any amplification and the focus of the laser is shifted to a point in front of the cluster jet. The focus diagnostics consisting of an objective and a camera are used to take backlighted photos of the cluster jet. A sketch of the experimental setup can be seen in figure 3.15. The short pulse durations are important since the clusters are moving with 200 – 400 m/s [Täs12] and a blurring of the objects due to their movement while the illumination has to be prevented. Four settings with different stagnation temperatures (25 K, 27 K, 29 K, 31 K) and constant pressure (16 bar) were used and 40 photos were taken for each setting. Another 40 photos were taken for comparison at a setting at stagnation conditions in the gaseous regime (16 bar, 40 K) where no micrometer sized clusters were expected nor measured.

Figure 3.16 shows an example photo with micrometer sized clusters and another photo at stagnation conditions in the gaseous regime without any of these large clusters for comparison. The large dimensions of the cluster jet ( $\sim 1$  cm) compared with the depth of focus of the used objective ( $Z = 14 \mu\text{m}$ ) results in a strong background on the photos generated by scattering of the incoming laser at clusters outside of the depth of focus. The images show a distribution of sharply visible cluster shadows, blurred cluster shadows and cluster shadows with interference fringes around them. The sharply visible clusters shadows correspond to clusters inside of the depicted focus volume. Clusters outside of the focus volume are shown as blurred clusters if they are close to the focus volume. At larger distances they show interference fringes around them. Cluster shadows of clusters outside of the focus volume are shown enlarged due to the divergent illuminating laser beam. A calibration of the images for the determination of the cluster sizes were done by B. Aurand by taking images of the focus spot of the main ARCTURUS laser pulse. Ten focus spot images were taken at the starting position and an additional ten images were taken after shifting the objective by 50/100/150  $\mu\text{m}$  with a step motor. The position

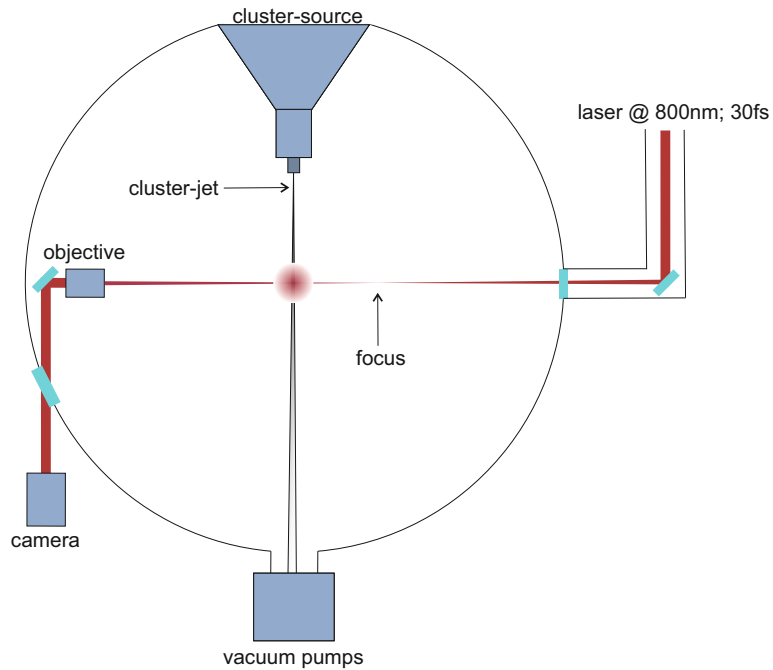


**Figure 3.15** – Sketch of the experimental setup used for the shadowgraphy of the cluster jet. A short laser pulse (30 fs) illuminates the cluster jet while the focus diagnostics consisting of an objective and a camera takes backlit photos of the cluster jet. Based on an image generated by C. Mannweiler.

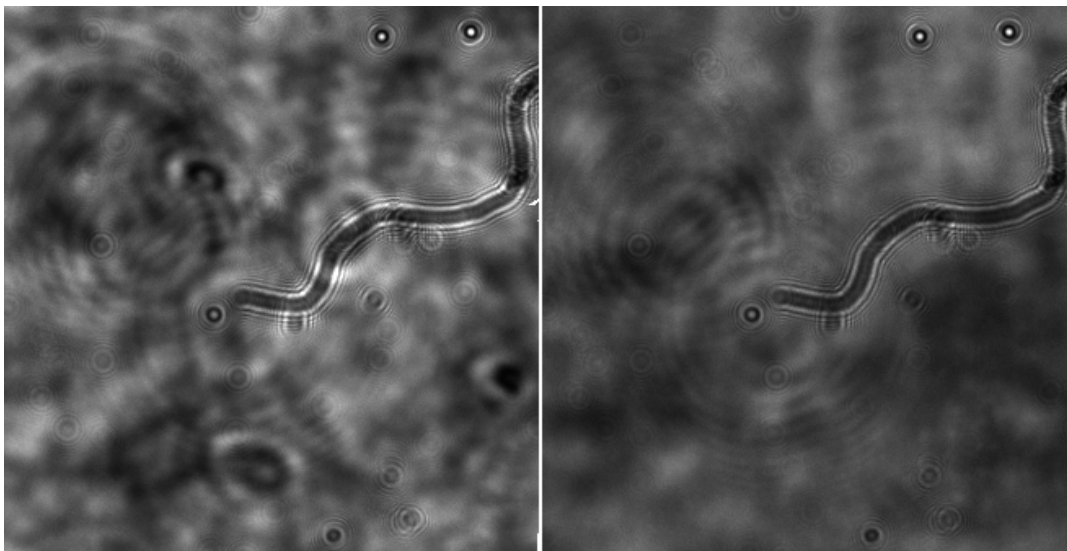


**Figure 3.16** – The left side shows an example shadowgraphy photo with several micrometer sized cluster visible as dark spots or shadows while the right side shows a reference photo taken at stagnation conditions in the gaseous regime without any large clusters visible.

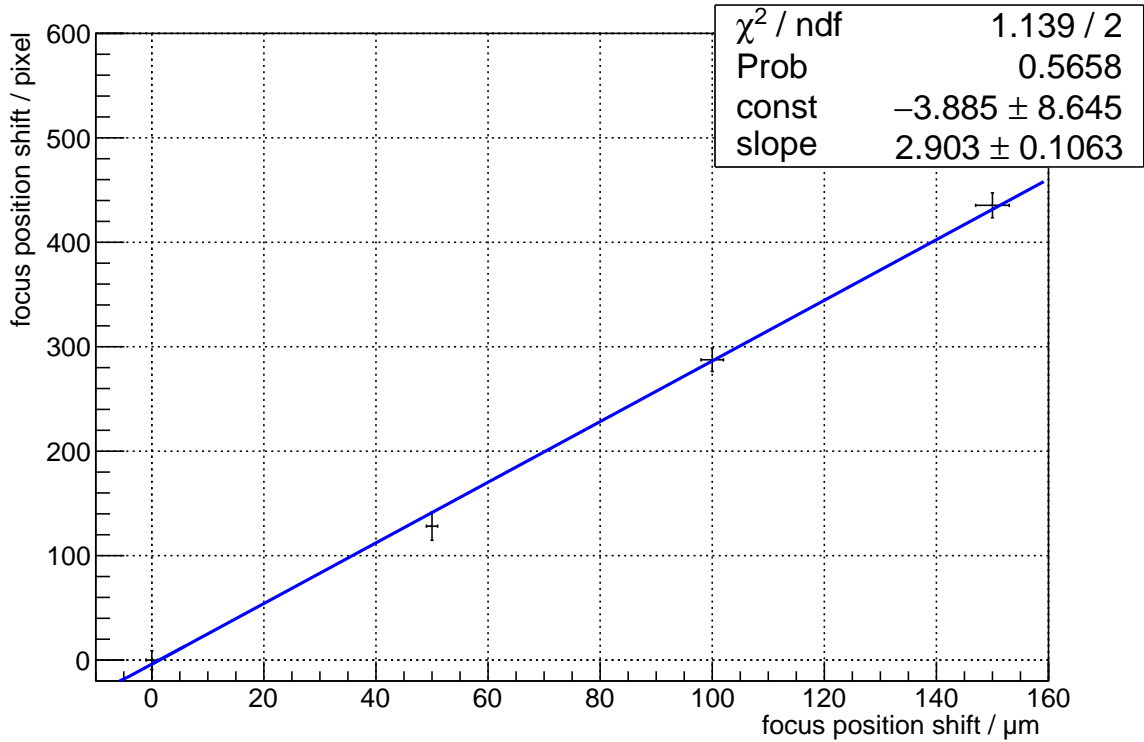


**Figure 3.17** – Calibration of the photos taken with the focus diagnostics. The inverse of the slope of the best fit is the calibration factor  $0.344(13) \mu\text{m}/\text{pixel}$ . Data taken by B. Aurand.

shift of the focus spot has been determined from each image. This is depicted in figure 3.17. The inverse of the slope of the best fit is the calibration factor  $0.344(13) \mu\text{m}/\text{pixel}$ .

For this and all following best fits a  $\chi^2$  minimisation method is used. Thereby, the square sum of the distances of the single data points to the fit function weighted by the squared inverse of the corresponding uncertainty is minimised. As a measure for the goodness of the fit,  $\chi^2/\text{ndf}$  with the number of degrees of freedom (ndf) of the fit is shown together with the fit parameters and should be close to 1. In addition the probability that the data measured could be generated by the best fit found is specified as "Prop".

The sharply visible shadows of clusters were counted and their sizes were measured using the presented calibration for the four different stagnation temperature settings and all 40 photos per setting. Since these clusters were seen sharply they were located

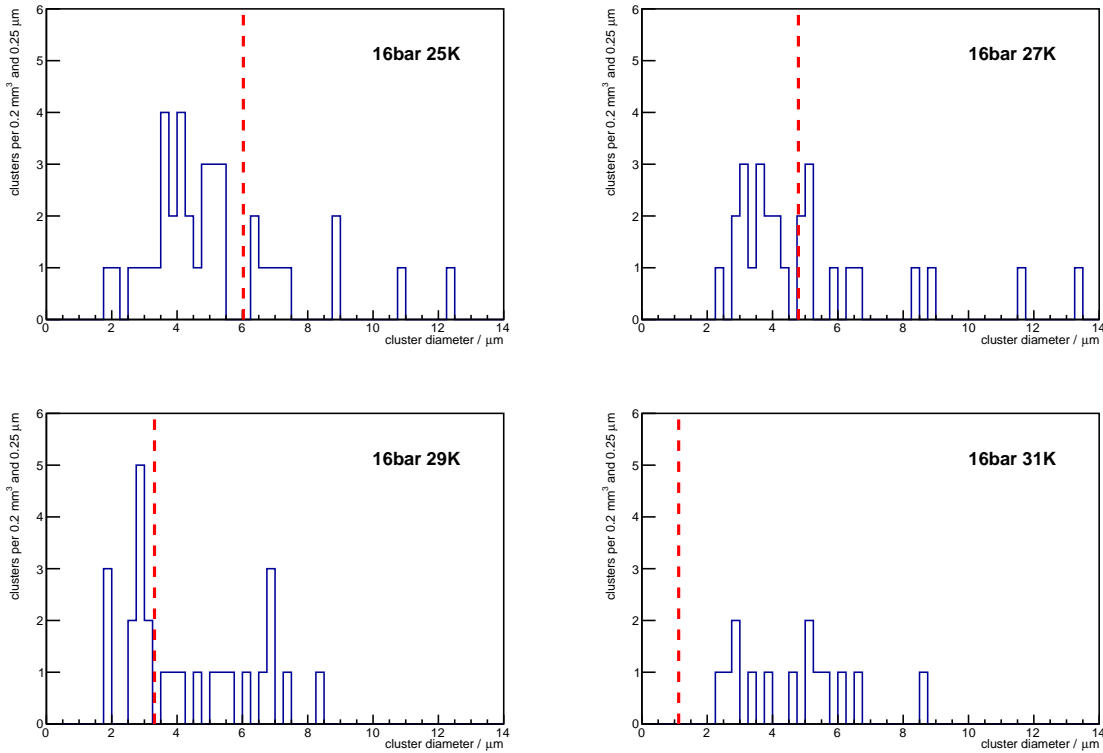


**Figure 3.18** – Found cluster size distributions for the four different stagnation temperatures. All sharp clusters in 40 photos per temperature were measured and counted, this corresponds to an evaluated volume of  $0.2 \text{ mm}^3$ . The dashed red lines mark the respective maximum cluster size of the atomisation process.

in the focus volume of the used objective. The evaluated volume per temperature is calculated by the size of the single photos multiplied with the depth of focus of the used objective and the number of photos taken  $V = A \cdot Z \cdot 40 = 0.2 \text{ mm}^3$ . Figure 3.18 shows the found cluster size distributions for all four measured settings. No large clusters were seen in the photos taken at stagnation conditions in the gaseous regime. Clusters below  $1.75 \mu\text{m} \approx 6 \text{ px}$  are too small to be detected due to the strong background on the photos. The dashed red lines show the maximum cluster size of the atomisation process calculated by formula 3.1.24. There are a non significant number of clusters beyond the respective limit. These may be a tail of a wide cluster size distribution centred around a value below the calculated limit, but this can not be proved with the given statistics. There may be an error in the evaluation of the photos since all clusters outside of the focus volume are depicted larger than they are and it is difficult to judge

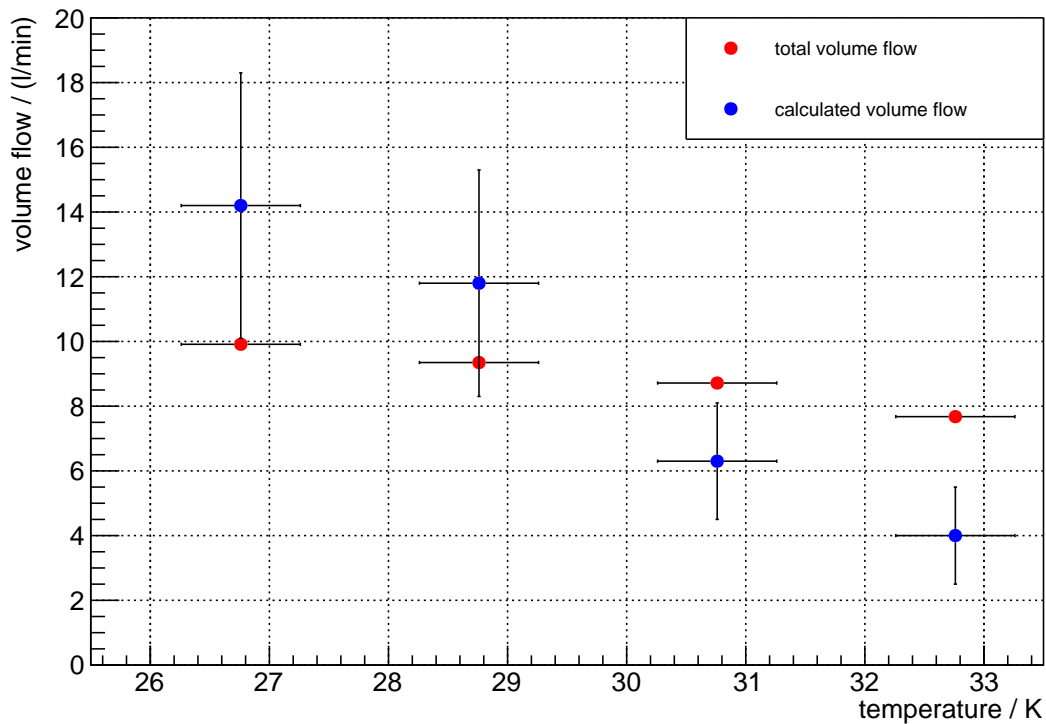


**Figure 3.19** – Calculated volume flow of the observed micrometer sized clusters in comparison with the measured total volume flow. The fraction of the larger clusters of the total volume flow increases with lower temperatures.

whether a cluster shadow is sharp or not. Or this may be a result of the geometric shape of the clusters, which is not always axially symmetric as assumed in theory and evaluation.

The fraction of the gas flow contained in micrometer sized clusters to the measured total gas flow can be calculated using the evaluated density of the micrometer sized clusters. Figure 3.19 shows the calculated gas flow contained in the larger clusters in comparison with the measured total gas flow. The fraction of the larger clusters increases with lower temperatures.

Since the large clusters are very rare in the cluster jet, the interaction probability of the focused ARCTURUS laser pulse with one of the larger clusters is calculated. A listing of the number of found large clusters and the number of shots necessary for a probability of



95% for at least one interaction is shown in table 3.6. Even in the best case at the lowest possible temperature 25000(8000) shots are necessary to ensure a single interaction. This number is roughly two orders of magnitude higher than the planned number of shots in the later main experiment (c.f. chapter 5) and thus no interaction of the focused laser pulse with a micrometer sized cluster can be expected.

**Table 3.6** – Total number of counted and measured micrometer sized clusters per temperature and the number of shots necessary for at least one interaction of the ARCTURUS laser with one of these clusters. The number of shots necessary for an interaction is approximately two orders of magnitude bigger than the number of shots recorded (c.f. chapter 5).

temperature / K	clusters per 0.2 mm <sup>3</sup>	shots for interaction (95%)
25	37	25000(8000)
27	26	37000(12000)
29	25	38000(12000)
31	13	74000(29000)

## Summary

This chapter presented the newly build cluster source MCT-D and its characterisations. The total density of the cluster jet was estimated with a Mach-Zehnder interferometer to be below  $1.7 \times 10^{18} \text{ cm}^{-3}$  which is in good agreement with the calculated predictions. Measurements of Mie-scattered light were used to determine the cluster size distributions for stagnation conditions in the gaseous regime. The prediction of the mean cluster sizes by the Hagena scaling law was slightly adjusted to the used gas and hardware. The cluster sizes for stagnation conditions in the liquid regime were determined by a shadowgraphy measurement showing a good agreement with the predictions by the atomisation process. The interaction probability of a strongly focused short laser pulse with a micrometer sized cluster was calculated based on these measurements, resulting in the expectation for not a single observed interaction. A larger laser focus volume is necessary to reach a better interaction probability. The temperature depending fraction of the micrometer sized clusters of the total gas flow was calculated. Since these clusters are expected to not participate in the laser cluster interaction, the effective density of the cluster jet is reduced for stagnation conditions in the liquid regime. The fraction of micrometer sized

### *3 Cryogenic cluster jet targets*

---

clusters to the total gas flow increases for lower temperatures resulting in the prediction of lower effective densities for lower temperatures.

# 4 The ARCTURUS laser system

The laser system used in the scope of this work is the ARCTURUS laser system of the Institute for Laser and Plasma Physics (ILPP) of the Heinrich-Heine University (HHU) Düsseldorf. The ARCTURUS laser system was built in 2008 and received two major upgrades by 2019. It is used for various experiments featuring solid [K<sup>+</sup>19], gaseous [Bra17, Sch18], droplet [S<sup>+</sup>19] and cluster [Gri18, A<sup>+</sup>19] targets. This chapter gives a short overview of the operation principle of the ARCTURUS laser system and characterises the laser pulses generated. It is based on [C<sup>+</sup>19] where a most detailed up-to-date description of the ARCTURUS laser system can be found.

## 4.1 Pre-amplification

The seed of every laser pulse is generated by a Ti:Sa oscillator pumped by a solid state laser. These seeds have a pulse energy of 5 nJ, a pulse length of around 20 fs and a repetition rate of 76 MHz. This frequency is much too high for the following amplification stages and thus a Pockels cell picks pulses at 10 Hz. An Öffner-type stretcher increases the pulse length of the picked pulses to about 500 ps for the first CPA stage and an acousto-optic programmable dispersive filter (Dazzler) shapes the spectrum. The first CPA stage consists of a 14-pass amplifier pumped by a Nd:YAG pump laser in second harmonics mode, a regenerative amplifier and a multi-pass 'butterfly' amplifier. After this first stage the pulses are re-compressed to around 40 fs and have an energy of around 3 mJ. A cross-polarised wave (XPW) module enhancing the pulse contrast and broadening the spectrum is located in the transition beam line leading to the main amplification. A schematic view of the ARCTURUS laser system is depicted in figure 4.1.

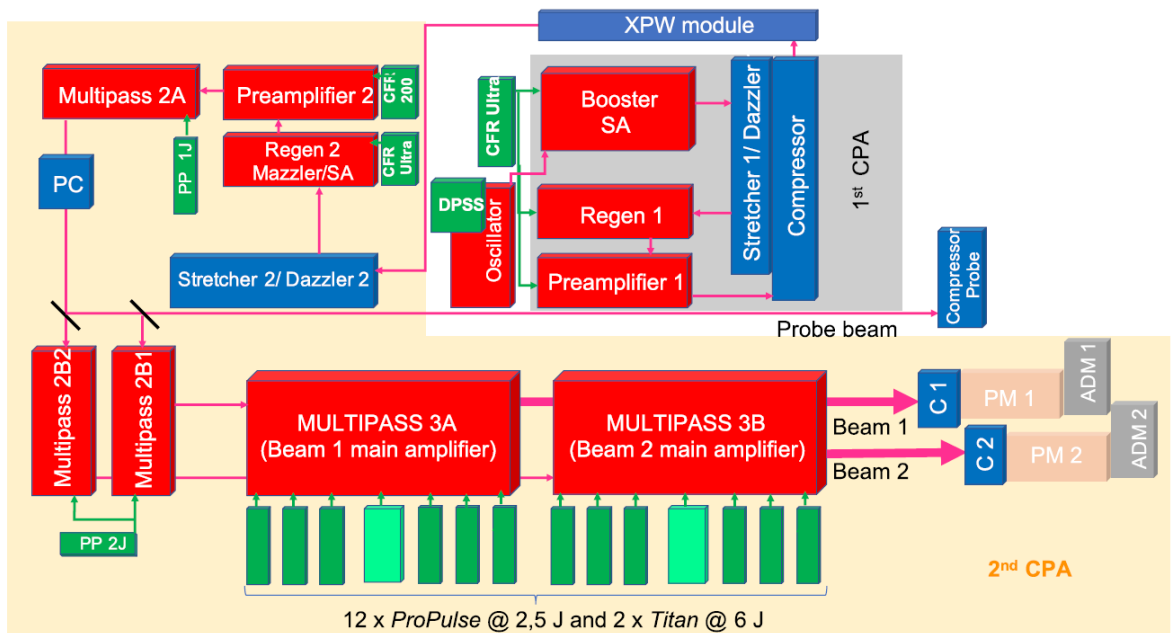


**Figure 4.1** – Schematic view of the ARCTURUS laser system with a Ti:Sa oscillator as pulse source in the center, the first amplification stage highlighted in grey in the top right corner and the main amplification stage highlighted in cream white. The amplification components are depicted in red while the pump lasers are shown in green and all components concerning the pulse duration and spectral width are illustrated in blue [C<sup>+</sup>19].

## 4.2 Main-amplification

In the main amplification stage of the ARCTURUS laser the incoming laser pulses are stretched by another Öffner-type stretcher to 10 ps/nm bandwidth and another acousto-optic modulator (Dazzler) compensates the spectral phase to keep a broad spectrum. After a regenerative amplifier and another acousto-optical modulator (Mazzler), two four-pass amplifiers, pumped by additional Nd:YAG lasers, increase the pulse energy to 300 mJ. At this point the pulses are split into three beams. One of them is the probe beam. It is guided directly to a pulse compressor under vacuum and then further to the experimental hall. The other two beams are guided parallel to each other to another amplification stage. The laser beams leave this stage, consisting of two identical four-pass amplifiers, with 400 mJ pulse energy and enter the two identical main amplifiers. The main amplifiers are large-scale, four-pass amplifiers with a  $5 \times 5 \times 3 \text{ cm}^3$  Ti:Sa crystal each. Each of these crystals is pumped by six Pro-Pulse pump lasers and a Titan Amplitude

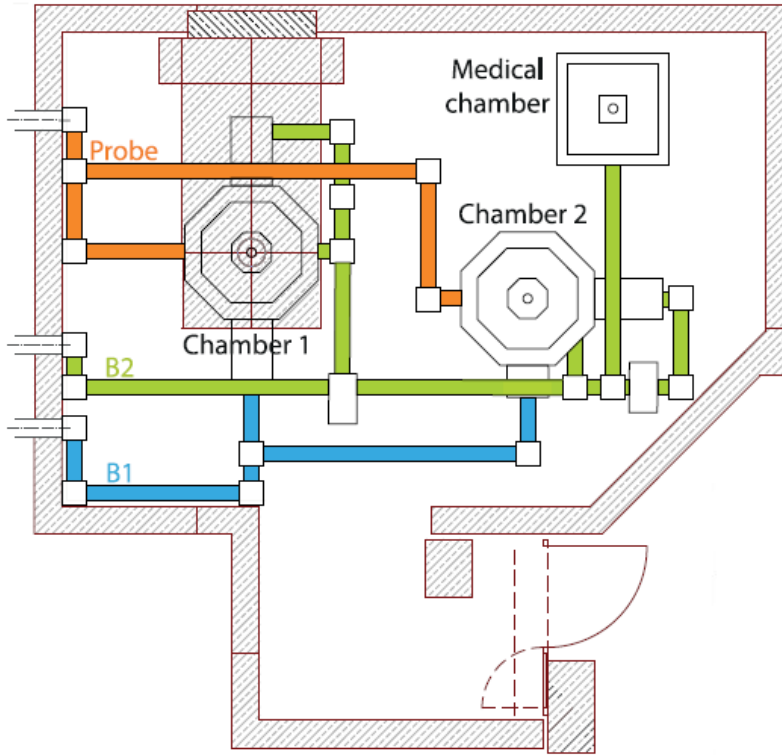


**Figure 4.2** – Floor plan of the shielded experimental hall. While all three laser beams (B1, B2 and Probe) can be guided to the two interaction chambers (Chamber 1 and Chamber 2), only Beam 2 can be guided to another interaction chamber, the Medical chamber. All measurements presented in this work have been taken at chamber 1 with the cluster jet target mounted at the left side of the chamber (at the actual position of the probe beam) perpendicular to beam B1 [C<sup>+</sup>19].

Technologies pump laser with a combined energy of 21 J per pulse. In addition, the crystals are cryogenically cooled to prevent thermal lensing. The two laser beams leave the main amplification stage with 7 J per pulse and are radially expanded to 10 cm in diameter. All three beams are separately compressed under vacuum by double-pass optical compressors to a pulse length of about 30 fs. The beams can be guided with separate beam lines into the experimental hall. A sketch of the hall is shown in figure 4.2. Once inside the shielded area, the three beam lines each lead to the two interaction chambers and beam B2 can be guided to another chamber. The measurements presented in this work have been taken at chamber 1 (cf. figure 4.2) with the cluster jet going from left to right and beam B1 from bottom to top. Since the vacuum in the interaction chamber was insufficient for the beam compression chamber and the long beam lines, a

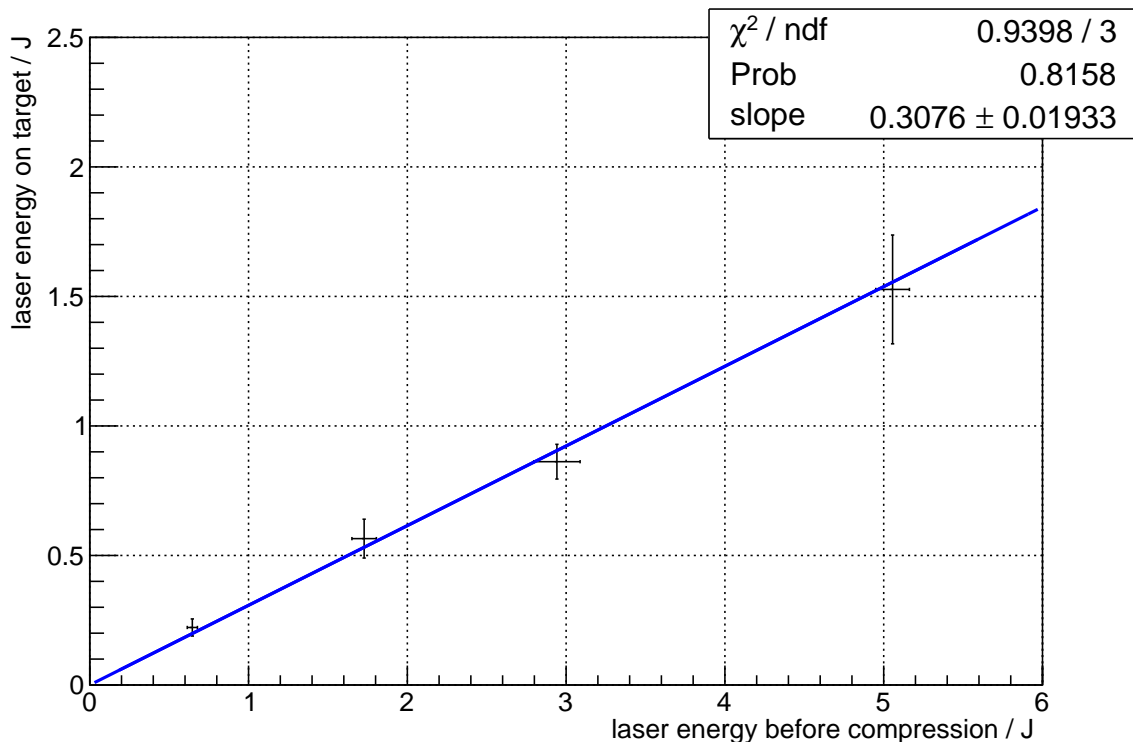


**Figure 4.3** – Laser energy measured in the interaction chamber as a function of the laser energy measured before the final compression. The slope of the linear function without offset corresponds to the beam line efficiency. The data was taken by B. Aurand and K.M. Schwind.

1mm-thick anti-reflex coated pellicle-window was inserted into the beam line in front of the interaction chamber. Measurements with a calorimeter in the interaction chamber and directly in front of the final compression, corrected by a cross-correlation of the two used calorimeters, resulted in a beam line efficiency of 30(2)%. This measurement can be seen in figure 4.3 and they were taken beforehand by B. Aurand and K.M. Schwind.

Once inside the interaction chamber, the laser pulse is focused with an  $f/2$  off-axis-parabolic mirror (OAP) onto the target. The focus volume has a minimum radius of  $\omega_0 \approx 5 \mu\text{m}$  at its centre and expands to  $\omega(z_R) = \sqrt{2}\omega_0$  at the Rayleigh length of  $z_R \approx 30 \mu\text{m}$  before and behind the centre of the focus volume. Figure 4.4 shows some example pictures of the focus spot.

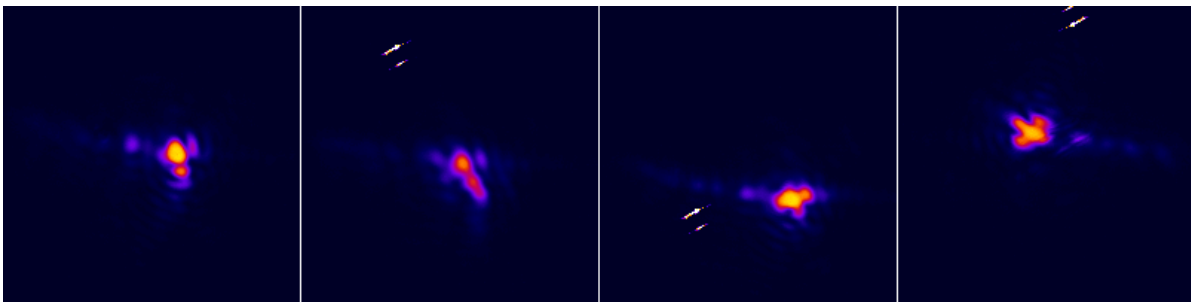


**Figure 4.4** – Four example pictures of the laser focus spot during the measuring campaign. Each picture has an edge length of roughly  $70\ \mu\text{m}$ . Images taken by K.M. Schwind.





# 5 Protons accelerated by laser-cluster interaction

Proton acceleration is an intensively studied field of researched. High energy protons are required for nuclear and particle physics experiments, as seeds for larger particle accelerators, in material science, for radiation hardness tests or for medical application as proton radiation. In conventional particle accelerators, the required proton energy is reached by letting the protons pass an alternating electric field multiple times in phase. This demands a closed loop structure resulting in a relation between diameter of the accelerator and the maximum achievable proton energy due to the energy loss by synchrotron radiation. Laser induced proton acceleration is a very promising alternative for high particle fluxes in ultra-short pulses. The electric field strength in a plasma reaches the TV/m scale, enabling a proton acceleration on a very small scale. This results in smaller facilities and may increase the availability of accelerated protons for science, industry and medicine. The most common approach for laser induced proton acceleration is the TNSA (c.f. section 2.3) using thin solid foils as the target for an ultra-short high energy laser pulse. Proton energies up to 58 MeV have been reported e.g. by [S<sup>+</sup>00]. Several groups are working on improvements of this well understood technique, e.g. [K<sup>+</sup>19] uses a special foil surface or [K<sup>+</sup>16] adds another acceleration stage via an electric pulse travelling along a coil in the same directions as the protons. While the energy achieved is very promising, foil targets come with several drawbacks. The foil is destroyed by each interaction resulting in a low repetition rate and debris which may damage the optical components in the interaction chamber. Many alternative targets such as gas-jets e.g. [PV<sup>+</sup>19], frozen droplets [S<sup>+</sup>19, A<sup>+</sup>20], solid spheres [O<sup>+</sup>16], liquid jets [G<sup>+</sup>17] and hydrogen ribbons [M<sup>+</sup>16] were already tested. Another promising target for laser induced proton acceleration is a cluster jet target. The continuous flow of clusters enables a high repetition rate and the use of pure hydrogen for the clustering process

results in a pure proton acceleration without any other ions and without any debris. After first experiments concerning laser cluster interaction by [D<sup>+</sup>96], the development of cluster jet targets has made leaps of progress. [L<sup>+</sup>06b] shows an experiment using clusters from a liquid nitrogen cooled source with a diameter below 8.8 nm resulting in proton energies below 2 keV. Precursor experiments of this work [A<sup>+</sup>19, Gri18] with a stagnation temperature down to 36 K [G<sup>+</sup>19] showed cluster diameters of up to 40 nm and easily tunable proton energies up to nearly 100 keV. Especially promising is the reported strong increase of the maximum proton energy with a decrease of the stagnation temperature, because the MCT-D is able to operate at even lower temperatures (c.f. section 3.2). [J<sup>+</sup>18] very recently reported of a cluster jet target able to operate at stagnation temperatures down to 25 K and at very high stagnation pressures. They measured the cluster sizes to be in the range of 1  $\mu\text{m}$  and showed a single proton spectrum with energies up to several MeV.

Various measurements were taken with a proton spectrometer which is presented in the first section of this chapter. A newly created evaluation routine is described thereafter including the detailed handling of systematic uncertainties. Afterwards, the measurements taken are presented and the maximum energies found are compared with the expectations of the corrected Hagena scaling law and the acceleration through a perfect Coulomb explosion as described in chapter 2.3.

## 5.1 Experimental setup

The experimental setup for measurements on proton energy spectra consists of the cluster jet target MCT-D (c.f. chapter 3.2), the ARCTURUS laser (c.f. chapter 4) perpendicular to the cluster jet and a Thomson parabola in forward direction of the laser. Another Thomson parabola under 45° with respect to the laser propagation direction was added for certain measurements. A sketch of the setup used can be seen in figure 5.1.

A Thomson parabola usually consists of a pinhole, a magnetic field, an electric field anti-parallel to the magnetic field and a detector in this order. A sketch of a Thomson parabola is depicted in figure 5.1. The pinhole defines the entrance in the Thomson parabola and can be chosen to be bigger for higher flux or smaller for a better resolution.

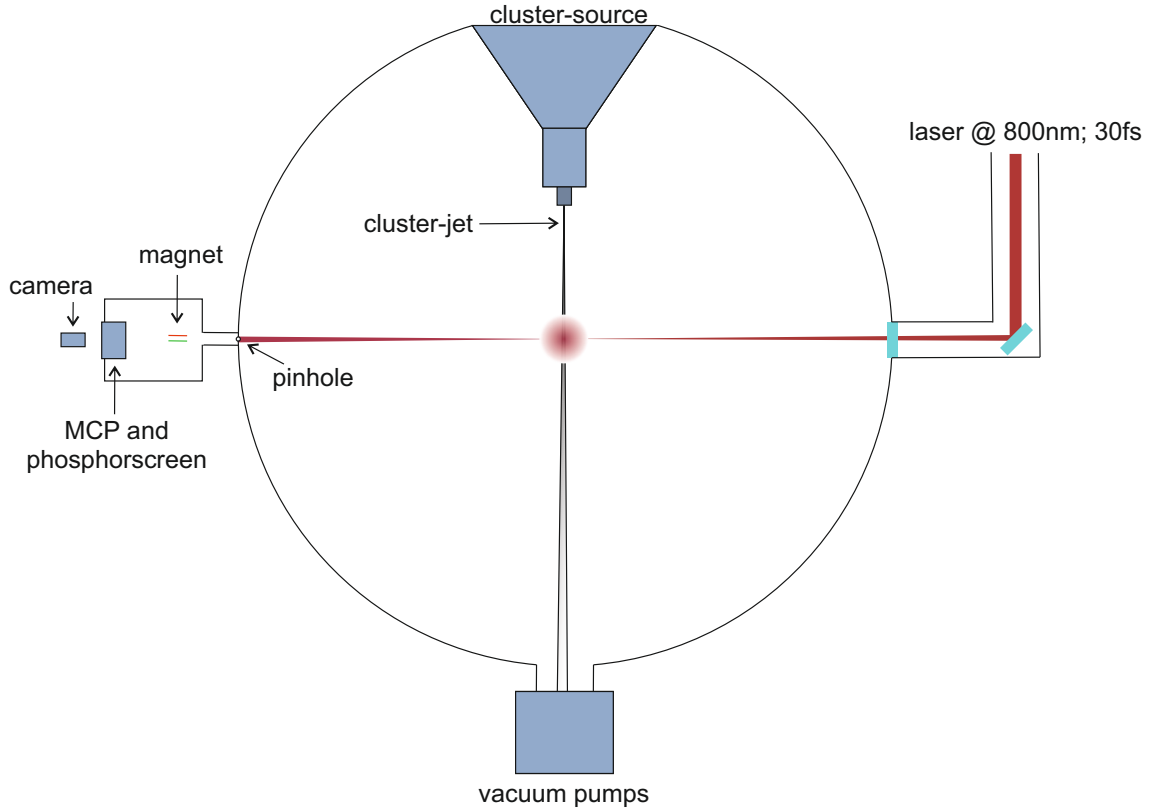


**Figure 5.1** – A sketch of the experimental setup used to detect proton energy spectra. The cluster jet propagates through the interaction vacuum chamber ( $p \approx 0.1$  mbar) and is dumped in the pumping system. The ARCTURUS laser pulse interacts with the cluster jet in the centre of the vacuum chamber and the accelerated charged particles can be detected with the Thomson parabola under  $0^\circ$  with respect to the laser propagation direction. Based on an image generated by C. Mannweiler.

In this work a pinhole with a diameter of  $250 \mu\text{m}$  has been used for a good compromise of both characteristics. The entering particles of charge  $q$  are deflected in the magnetic  $\vec{B}$  and electric  $\vec{E}$  fields by the Lorentz force

$$\vec{F}_{\text{Lorentz}} = q\vec{E} + q\vec{v}_0 \times \vec{B} \quad (5.1.1)$$

dependent on their velocity  $\vec{v}_0$  or rather on their kinetic energy. The point of impact on the detector can be calculated for non relativistic particles by assuming box shaped

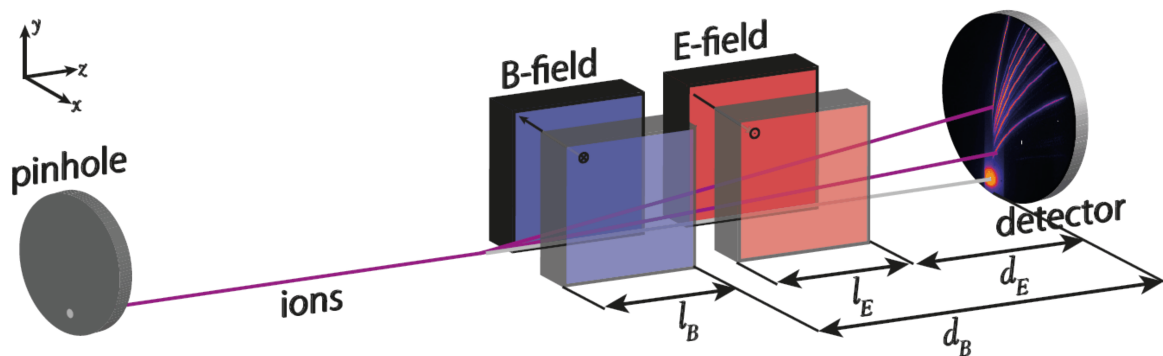


**Figure 5.2** – Technical sketch of the Thomson parabola. The generated ions enter the detector chamber through the pinhole and are deflected by the magnetic and the electric fields before they hit the detector on a position depending on their energy and specific charge [Sch18].

electric and magnetic fields of constant field strength:

$$x = \frac{q}{mv_0^2} E_0 \ell_E (d_E + \ell_E/2) \quad (5.1.2)$$

$$y = \frac{q}{mv_0} B_0 \ell_B (d_B + \ell_B/2) \quad (5.1.3)$$

The coordinates and distances used are the same as shown in figure 5.2,  $\vec{e}_z$  is the ion propagation direction,  $\vec{e}_x$  is the direction of the electric field and  $\vec{e}_y$  is perpendicular to both of them.  $\ell_{E/B}$  are the width of the corresponding field and  $d_{E/B}$  are the distances between the corresponding field and the detector. The magnetic field deflects the incoming particles only in  $\vec{e}_y$  direction depending on their energy. Faster ions are deflected less than slower ions. This results in an energy resolution in  $\vec{e}_y$  direction. The electric field splits up the ion traces depending on their charge-mass ratio  $q/m$  in  $\vec{e}_x$  direction. This results in different parabolic traces for each different ion species. Each trace keeps the energy resolution caused by the magnetic field. In this way one detector can measure the energy spectra of all generated ion species at once. While a magnetic field strength of 180 mT was used, the electric field was omitted in the scope of this work because the target material used was pure hydrogen, which consists only of individual protons and electrons.

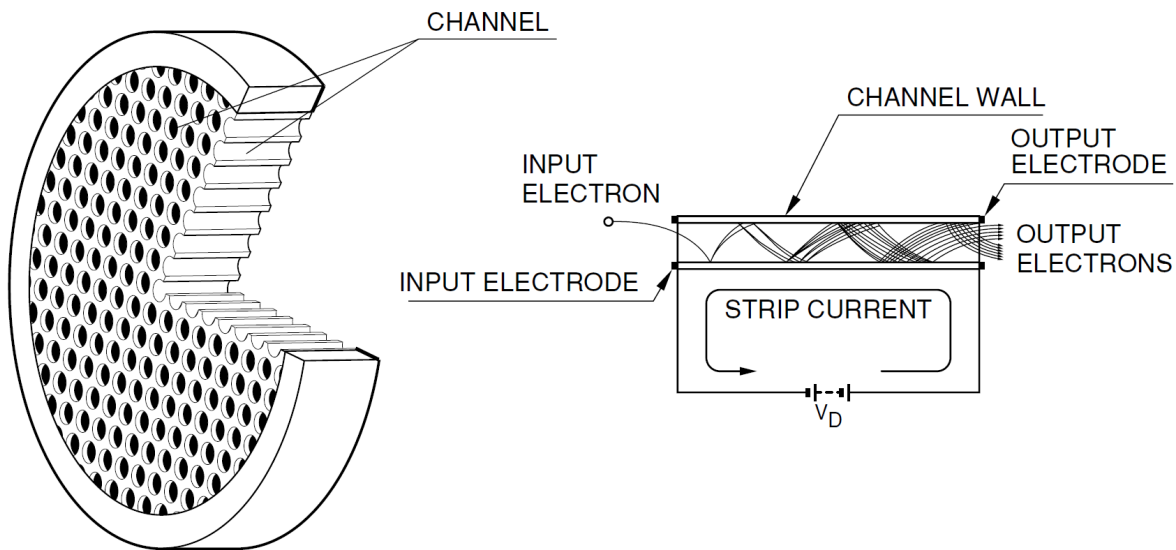


**Figure 5.3** – The left side shows a sketch of a single stage MCP. The plate is perforated by parallel tubes in a uniform pattern. These tubes are usually under a small angle to the surface normal. The right side shows the working principle of a MCP. A voltage is applied between the front and the rear surfaces generating an electric field in the tubes. Incoming particles generate electrons at their impact on the MCP and these electrons propagate in a cascade through the tube resulting in a strong and local electron signal at the output. Courtesy of Hamamatsu Photonics K.K.

A double staged micro channel plate (MCP), an MCP-88-D-R-VF-P43 by tectra GmbH, was used in combination with a P43 phosphor screen and a CCD camera to detect the ion trace behind the magnetic field. MCPs are thin plates with a uniform pattern of tubes from the front side to the rear side. The tubes are under a small angle of  $6-10^\circ$  to the surface normal and parallel to each other. A high voltage is applied between front and rear side of the plate causing an electric field in the tubes. Incoming particles may generate electrons at their impact on the MCP, which propagate, accelerated by the electric field, through the tubes in a cascade. A schematic view of an MCP and a sketch of the multiplication process can be seen in figure 5.3. The spacial resolution of the incoming particles is sustained by the MCP while the signal is enhanced by a factor of the order  $10^6$ . This strong electron signal is converted to a visible signal by the phosphor screen. The phosphor screen is excited by the incoming electrons and returns to its ground state under emission of photons of 545 nm wavelength over 1 ms. This phosphorescence is recorded by the camera using a trigger connected to the laser trigger.

## 5.2 Evaluation method

The images of the phosphor screen are evaluated in several steps. Figure 5.4 shows a raw data image taken at 16 bar, 34 K and 5 J laser energy before pulse compression with the evaluated region of interest marked in green. At first, projections of the zero spot to the different axes and the best fit of Gauss functions determine the position of the zero spot. Figure 5.5 shows the two projections of the example shot. The x position is needed as a starting parameter later and the y position is used as the reference point for the energy calculation using formula 5.1.3. The quality of the best fits is very bad since the uncertainties of the intensity is not known. Therefore, the uncertainties of the fit parameters are not very precisely calculated. But it is not necessary to improve this, since the resulting energy uncertainty will be statistically distributed and thus be part of the later calculated standard deviation of multiple shots. Afterwards every pixel row is evaluated separately. The region of the signal is fitted with a combination of an asymmetric Gauss function for the signal and a linear function describing the background. Figure 5.6 shows three examples with different signal to background ratios for this routine. The significance of the fit compared to a linear background function is calculated. For a significance above  $3\sigma$  the signal is considered to be significant and the signal intensity is counted in a fixed area around the zero spot x position while subtracting the fitted linear function as the local background value. The counted signal is corrected to 100% of the integral of the asymmetric Gauss function by multiplying the counted signal with the inverse of the counted integral fraction for both sides

$$\frac{A_{\text{left, counted}}}{A_{\text{left, total}}} = \text{erf} \left( \frac{\text{mean} - x_{\text{start}}}{\sqrt{2}\sigma_{\text{left}}} \right) \quad (5.2.1)$$

$$\frac{A_{\text{right, counted}}}{A_{\text{right, total}}} = \text{erf} \left( \frac{x_{\text{end}} - \text{mean}}{\sqrt{2}\sigma_{\text{right}}} \right) \quad (5.2.2)$$

with the fitted peak position *mean* and the borders of the counted area  $x_{\text{start}}$  and  $x_{\text{end}}$ . Lower significances are considered as no signal and lead to a cut-off in the spectrum if the respective significances of three neighbouring pixel rows are too low. The distance of the evaluated pixel row to the zero spot y position is used to calculate the corresponding energy of the measured protons by using formula 5.1.3. The fit parameters and the

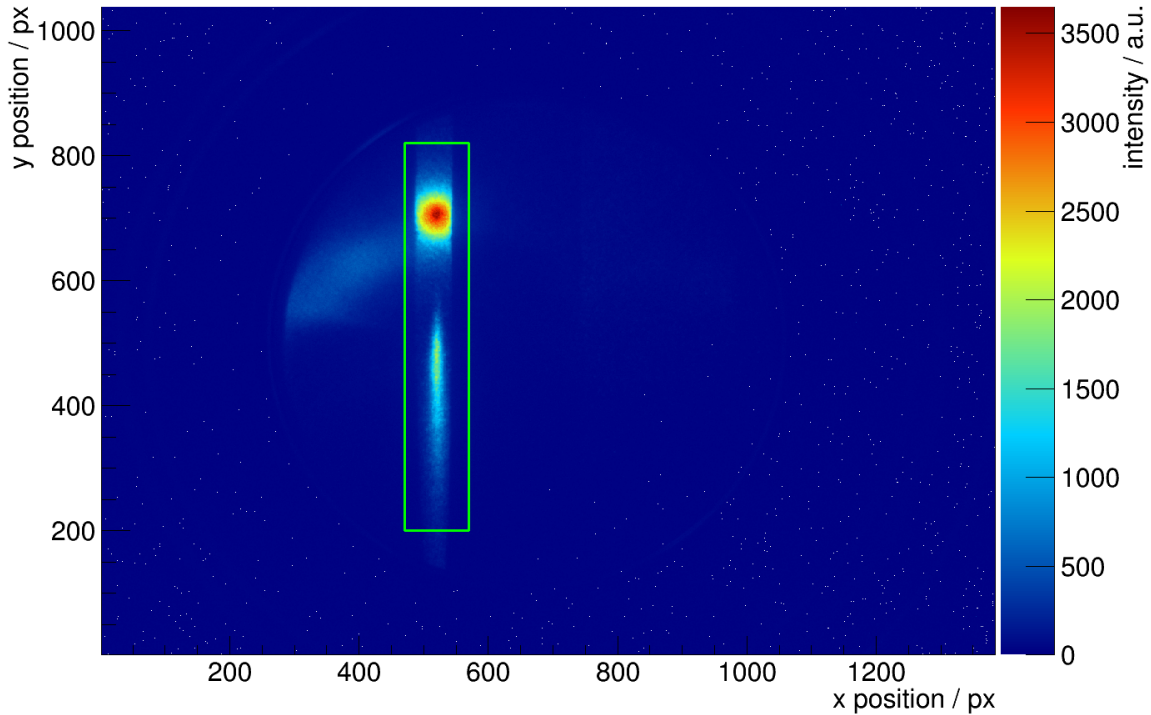


**Figure 5.4** – Raw data image of the phosphor screen after a single laser shot with 5 J energy before compression on the cluster jet operated at 16 bar and 34 K. The signal area is marked with a green box. In the higher region of the signal area is the zero spot generated by neutral particles and below is a signal trace. Outside of the signal box is another area with higher intensity. This is caused by a gas discharge of hydrogen gas in the MCP.

calculated significances of the signal fit of all pixel rows are shown in figure 5.7. Position and width of the signal show non-physical fluctuations supporting the cut-off position found by the significance. The trend of the fit significance shows a clear signal peak at lower energies.

For the conversion of the counted signal  $s$  to a proton flux  $\frac{dN}{dE}$  the calibration of A.-M. Schroer [Sch18] was used. She used a slotted CR-39 plate in front of the MCP to compare the signal on the data image with the signal on the well known CR-39 detector. She found a conversion factor of  $k_0 \sim 7.32$  counts/proton for the double stage MCP used for the Thomson parabola in laser propagation direction. The proton flux is calculated as

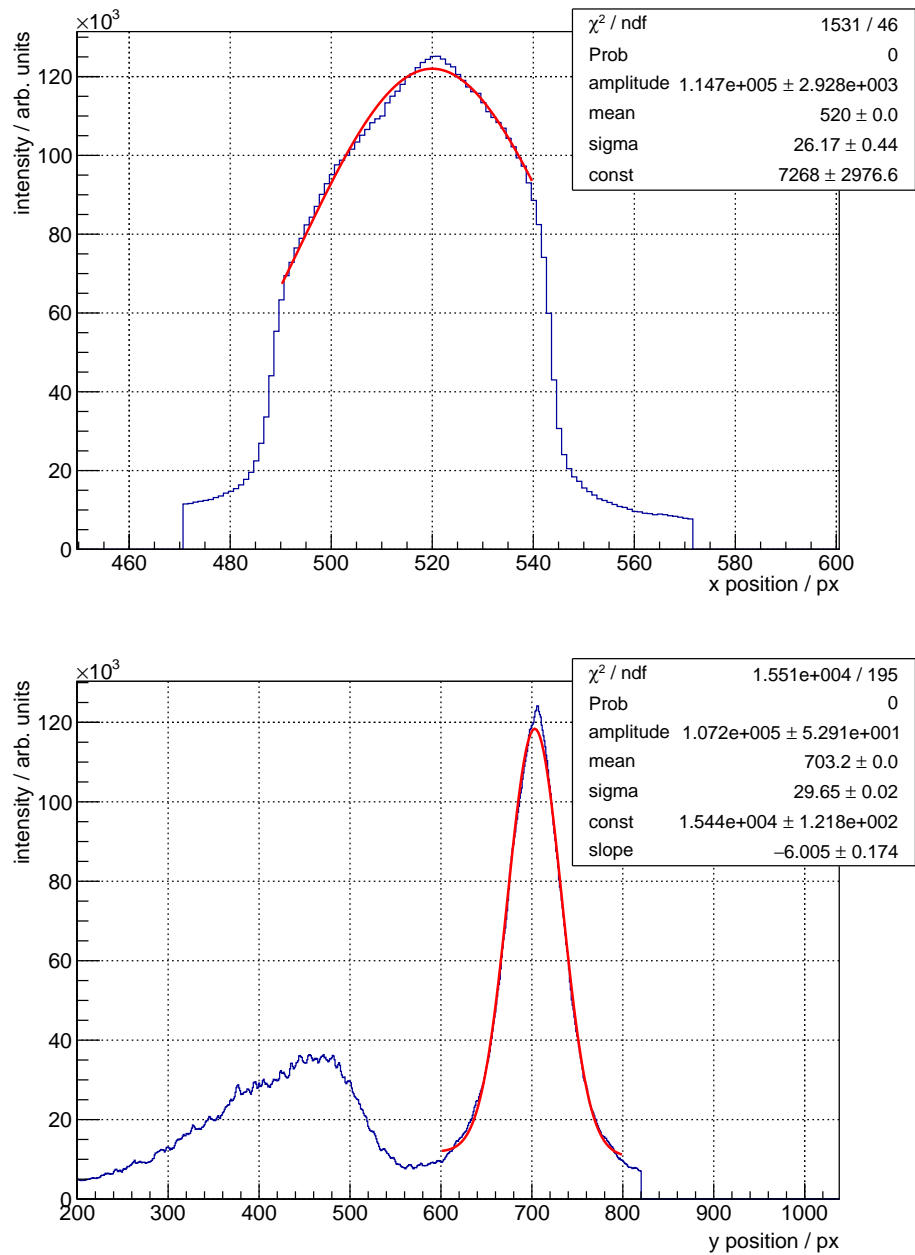


**Figure 5.5** – Projections of the area of the zero spot on both axis. The top shows the projection on the horizontal axis. The sharp edges around 470 px and 570 px are caused by evaluating only the signal box. The steep flanks of the projection are caused by the width of the magnet used. The bottom shows the projection on the vertical axis. The projection of the signal trace can be seen between 200 px and 550 px. Gauss functions are fitted to the centre of the projections to get the position of the zero spot.



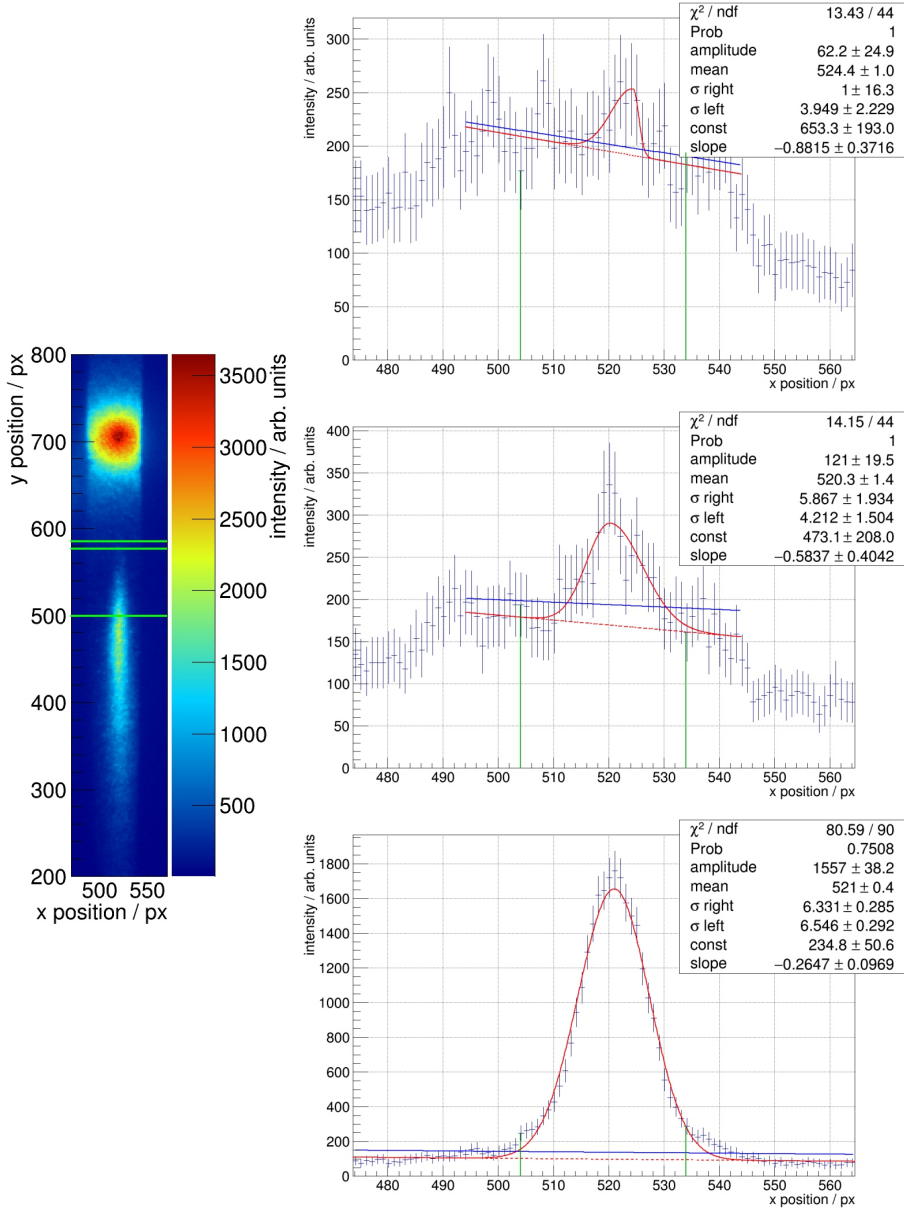


**Figure 5.6** – Three example projections of single pixel rows of the signal trace on the horizontal axis. Shown are the pixel rows 500, 577 and 585 from bottom to top. The corresponding rows are marked in green in the raw data image on the left side. The intensity uncertainties are calculated from the statistical uncertainties of the detected proton number using the conversion factor  $k \sim 7.32$  counts/proton. From  $I = k * N_{\text{protons}}$  and  $dN_{\text{protons}} = \sqrt{N_{\text{protons}}}$  follows  $dI = \sqrt{kI}$ . The single projections are fitted with an asymmetric Gauss function and a linear background function, respectively. The combined function is shown in red, while the background part of the fit is shown as a dashed line. A linear background only fit for a significance check is plotted in blue. The two green lines mark the constant area for counting the background reduced signal. While the bottom shows a very clear signal above a small background resulting in a huge significance, the projection in the middle still shows a significant signal and the upper projection shows no significant signal at all.

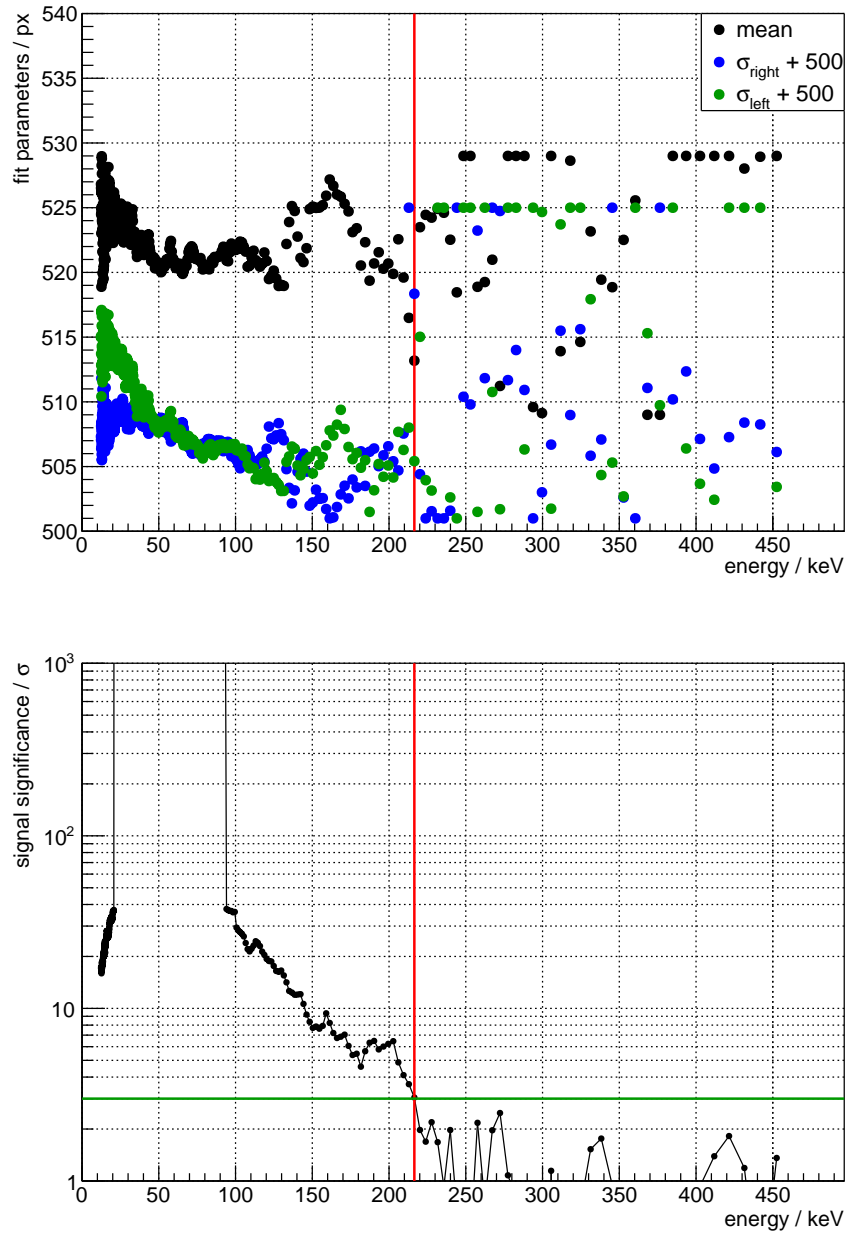


**Figure 5.7** – Results of the signal fits on the single projections of the signal trace. The top graph shows the position and width parameters of the fitted signal function over the evaluated energy range. All parameters show non-physical fluctuations beyond the cut-off energy marked with the red line. The lower graph shows the calculated signal significances over the evaluated energy range. The significance values for lower energies (30-90 keV) are several orders of magnitude higher and not shown here for simplicity. The green line marks the cut-off constraint of  $3\sigma$  and the red line marks the cut-off energy found.

$$\frac{dN}{dE} = \frac{s}{k \Omega_{\text{detector}}} \frac{1 \text{ MeV}}{\Delta E} \quad (5.2.3)$$

with the solid angle covered by the detector  $\Omega_{\text{detector}}$  and the energy range covered by the corresponding pixel row  $\Delta E$ . Figure 5.8 shows the counted raw signal with a linear axis and the converted proton flux with a logarithmic axis of the example shot.

### 5.2.1 Systematic uncertainties

Since the fit area for the signal fit and the background function was chosen arbitrarily, additional systematic uncertainties may occur during the evaluation process. Both parameters were varied slightly and the effect along a whole temperature scan was studied. The fit area width was varied from the nominal value of 30 px to values between 24 px and 36 px. The smallest fit area still includes the whole signal peak and the widest fit area ends at the signal drop caused by the magnet. The order of the background polynomial was increased and decreased by one. Higher order polynomials were tested, too, but the higher order coefficients stayed negligible small. Figure 5.9 shows the ratio of the obtained cut-off energies and the nominal cut-off energy  $R_i = E_{\text{cut-off},i}/E_{\text{cut-off,ref}}$  for some representative example temperatures. No significant dependence of the cut-off energy on the fit area or on the background function can be observed for any temperature.

The systematic uncertainties are calculated by

$$\sigma_{\text{sys}}^2 = \frac{\sum_i \omega_i^2 (1 - R_i)^2}{\sum_i \omega_i^2} \quad (5.2.4)$$

with  $\omega_i = (\Delta R_i)^{-1}$  using the standard deviation  $\Delta R_i$  from five shots per temperature. The standard deviation of multiple shots includes uncertainties from fluctuations of the laser energy or the target density. Figure 5.10 shows the calculated systematic uncertainties and the standard deviations for the evaluated temperature scan. While the choice of

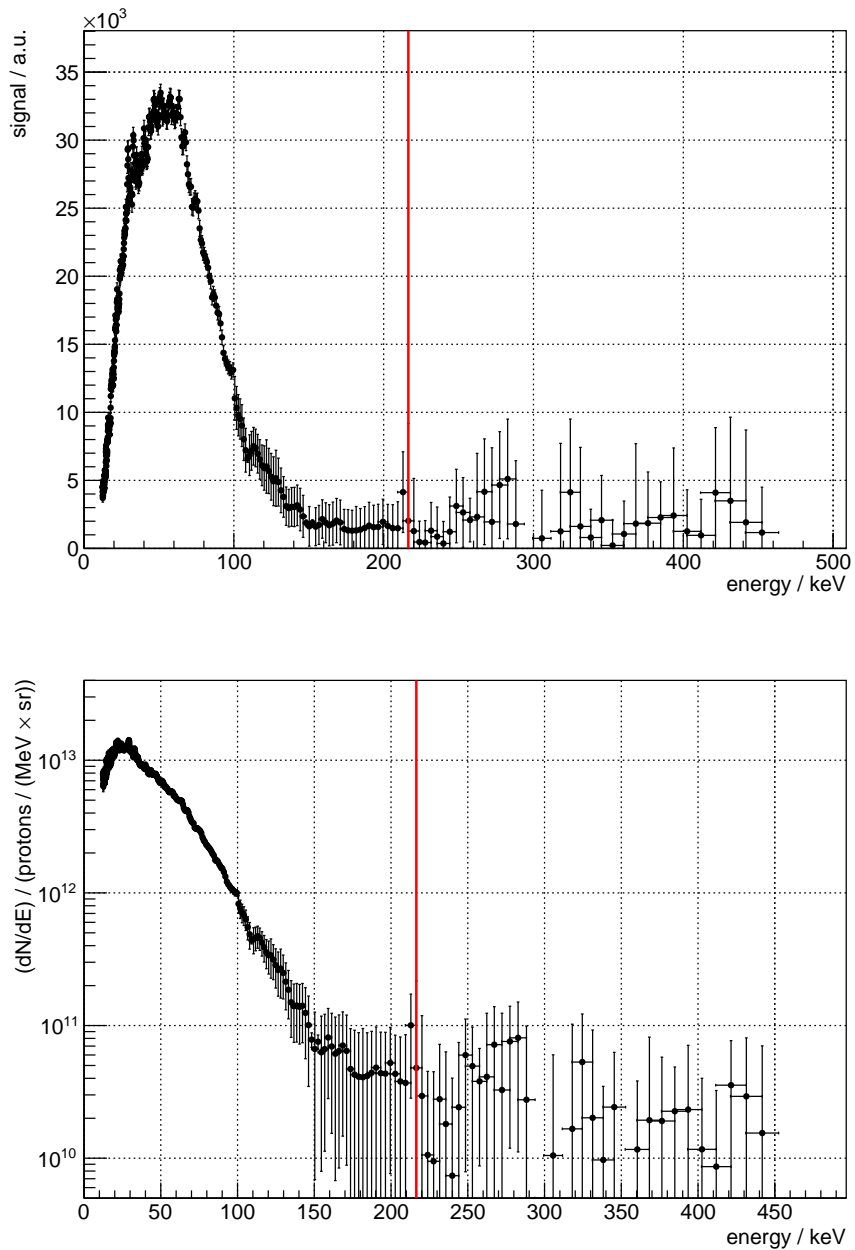


**Figure 5.8** – Counted and corrected signal and proton flux of the evaluated example spectrum. The red line marks the found cut-off energy in both graphs. The top graph shows the raw signal over the evaluated energy range with a linear axis and the bottom graph shows the converted proton flux using equation 5.2.3 with a logarithmic axis. The signal uncertainties are calculated from the uncertainties of the fit parameters of the signal fit.

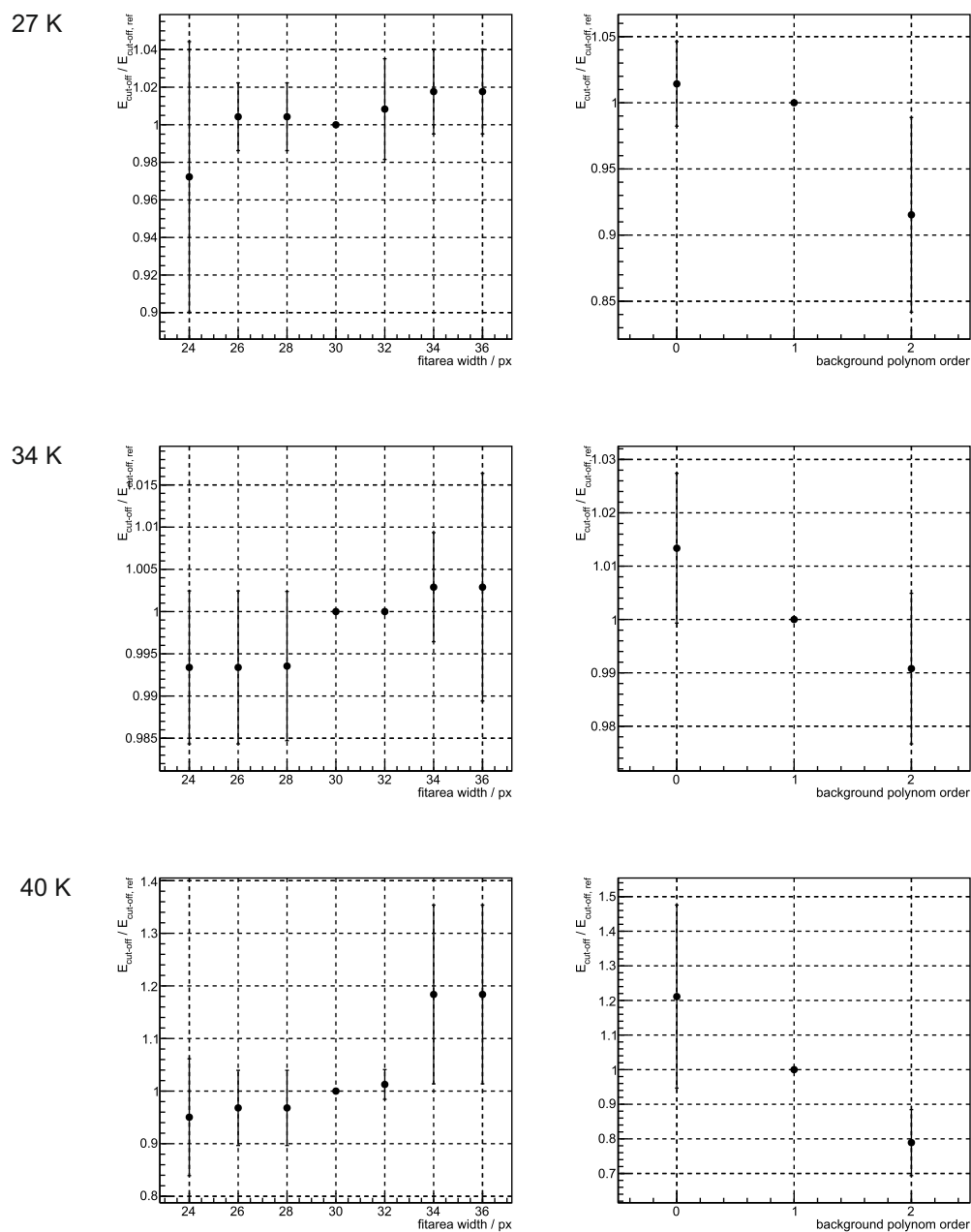


**Figure 5.9** – Ratio plots for the determination of systematic uncertainties. The left side shows the effect of varying the fitting range and the right side shows the effect of varying the background function. The rows correspond to the parameters 5 J, 16 bar and from top to bottom 27 K, 34 K and 40 K.

the fit region has nearly no systematic effect, the chosen background functions results in systematic uncertainty nearly as high as the standard deviation. The mean combined value of the systematic uncertainties is 10.4% while the mean standard deviation is 15.9%. This results in a mean total uncertainty of 19.9%.

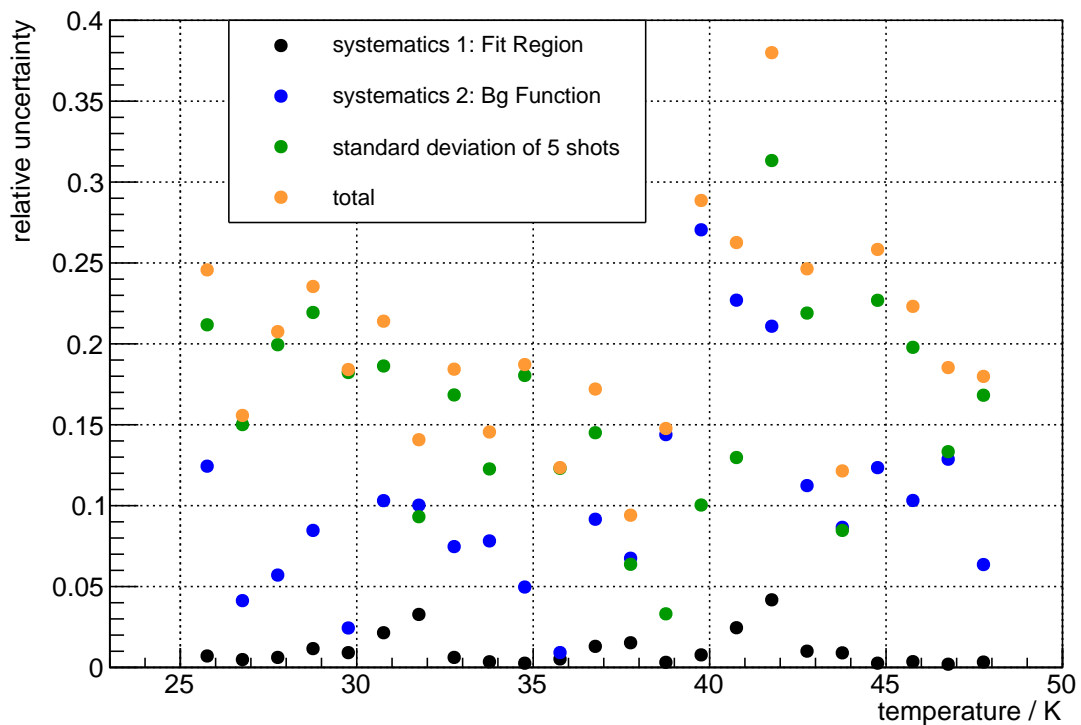


**Figure 5.10** – Summary of the calculated systematic uncertainties and the standard deviations of the evaluated temperature scan by temperature. The mean combined value of the systematic uncertainties is 10.4% while the mean statistical uncertainty is 15.9%. This results in a mean total uncertainty of 19.9%.

## 5.3 Proton data

This section presents measurements of proton spectra taken with the experimental setup shown at the beginning of this chapter and evaluated with the method presented previously. Apart from tests of the stability, variations of the cluster jet's stagnation conditions (pressure and temperature) and of the laser parameters (pulse energy and pulse duration) are presented.

### Stability scans

The first kind of measurements taken are stability scans. 50 shots per scan were taken per set of target and laser parameters. All stability scans were taken at a laser pulse energy of roughly 5 J before compression, a laser pulse length of approximately 30 fs, a high backing pressure of 16 bar and variable stagnation temperatures of the cluster jet. Figure 5.11 shows three examples while the remaining scans are shown in the appendix A.2. The left side shows the proton spectra evaluated with the routine presented in the previous section and the right side shows the corresponding cut-off energies, respectively. The 50 proton spectra per scan differ only slightly and the cut-off energies of the stability scans show the same small deviations. Table 5.1 shows the evaluated mean cut-off energies of all stability scans taken in comparison with a theoretical value calculated by the predicted mean cluster size using the Hagen scaling law (see formula 3.1.22) and the acceleration by a perfect Coulomb explosion of these clusters (see formula 2.3.6).

### Temperature scans

For the next measurement series the laser parameters (5 J before compression, 30 fs) and the stagnation pressure (16 bar) of the cluster jet were kept constant and the stagnation temperature was varied over a wide range including the gaseous, hypercritical and liquid regimes. Five shots were taken at each temperature per scan and two scans were recorded, one starting with the lowest temperature and the other starting with the highest temperature. Figure 5.12 shows the proton spectra of some example shots for different temperatures and figure 5.13 shows the cut-off energies of both scans versus

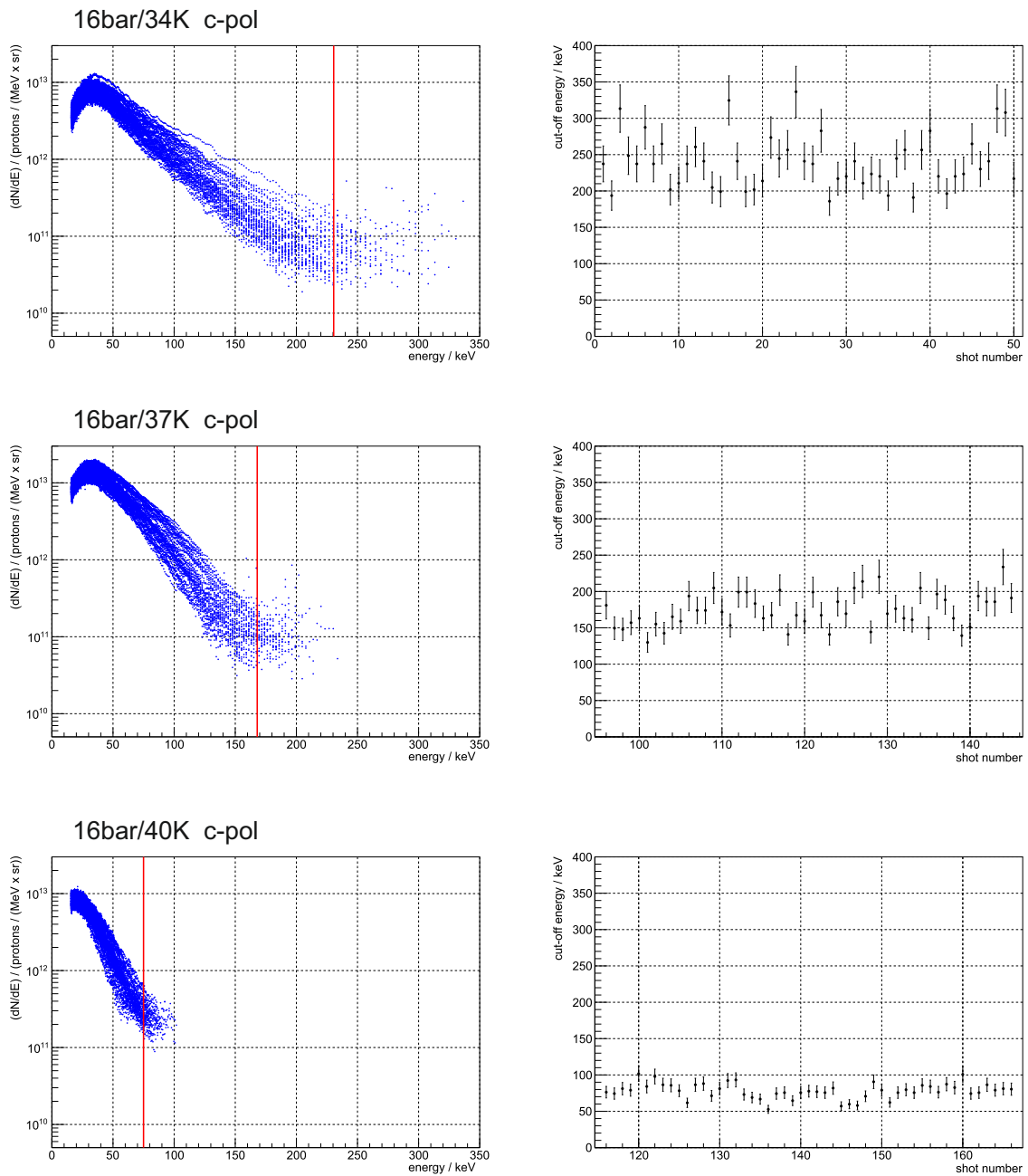


**Figure 5.11** – Three example stability scans. The stagnation conditions of the cluster jet were (from top to bottom) 16 bar and 25 K, 16 bar and 34 K and 16 bar and 40 K. The left side shows the 50 proton spectra of the stability scan with the mean cut-off energy marked with the red line and the right side shows the corresponding cut-off energies of the single shots in the scans.



**Table 5.1** – Mean proton cut-off energies of the stability scans in comparison with a theoretical value. The top five scans were taken with a circular polarised (c-pol) laser pulse and the lower five were taken with a parallel polarised (p-pol) laser pulse. All scans were taken at a backing pressure of 16 bar and at a laser pulse energy of roughly 5 J before compression. The scan taken at 25 K has no corresponding theoretical value since these stagnation conditions correspond to the liquid regime where no estimations concerning mean cluster sizes can be made.

temperature / K	cut-off energy / keV	theoretical value / keV
c-pol		
34	177(25)	157
35.5	186(32)	135
37	129(25)	117
38.5	82(23)	102
40	57(15)	90
p-pol		
25	301(49)	
35.5	167(29)	135
37	124(23)	117
38.5	80(21)	102
40	70(17)	90

the corresponding stagnation temperatures including the mean cut-off energies of the stability scans. The same theoretical value as before has been plotted as a function of the temperature for a comparison with the data in the gaseous regime. Since these and some of the following measurements were recorded simultaneously with another Thomson parabola under  $45^\circ$  with respect to the laser propagation direction, the cut-off energies found in this data are plotted, too. The evaluation of the data taken under  $45^\circ$  was done in the same way as presented for the data taken under  $0^\circ$  (presented before in this chapter), but another calibration (counts  $\rightarrow$  protons) is missing. Therefore, the spectra were scaled with a global and constant factor to match the data taken under  $0^\circ$ . This works very well and can be seen in the appendix A.1. In the following only the evaluated cut-off energies found under  $45^\circ$  will be shown in addition to the data taken under  $0^\circ$ .

Two major trends can be seen in the data of the temperature scans. The first one is the strong rise of the cut-off energy with decreasing temperature in the gaseous regime ( $T > 36$  K) while the proton spectrum gets not only wider but the overall flux increases,

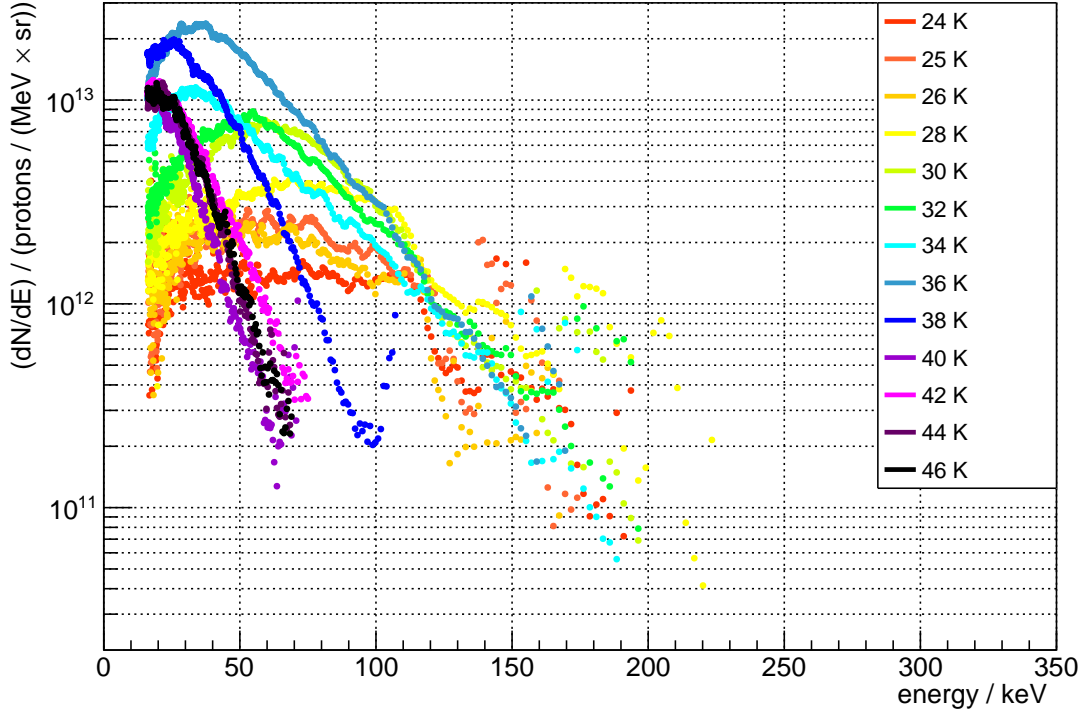


**Figure 5.12** – Some example proton spectra at different stagnation temperatures of the cluster jet. With decreasing temperature, the spectra increase in width and amplitude as long as the temperature corresponds to the gaseous regime. This trend changes in the hypercritical and liquid regime ( $T < 36$  K) to a decrease of the amplitude of the spectra while the width of the spectra stay the same.

too. This corresponds to bigger clusters in the cluster jet (higher cut-off energy) and a higher density of the cluster jet (higher proton flux). This trend was already observed before [Gri18, A<sup>+</sup>19] and motivated this work and the low design temperature of the MCT-D. Both parts of this first observation fit very well with the expectation to the cluster jet. The Hagen law predicts bigger clusters for lower temperatures  $\bar{d}_{\text{Cl}} \propto T^{-1.79}$  (see equation 3.1.22) and the gas flow theory predicts a higher density of the cluster jet for lower temperature  $\rho \propto (q_V \cdot \sqrt{T})^{-1}$  (see equation 3.1.17). The second trend in the data can be found at even lower temperatures ( $T < 36$  K) and thus in the hypercritical and liquid regime. A further decrease in temperature does not change the cut-off energy (width of the spectrum) any longer but the amplitude of the proton spectrum decreases. This corresponds to a lower effective density of the cluster jet, which seems to be in

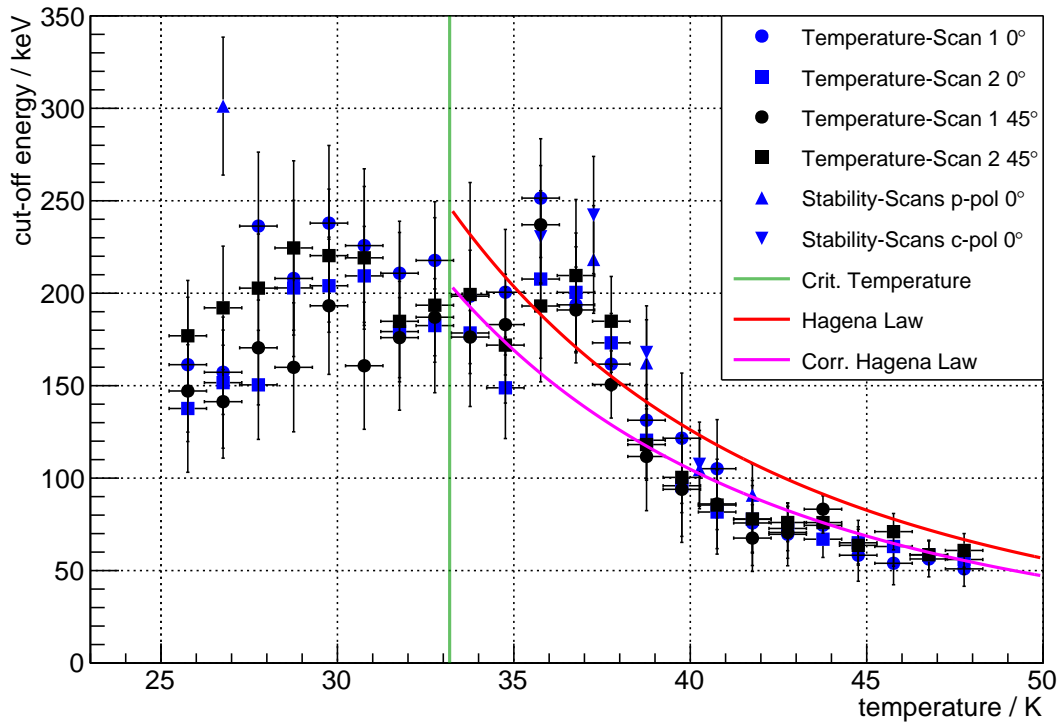


**Figure 5.13** – Cut-off energies of the two temperature scans and of all stability measurements taken. The gray dots and squares are the cut-off energies of single shots while the black dots and squares are the weighted mean values of the five corresponding single shots. Both temperature scans and the stability measurements match very well and fit to the theoretical expectations for higher temperatures of the Hagedorn scaling law and a pure Coulomb explosion. Temperatures slightly above the critical temperature ( $T_C < T < 35$  K) correspond already to the liquid regime since the scan was taken at a pressure above the critical pressure. Temperatures even slightly higher ( $35$  K  $< T < 40$  K) correspond to the hypercritical regime, where the Hagedorn scaling law is no longer applicable.

conflict with the higher gas flow at lower temperatures corresponding to higher densities. But, as shown with the shadowgraphy measurements presented in chapter 3.5 a higher percentage of the gas is bound in the large clusters for lower temperatures (see figure 3.19) and these large clusters are not part of the interaction resulting in a lower effective density at lower temperatures. Since the micrometer sized cluster do not participate in the interaction due to their infrequency, the proton spectra taken at stagnation conditions in the liquid regime allow to draw a conclusion concerning the cluster sizes of the interacting clusters. Both the cut-off energy and the spectra shape do not differ significantly between

the proton spectra taken at different stagnation conditions in the liquid regime. Thus the cluster participating in the interactions are of a nearly temperature independent size distribution. The cut-off energies measured at stagnation condition in the liquid regime can be used to estimate the size of the smaller clusters participating in the interaction with the laser. Using equation 2.3.6 and 3.1.22 results in

$$d_{Cl.} = \sqrt{\frac{12\epsilon_0 m E}{e^2 \rho_{Cl.}}}, \quad (5.3.1)$$

which gives a cluster diameter of 56 nm for an energy of 200 keV.

### Pressure scan

After changing the stagnation temperature of the cluster jet, the impact of a change in the stagnation pressure of the cluster jet is investigated. The laser parameters were kept constant as before (5 J before compression, 30 fs) and the stagnation temperature of the cluster jet was kept at 25 K. Some example proton spectra taken at different stagnation pressures can be seen in figure 5.14 and the cut-off energies of the whole pressure scan are shown in figure 5.15. The spectra show no significant difference to each other and the cut-off energies are stable for the whole scan. The stagnation pressure has no significant impact on the sizes of the smaller clusters generated at liquid stagnation conditions.

### Scans of constant predicted mean cluster sizes

According to the Hagen scaling law there are several pairings of stagnation pressure and temperature that result in the same mean cluster diameter. For three calculated mean cluster diameters (51 nm, 56 nm, 63 nm) measurements at three to four different stagnation condition pairings were taken. Figure 5.16 shows the proton spectra and the corresponding cut-off energies of the three scans. The single measurements in the scans show similar cut-off energies. The spectra differ only from each other in shape and integral. While the integral is a measure for the target density and may

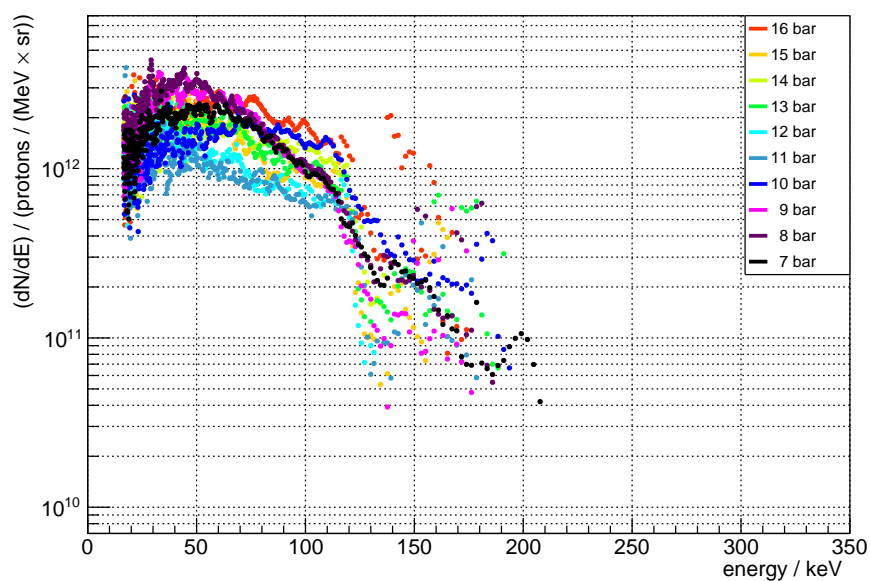


**Figure 5.14** – Some example proton spectra at different stagnation pressures of the cluster jet. The scan was taken at a laser pulse energy of 5 J before compression, a laser pulse duration of 30 fs and a stagnation temperature of the cluster jet of 25 K. There is no clear trend visible in the spectra.

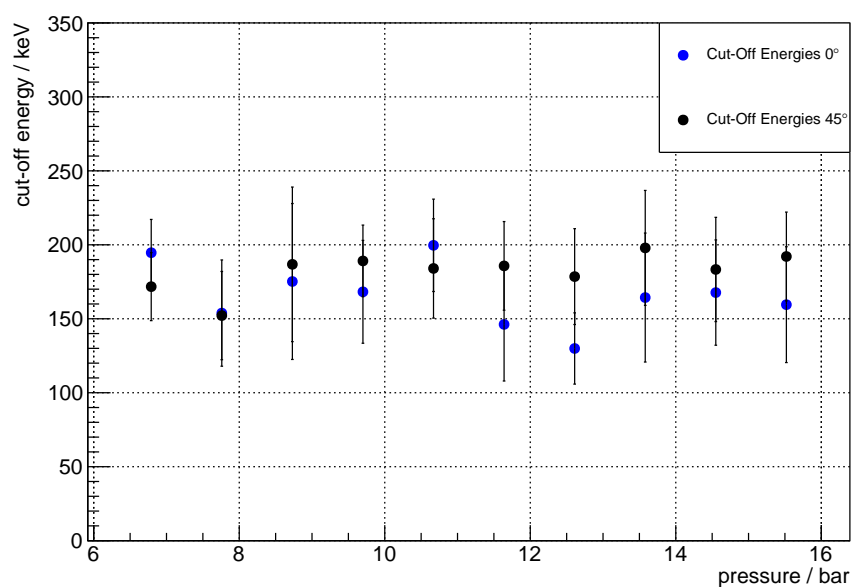


**Figure 5.15** – Cut-off energies of the pressure scan. The scan was taken at a laser pulse energy of 5 J before compression, a laser pulse duration of 30 fs and a stagnation temperature of the cluster jet of 25 K. The cut-off energies stay constant for all pressure settings measured.

change for different pairings of stagnation conditions, the shape corresponds to the cluster size distribution which seems to be not the same for the different stagnation conditions.

### **Laser pulse energy scans**

After the variation of the cluster jet parameters, the impact of a variation of the laser pulse energy was investigated. For each laser energy scan the laser pulse energy was varied by switching off single pump lasers while the laser pulse duration was kept at 30 fs and the cluster jet stagnation conditions were kept constant, too. Several measurements were taken for different stagnation conditions of the cluster jet with five shots per parameter setting. Figure 5.17 shows three examples for 16 bar and 25 K, 34 K and 40 K, respectively. The left side shows the spectra for the different laser pulse energies and the right side shows the corresponding cut-off energies. The remaining laser pulse energy scans can be found in the appendix A.3. While the spectra scale in amplitude with the laser pulse energy, the cut-off energies show only a decrease with the laser pulse energy at very low energies. The minimal laser pulse energy necessary for a pure Coulomb explosion is calculated for the given settings using formula 2.3.5 which is marked as a green line in figure 5.17. The expected behaviour would be a constant cut-off energy for all laser pulse energies beyond the green line. But the data show a decrease at very low laser pulse energies instead and the expected constant behaviour for higher energies. The corresponding proton spectra do not change in their shape. Only the amplitude of the spectra decreases for lower laser pulse energies resulting in a very low signal at higher proton energies with the same background as before. Thus, the significance of the signal is lower and may fall below the cut-off constraint of  $3\sigma$ . This results in a lower cut-off energy although the laser intensity is high enough to cause a Coulomb explosion of the same clusters and the cluster size distribution has not changed. The amplitude of the spectra was interpreted beforehand as a measure for the target density, but in this scan the target density does not change. But, since the laser amplitude is high enough to cause Coulomb explosions of the clusters even outside of the focus volume, the effective interaction volume is enlarged for higher laser pulse energies.

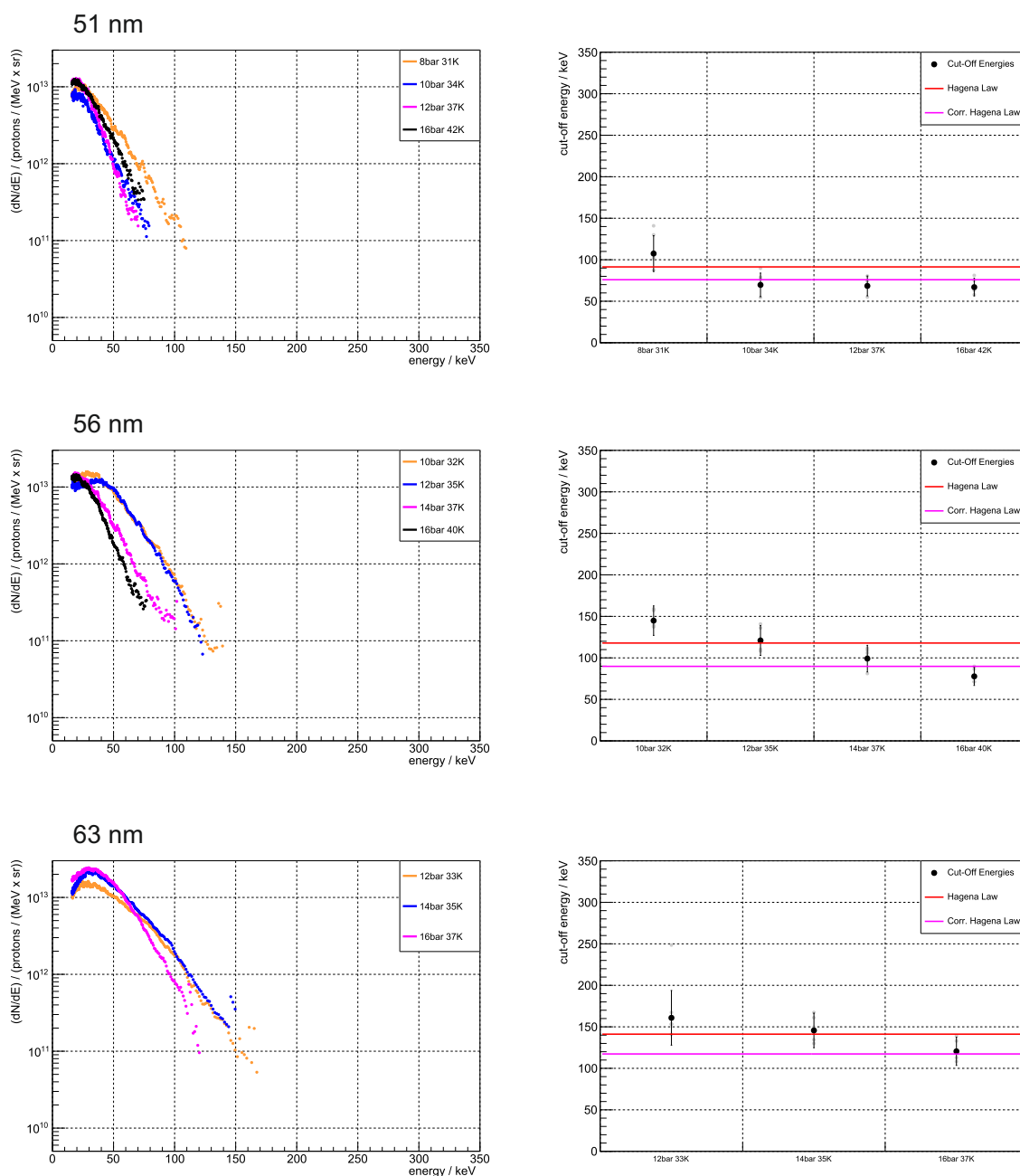


**Figure 5.16** – The left side shows the spectra and the right side shows the corresponding cut-off energies of the compared stagnation condition pairings for the same calculated mean cluster, respectively. While the top shows the different stagnation condition pairings for a mean cluster diameter of 51 nm, the middle shows the same for 56 nm and the bottom for 63 nm.

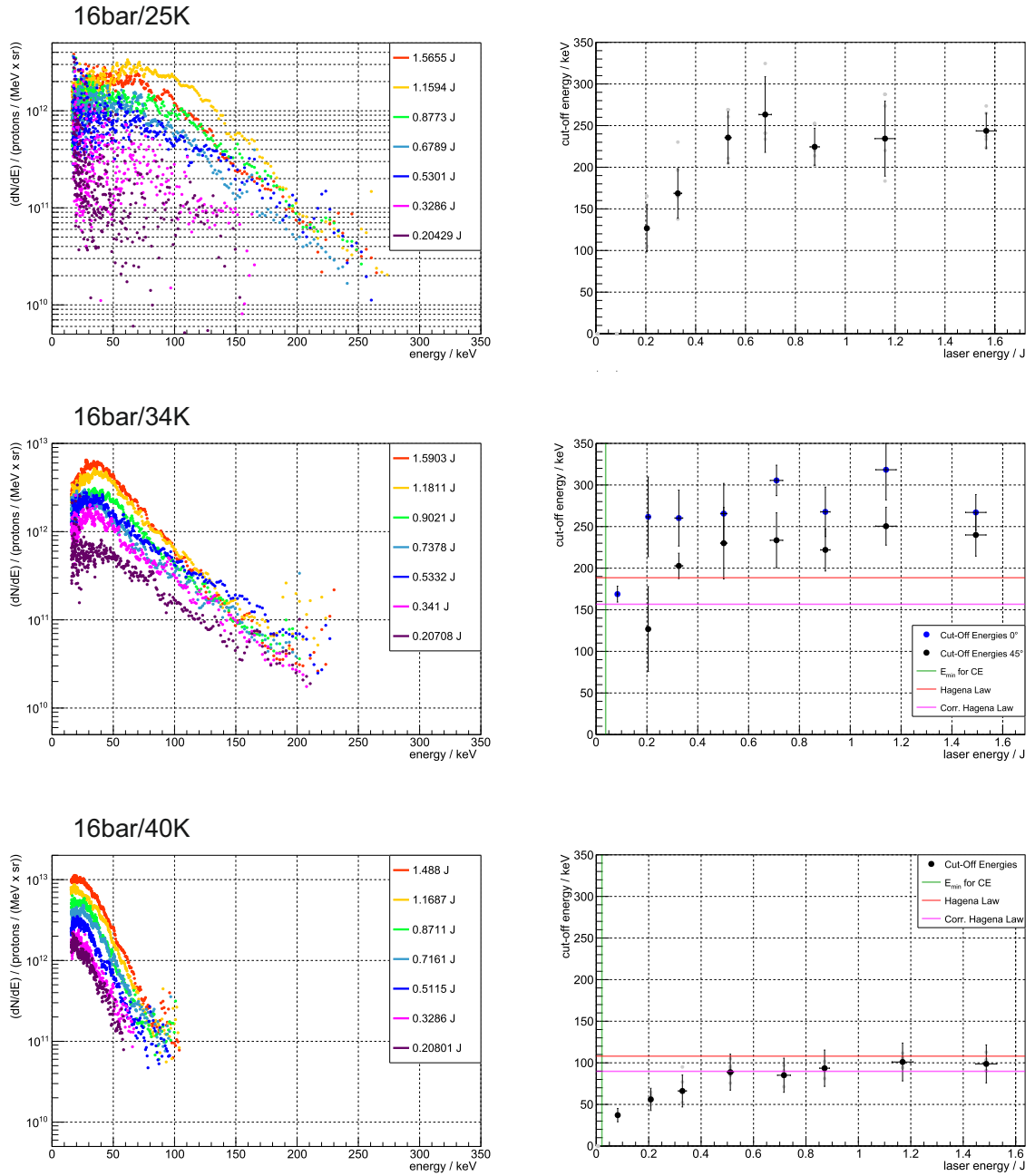


**Figure 5.17** – Three example laser pulse energy scans. The left side shows the proton spectra and the right side shows the corresponding cut-off energies of the different laser energies, respectively. The scan shown on the top was taken at 16 bar and 25 K, the scan in the middle at 16 bar and 34 K and the scan on the bottom was taken at 16 bar and 40 K. The red and magenta lines mark the expectations calculated from the Hagena scaling law and a pure Coulomb explosion with the original and the corrected parameters. The green line is drawn at the laser pulse energy necessary for a pure Coulomb explosion of the calculated mean cluster size.



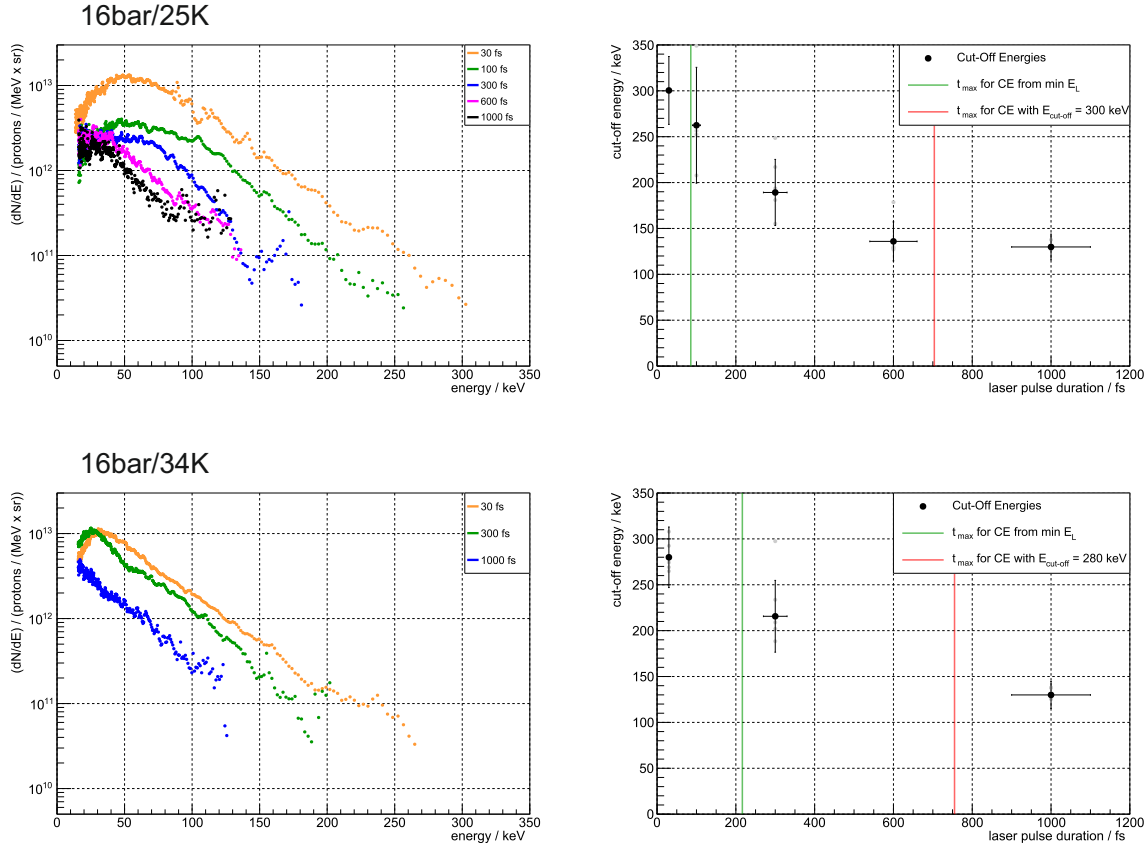


**Figure 5.18** – The two laser pulse duration scans. The left side shows the proton spectra and the right side shows the corresponding cut-off energies of the different laser pulse durations, respectively. The top shows the scan taken at a stagnation pressure of 16 bar and a stagnation temperature of 25 K and the bottom shows the scan taken at 16 bar and 34 K. The red line marks the laser pulse duration corresponding to the minimal laser intensity necessary for a Coulomb explosion reaching the maximal cut-off energy of the particular laser pulse duration scan. The green line marks the laser pulse length corresponding to the lowest laser intensity where the laser energy scan already shows the maximal cut-off energy.

### Laser pulse duration scans

Next to the variation of the laser pulse energy a variation of the laser pulse duration is possible. The impact of the laser pulse duration was investigated in two scans with constant laser pulse energy of 5 J before compression and at two different stagnation conditions of the cluster jet. The first scan was taken at 16 bar and 25 K in the liquid regime and the second scan was taken at 16 bar and 34 K in the hypercritical regime.

The proton spectra and corresponding cut-off energies are shown in figure 5.18. The red line marks the laser pulse duration corresponding to the minimal laser intensity necessary for a Coulomb explosion (c.f. formula 2.3.5) reaching the maximal cut-off energy of the particular series of measurement. The expected behaviour of the cut-off energies is staying constant below the red line and start dropping beyond it. But the data show an other progression. The cut-off energy drops way before reaching the red line. This has the same origin as the drop of the cut-off energies at low laser pulse energies observed in the laser energy scans (c.f. last paragraph). The reduction of the laser intensity by reducing the laser pulse energy or by increasing the laser pulse duration reduces the effective interaction volume, since the laser intensity is even outside of the focus volume high enough to cause Coulomb explosions of the clusters. For a cross-check with the laser energy scans, the green line is drawn. It marks the laser pulse length corresponding to the lowest laser intensity where the laser energy scan shows no drop of the cut-off energy. All measurements at lower laser pulse durations (which correspond to higher laser pulse energies in the laser energy scans) should show the same cut-off energy. The measurements at laser pulse durations between the green and the red line show a decrease in the cut-off energy because the effective interaction volume decreases and consequently the proton flux at the highest energies decreases to a non-significant amount.

## 5.4 Accelerated electrons

In the interaction of a high energy and ultra-short laser pulse with a cluster jet the atoms of the clusters are ionised while the electrons are accelerated by the ponderomotive force and the laser wakefield acceleration mechanism (c.f. chapter 2). This offers an alternative to more traditional acceleration concepts used in conventional electron accelerators, e.g. in microtrons an electric field is passed several times. Since the electric field strength reached in a plasma can be several orders of magnitude stronger than conventional electric fields [M<sup>+</sup>02], an acceleration of electrons up to the GeV scale as reported by e.g. [L<sup>+</sup>06a] is possible along a very short path length. This comes with the benefit of smaller accelerator facilities increasing the availability for industry and medicine for techniques such as electron melting, electron cutting, non-destructive inspection or radiotherapy. Usually gas jet targets are used for laser wakefield acceleration due to their tunable density and the possible high repetition rate. Higher target densities

are advantageous for the reachable electron energy and increase, up to a certain limit, the number of accelerated electrons. Therefore, the use of a cluster jet target is very promising because of the very high local density inside of the single clusters although the total density in the cluster jet is well below the density of most gas jets presented in [M<sup>+</sup>13].

The same experimental setup as presented in the last chapter (see section 5.1 and figure 5.1) is used again to detect high energy electrons in laser forward direction. The direction of the magnetic field is reversed for these measurements so that negatively charged particles hit the MCP. The evaluation of the data is done in the same way as presented before for the proton data (see section 5.2) with an additional conversion of the energy. This is necessary because the evaluation routine calculates the energy for a given pixel row under the assumption that the measured particle were non-relativistic protons. Since relativistic electrons are measured instead, a conversion factor has to be taken into account. The relativistic momentum  $p$  corresponding to the calculated energy  $E_{\text{kin}}$  for protons is calculated from the relativistic energy momentum relation

$$(E_{\text{kin}} + mc^2)^2 = m^2c^4 + p^2c^2 \quad (5.4.1)$$

and the detected electrons are assumed to have the same momentum. The relativistic energy momentum relation is used again to calculate the corresponding energy of the detected electrons.

A temperature scan at constant laser parameters of 5 J pulse energy before compression and 30 fs pulse length and at a constant stagnation pressure of 16 bar for the cluster jet was taken. The signal was very small compared to the proton signal seen before. Not all temperature steps showed a significant signal above the background. Figure 5.19 shows the evaluated electron spectra for the temperatures with a significant signal and figure 5.20 shows the corresponding cut-off energies. Only at stagnation condition corresponding to highest effective target densities a significant signal can be observed. The cut-off energies are roughly between 8 and 12 MeV, but without any clear trend. Additional measurements with the same detector shifted to 45 ° or 135 ° with respect

to the laser propagation direction showed no electron signal at all. The weak signal intensity, the acceleration direction and the achieved energies all fit very well with the laser wakefield acceleration scheme.

Since the Thomson parabola is quite far away from the interaction point (around 1.5 m) and the energy resolution is restricted to the lower MeV range, Image plates (Fujifilm's BAS-IP TR 2040) were used to investigate lower energetic electrons close to the interaction point. Image plates are film-like sensors which can store radiation energy. The stored energy can be released by stimulated emission with a laser as luminescence. The used image plates were sensitive to electrons, protons and X-rays. The IPs were wrapped in 14  $\mu\text{m}$  thick aluminium foil to absorb the accelerated protons and a measurement with an added permanent magnet at the back of the image plate showed that the detected particles carried electric charge and thus were no X-rays. The image plates are wrapped around the cluster jet like a cylinder. Figure 5.21 shows the readout of two image plate taken at stagnation conditions of 16 bar and 34 K or 40 K, a laser energy of 5 J before compression and a laser pulse length of 30 fs. Only a single laser shot was recorded per image plate. Next to the strong electron signal in laser forward direction (the dot in the centre) at 34 K, there is a ring link structure in both measurements. The difference between 34 K and 40 K seems to be critical for the acceleration process. Additional measurements with different filters in front of the image plate and with an electron spectrometer consisting of a pinhole, a permanent magnet and an IP determined the energy of the ring electrons to be up to 150 keV. But these measurements need further investigation concerning the measured structure, the electron intensities and the electron energy distribution and will be published in more detail in the next year [A<sup>+</sup>21]. Up to now the ring electrons seem to be electrons with too much transversal momentum to be trapped in the wake escaping from it in a more or less parameter independent angle.

The same structure of laser-wakefield accelerated electrons was already described in former publications by [B<sup>+</sup>19] and [Y<sup>+</sup>17] using a similar laser pulse and a gas jet target. The presented experiments used target densities 2-3 orders of magnitude higher than the cluster jet density used in this work. Particle in a cell (PIC) simulations by [C<sup>+</sup>18] or [M<sup>+</sup>20] show that the trapping mechanism is enhanced by the presence of clusters in the target due to their local high density. This improves the laser wakefield acceleration

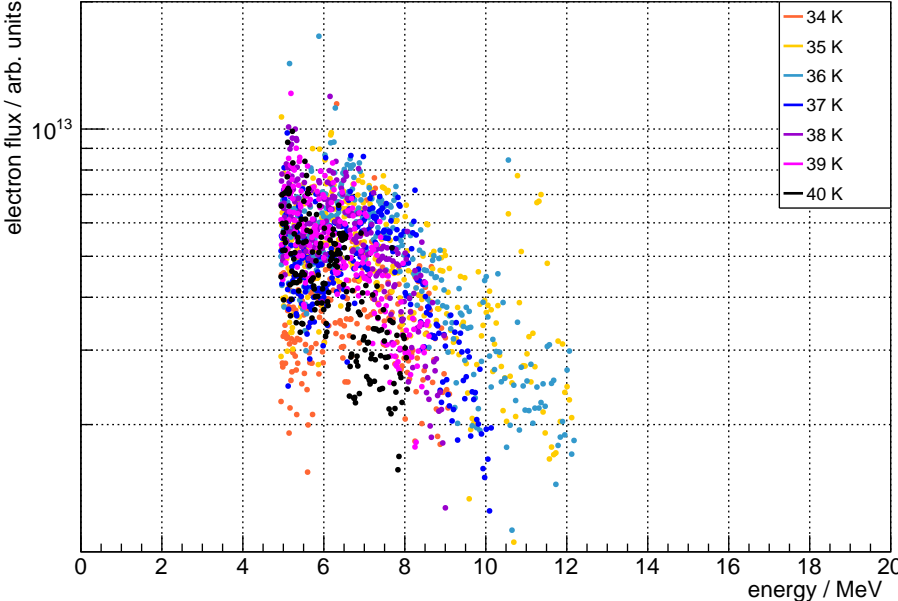


**Figure 5.19** – Electron spectra at different stagnation temperatures of the cluster jet. The scan was taken at a laser pulse energy of 5 J before compression, a laser pulse duration of 30 fs and a stagnation pressure of the cluster jet of 16 bar. Varying the stagnation temperature leads to no significant change of the electron energy spectra.

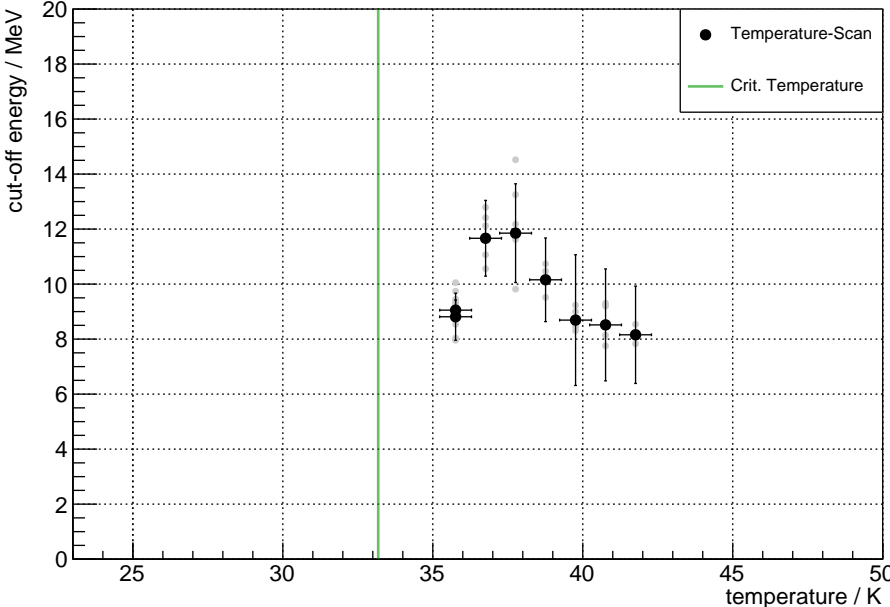


**Figure 5.20** – Electron cut-off energies of the temperature scan. The scan was taken at a laser pulse energy of 5 J before compression, a laser pulse duration of 30 fs and a stagnation pressure of the cluster jet of 16 bar. There is no clear trend visible in the cut-off energies.

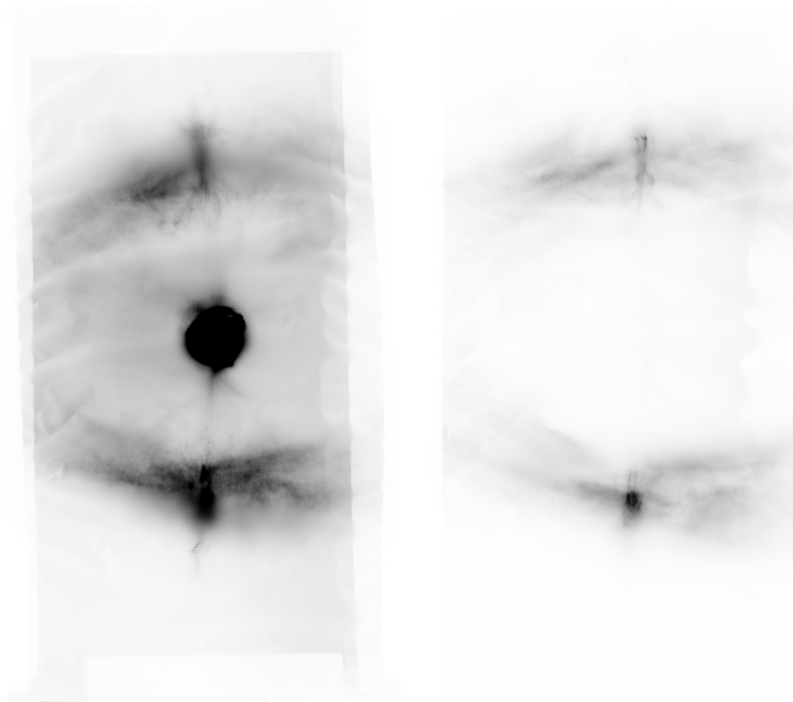


**Figure 5.21** – Readout of two IPs in laser forward direction wrapped around the cluster jet. The bright centre spot is caused by wakefield accelerated electrons while the ring like structure is probably caused by electrons which escaped from the wake without entering the bubble regime. The shown data are taken at stagnation conditions of 16 bar and 34 K (left) or 40 K (right) and from a single laser pulse of 5 J energy before compression and a pulse length of 30 fs.

using a cluster jet target to a comparable level to gas-jet targets of 2-3 orders of magnitude higher density.

## Summary

This chapter presented the data taken of accelerated protons and electrons in the laser cluster interaction and the newly developed evaluation routine, which enables a treatment of systematic uncertainties. A very good shot-to-shot stability of the accelerated protons was shown. It originates from the large interaction volume containing many clusters and the weak dependence on the laser pulse energy. A good agreement of the proton energies in the gaseous cluster regime with the corrected Hagedorn law was shown in various scans and the dependence of the laser pulse energy was investigated to have mostly an effect on the size of the effective interaction volume. The interaction of a short pulse

laser with clusters generated in the liquid cluster regime was investigated for the first time. Unfortunately no interaction with micrometer sized clusters could be observed as expected. However, next to these micrometer sized clusters another distribution of smaller clusters are generated simultaneously. Although most of the clustering gas is bound in the larger clusters, a clear proton signal generated by the Coulomb explosion of the smaller clusters can be observed. The detected proton energies are more or less pressure and temperature independent and reach up to approximately 200 keV, which correspond to cluster diameters of 56 nm. Laser wakefield accelerated electrons with energies around 10 MeV have been measured at low fluxes in laser forward direction. Additionally, a ring structure of accelerated electrons of lesser energy (approximately up to 150 keV) but higher flux was recorded closer to the interaction point. An increase of the electron capture efficiency caused by the presence of the locally very dense clusters was observed.





## 6 X-rays generated by laser-cluster interaction

The generation of ultra-short X-ray pulses has received a growing interest in the past decades. Several applications in biology, physics and industry require X-ray pulses e.g. for the investigation of condensed matter or ultra fast processes in the ps to fs scale or as pumps for short wavelength lasers. The few existing XFEL facilities are already able to generate the required X-ray pulses, but the access to these very large facilities (km scale) is very limited. The interaction of an ultra-short laser pulse with a plasma offers a promising small scale alternative. The three generation mechanisms of collimated X-ray pulses in laser plasma interaction are betatron radiation of the heated electrons, higher harmonics generation and Thomson scattering. The last two usually suffer of a low yield [C<sup>+</sup>13] leaving only betatron radiation as a suitable X-ray generation mechanism. Since gas jet targets are suitable for laser wakefield acceleration of electrons which in turn generate the betatron radiation, these targets are very popular in the investigation of generated X-ray pulses. But gas jets come with a small drawback as higher target densities increase the number of accelerated electrons but decrease their energy simultaneously [C<sup>+</sup>13]. A cluster jet target may overcome this since the electron trapping mechanism is enhanced due to the local high density regions of the single clusters, while the total target density is comparably low as presented in the last chapter.

Various measurements of X-rays generated in laser-cluster interaction were taken. This chapter introduces the experimental setup and the detectors used before the evaluation method is described and the data taken is presented.

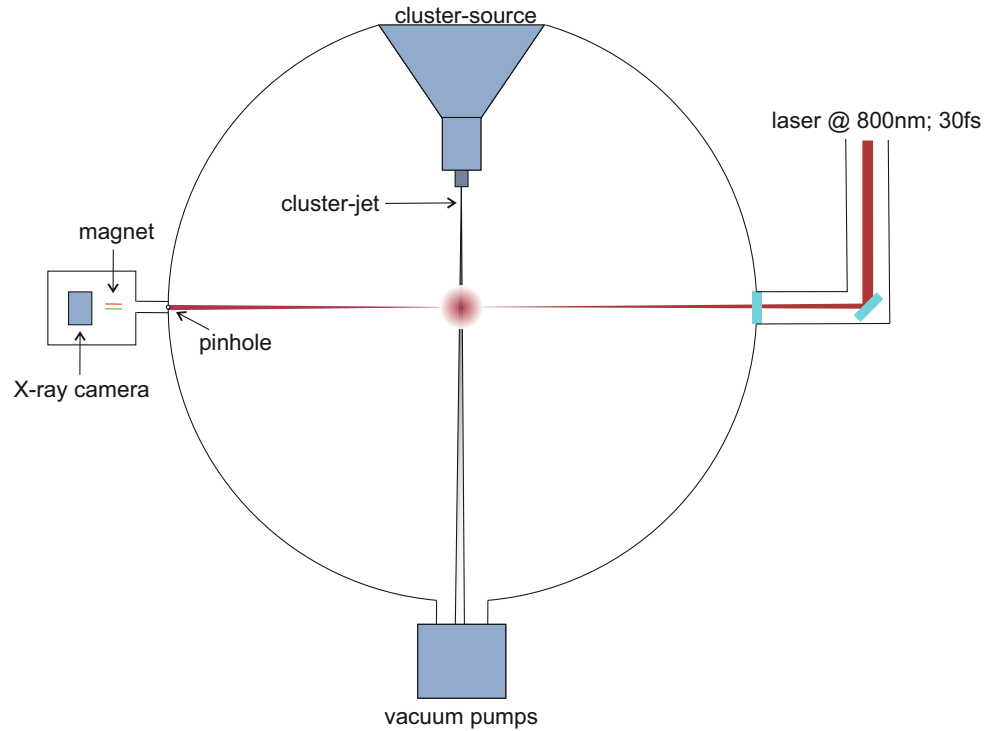


**Figure 6.1** – A sketch of the experimental setup used to detect X-rays. The cluster jet propagates through the interaction vacuum chamber ( $p \approx 0.1$  mbar) and is dumped into the pumping system. The ARCTURUS laser pulse interacts with the cluster jet in the centre of the vacuum chamber and the generated X-ray radiation can be detected with an Andor X-ray camera under  $0^\circ$  with respect to the laser propagation direction. Based on an image generated by C. Mannweiler.

## 6.1 Experimental setup

The experimental setup for measurements on generated X-ray radiation in the laser cluster interaction consists of the cluster jet target MCT-D (c.f. chapter 3.2), the ARCTURUS laser beam (c.f. chapter 4) perpendicular to the cluster jet and an X-ray camera in forward direction of the laser. A sketch of the setup used can be seen in figure 6.1. A small solid angle of the generated X-ray radiation is selected by a pinhole and enters the detector chamber together with the accelerated charged particles discussed in the last chapter. A magnet (0.18 T) deflects the charged particles as they would generate bremsstrahlung in the following filter layers. An aluminium filter holder with five holes for different filters is mounted in front of the camera. The holder itself has a thickness of approximately 1 cm and absorbs all incoming X-rays with energies in the detection

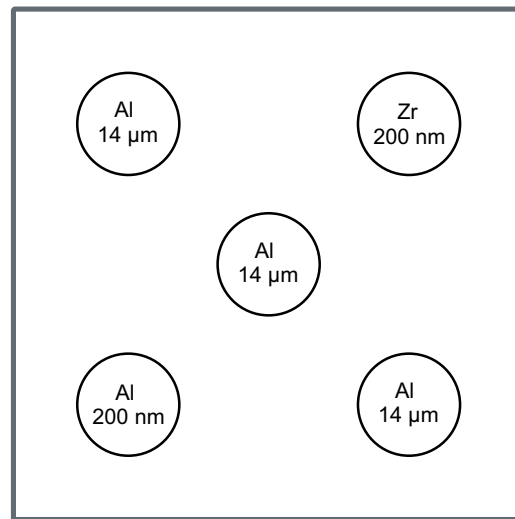


**Figure 6.2** – A sketch of the filter arrangement used directly in front of the X-ray camera. The holder features five holes for filters, three of which are covered by 14  $\mu\text{m}$  aluminium foil (top left, centre, bottom right), the other two area either covered with a 200 nm aluminium foil (bottom left) or by a 200 nm zirconium foil (top right).

range of the X-ray camera. The holder features five holes for thinner filters. Figure 6.2 shows a sketch of the filter holder and the used filter arrangement. Three of the holes were covered with a 14  $\mu\text{m}$  aluminium foil (top left, centre, bottom right), one was covered with a 200 nm aluminium foil (bottom left) and one was covered with a 200 nm zirconium foil (top right). The different filters protect the camera by blocking the direct laser light and they are permeable for different amounts of the incoming X-rays, allowing an estimation of their energy. The X-ray CCD (charge-coupled device) camera (Andor DX436-BN) used is sensitive for photons between 10 eV and 10 keV and is placed 1.3 m from the interaction point. Figure 6.3 shows the quantum efficiency of the X-ray camera and the transmission factors of the different filters and of the interaction chamber. For the transmission factor of the interaction chamber a filling with hydrogen gas at a pressure of  $10^{-1}$  mbar and a transmission distance of 80 cm is assumed. This corresponds to the distance between interaction point and pinhole to the detector chamber. The transmission through the detector chamber is neglected since the vacuum in the detector chamber is several orders of magnitude better than in the interaction chamber. Since there is, as shown later, only an observed signal behind the two thinner filters and no signal behind the thicker filters, the energy range of the generated X-ray radiation can be estimated to be below a few keV and above approximately 50 eV.

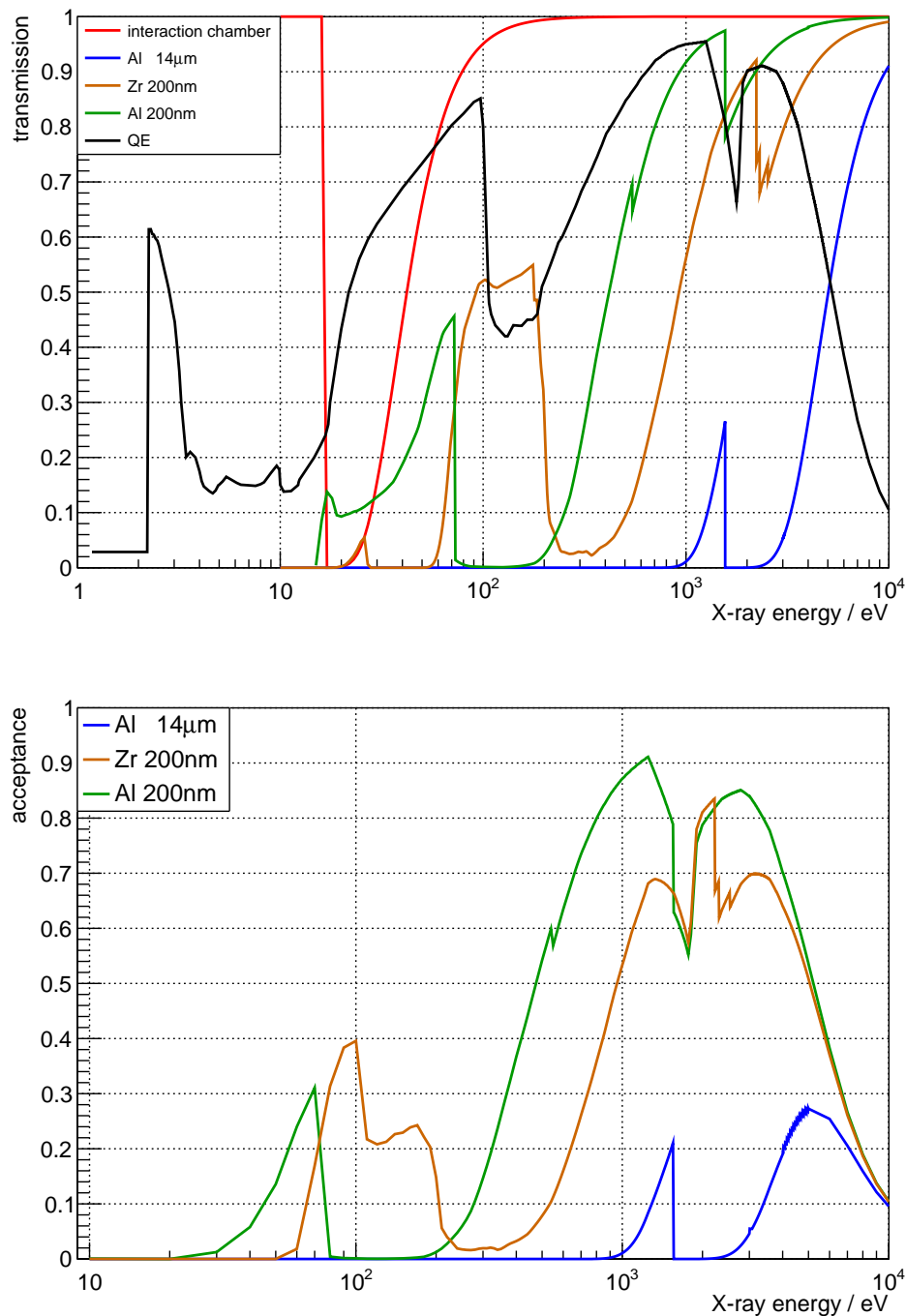


**Figure 6.3** – The top shows the quantum efficiency (QE) of the X-ray camera used [Ins20] and the transmission coefficients of the different filters and of the vacuum between interaction point and detector chamber [HGD93]. 80 cm of hydrogen gas at a pressure of  $10^{-1}$  mbar is used for the transmission factor of the interaction chamber. The bottom shows three products of the quantum efficiency with the transmission coefficient of the vacuum chamber and the three different filters. These are the detection likelihoods or the detector acceptances for the three different filters.

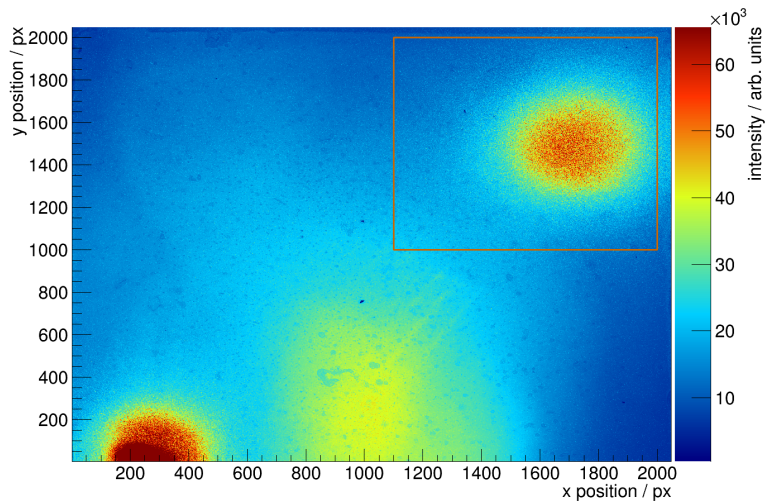


**Figure 6.4** – Example image taken with the X-ray camera at stagnation conditions of the cluster jet of 16 bar and 25 K and at 4.2 J laser pulse energy and 30 fs laser pulse duration. The orange rectangle marks the signal region behind the 200 nm zirconium filter.

## 6.2 Evaluation method

The images taken with the X-ray camera are evaluated in a region of interest corresponding to the 200 nm zirconium filter. Figure 6.4 shows an example image with the evaluation region marked with an orange box. The evaluation region leaves a small gap to the right side because of several broken pixels close to the border. The 200 nm aluminium filter on the bottom left side had a small hole resulting in an area where direct laser light overexposes the camera. Since the signal behind the 200 nm aluminium filter can not be distinguished from the light leak it is excluded from the evaluation. There is another light leak in the bottom centre of the images where scattered laser light is detected.

For highest laser intensities and target densities some pixels in the evaluation region are overexposed. Since this would cause an error in the following evaluation, these pixels are extrapolated firstly. Therefore, the centre of the signal is determined using projections of the whole signal region on both axes and finding the best fit of a Gaussian

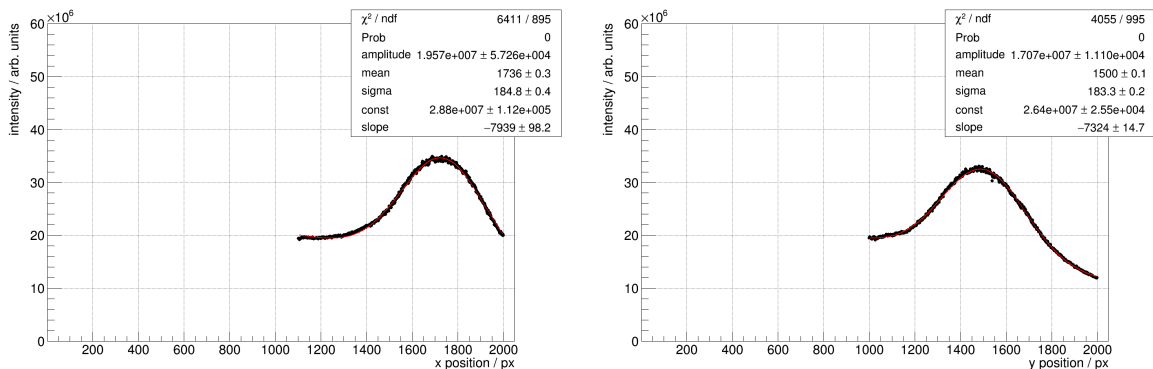


**Figure 6.5** – The two projections of the whole evaluation region of the example shot shown in figure 6.4 on both axis. The best fit of Gaussian functions combined with linear background functions are shown in red. The mean position is taken as the center of the signal.

function. The mean values of the best fits are used as the centre of the signal. The two projections and the corresponding best fits of an exemplary data image are shown in figure 6.5. Since all data images share the same signal position, this procedure is done for all data images and the mean position of the centre of the signal  $\bar{x}_{\text{centre}} = 1727(11)$  px and  $\bar{y}_{\text{centre}} = 1496(16)$  px is used for all images. Afterwards, concentric circles are found around the central spot with the fixed number of 10000 pixel in between neighbouring circles. The intensity values of all pixel between two neighbouring concentric circles are filled into a histogram as shown in figure 6.6. Keeping the distances between the circles as low as chosen results in very few counts per intensity value. Combining 100 neighbouring intensity values increases the counts per bin to an more manageable number as already shown in figure 6.6. The filled intensity values should be normal distributed around a mean intensity allowing an extrapolation of the overexposed pixel. For this extrapolation the overexposed pixel are removed from the histogram and the best fit of an asymmetric Gaussian function to the remaining histogram is found. The asymmetric function is chosen because of the linear background below the data which will be removed later during the evaluation. A new random value following the distribution found is assigned to every overexposed pixel. All new values are above the former overexposure threshold. These new values are shown in figure 6.6 in red and they are used during the following evaluation. The whole procedure starts in the centre of the signal and is repeated for the next more outer concentric circle until all overexposed pixel are corrected. This extrapolation technique was developed by A. Khoukaz [Kho21].

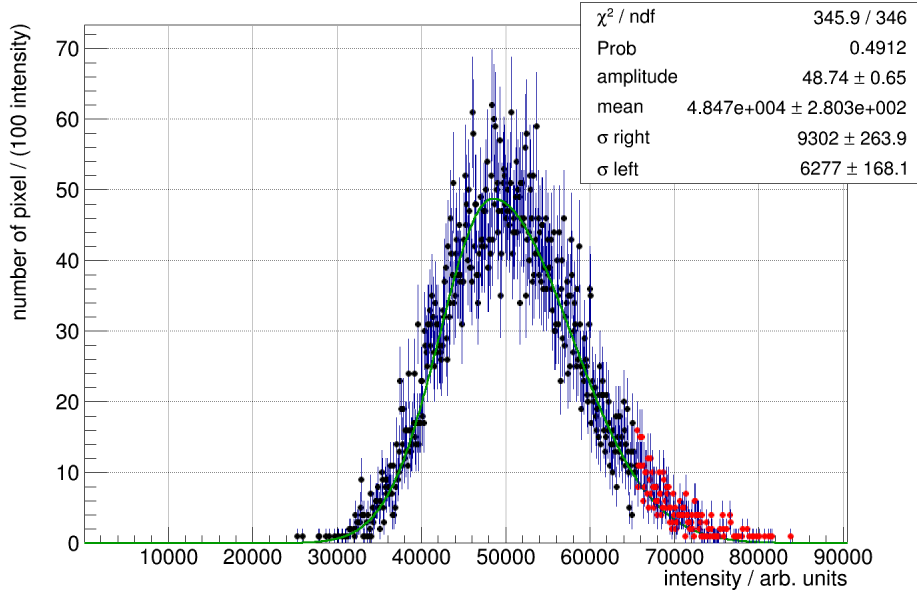


**Figure 6.6** – Intensity values of the pixel between the third and fourth concentric circles. The best fit of an asymmetric Gaussian function is shown as a red line. The overexposed pixel were already removed from the histogram and added again in red using random values following the distribution found.

After the extrapolation of all overexposed pixel in the signal area, the measured intensity in the marked box is projected column by column on the vertical axis. Figure 6.7 shows an example projection. The best fit of a Gauss function combined with a linear background function is found for each projection and is shown in red while the background part of the fit is shown in orange. The significance of the signal fit compared to a linear background function is calculated. For significances above  $3\sigma$  the intensity values of the whole projection are counted while subtracting the background part found by the best fit. The sum of these values is used as the evaluated X-ray intensity.

## Uncertainties

Several uncertainties have to be taken into account during the evaluation of the X-ray data. The statistical uncertainty is the square root of the number of incoming photons

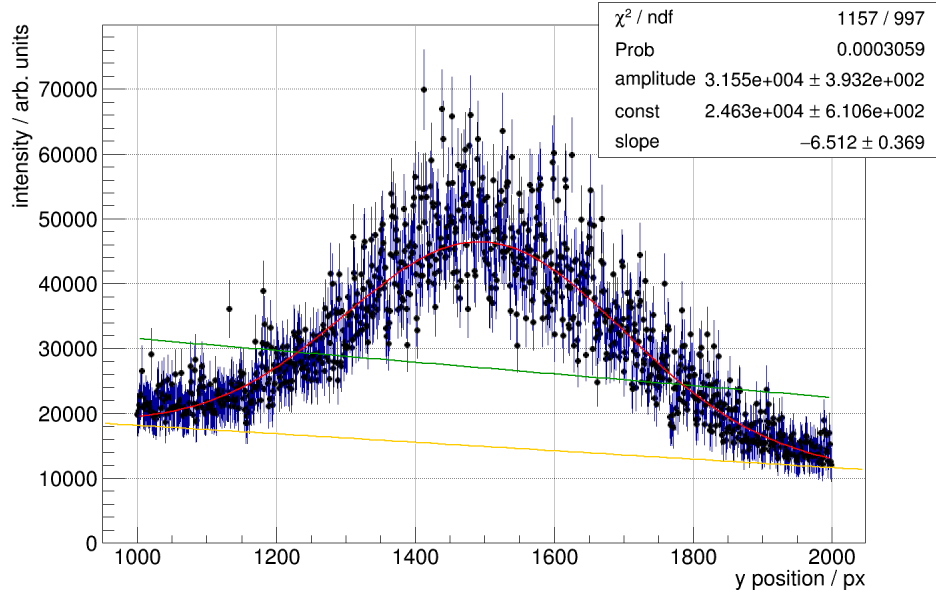


**Figure 6.7** – Example projection of pixel column 1600 of the marked signal region (c.f. figure 6.4) on the vertical axis. The best fit of a Gauss function (signal) and a first order polynomial (background) is shown in red. The background part of the fit is shown in orange and the background only hypothesis for the significance calculation is shown in green.

$\sigma_{\text{stat}} = \sqrt{N_\gamma}$ . Since every incoming photon generates multiple electrons during the absorption process in the camera, the resulting intensity uncertainty is the square root of the product of the conversion factor  $k(E) > 1$  between incoming photons and photoelectrons and the number of counted photoelectrons  $dN_e = \sqrt{kN_e}$ . The manufacturer of the X-ray camera provides an energy dependent relation between incoming photon energy and number of generated photoelectrons, as shown in figure 6.8 [Ins20]. Since the transmission of the 14  $\mu\text{m}$  aluminium foil increases at a few keV to a value which is significantly above zero (e.g.  $T_{\text{Al}}(3\text{keV}) = 0.05$ ) and there is no signal measured behind these filters, the X-ray energy is certainly below a few keV. For the treatment of the statistical uncertainties an X-ray energy of 3 keV is assumed as the exact energy distribution is not known. This value is chosen because the X-ray energy is certainly below this energy and the conversion factor is directly proportional to the X-ray energy. Thus, the conversion factor is certainly overestimated resulting in an overestimation of the relative statistical uncertainty. Next to the statistical uncertainties there are uncertainties of the fit parameters, which are included during the background reduction.



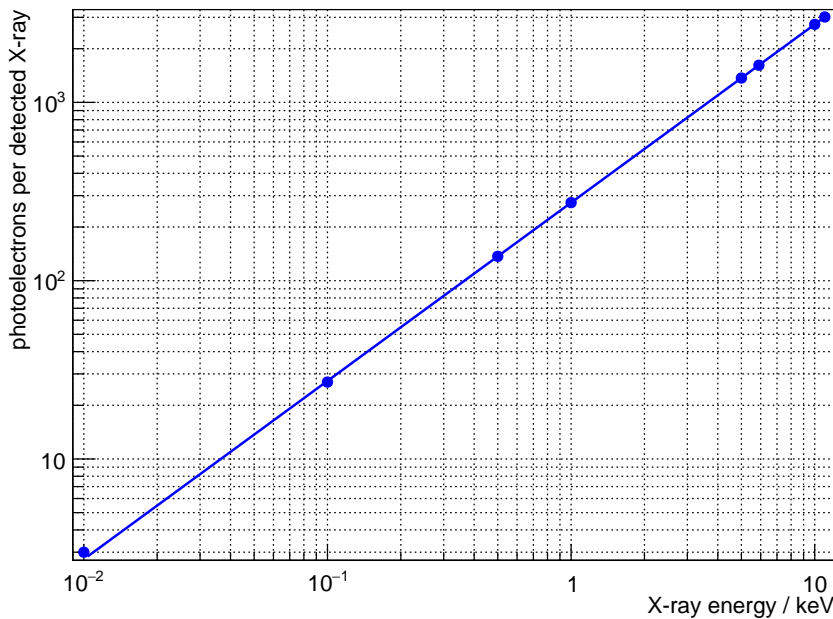


**Figure 6.8** – Number of photoelectrons per detected X-ray in dependence of the X-ray energy, data taken from [Ins20].

Additional uncertainties may occur during the reconstruction process. The centre of the signal is found for the reconstruction technique and used to group up pixel with the same intensity value. The centre spot has been shifted by up to 50 pixel in all directions, which corresponds to about three times the standard deviation, resulting in a change of the evaluated X-ray intensity of below 0.1%. In addition, the mean values and the widths of the reconstruction functions (asymmetric Gaussian functions) were varied by up to three times their fit uncertainties in both directions. Again, this resulted in a change of the evaluated X-ray intensity of below 0.1%. The additional systematic uncertainties generated by the reconstruction technique are neglected because they are very small compared to the uncertainties caused by the evaluation process presented in the next paragraph.

During the evaluation additional systematic uncertainties occur, because the evaluation region as shown in figure 6.4 was chosen arbitrarily. The left border of the evaluation

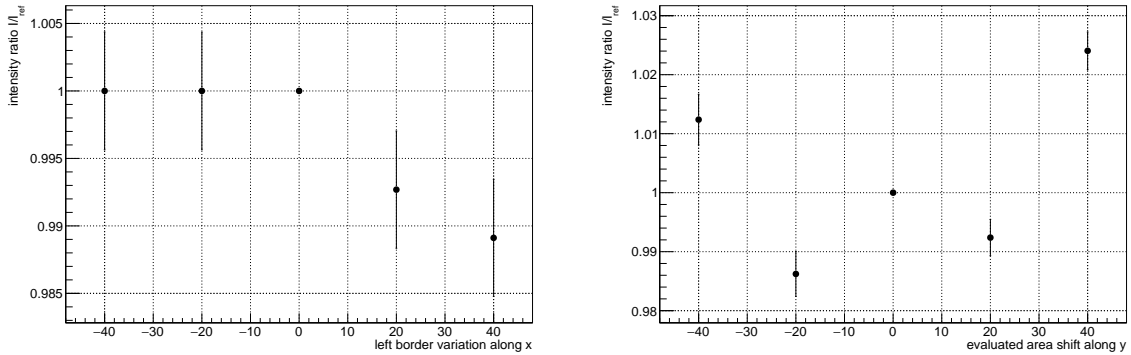


**Figure 6.9** – Example ratio plots for the determination of systematic uncertainties caused by the arbitrary choice of the evaluation region. The effect of the variation of the evaluation region along the horizontal axis is shown on the top and the effect of a shift of the evaluation region along the vertical axis is shown on the bottom. The shown example corresponds to stagnation conditions of 16 bar and 25 K, a laser pulse energy of 4.1 J and a laser pulse length of 30 fs.

region was varied slightly and the whole evaluation region was shifted slightly along the vertical axis while leaving the box size constant. Both variations were done for 20 pixel and for 40 pixel in both directions. The ratios of the nominal value to the values evaluated with the varied evaluation regions are shown for an example shot in figure 6.9. For the variation along the vertical axis, a decrease of the evaluated X-ray intensity can be seen for shifts towards the signal but no increase of the X-ray intensity can be observed for shifts away from the signal. Thus, the whole signal is included at the nominal position of the left border of the evaluation region. Increasing the evaluation region does not increase the obtained signal due to the significance check of each pixel row. The shift of the evaluation region along the horizontal axis results in no clear trend. The weighted standard deviation of the ratios is used as an additional systematic uncertainty. Figure 6.10 shows the calculated systematic uncertainties for all shots.

### 6.3 X-ray detection

Several series of measurements were taken similarly to the scans of the accelerated protons presented in the last chapter. The data was evaluated as presented before in this chapter taking all discussed uncertainties into account. Two scans of the stability of the X-ray

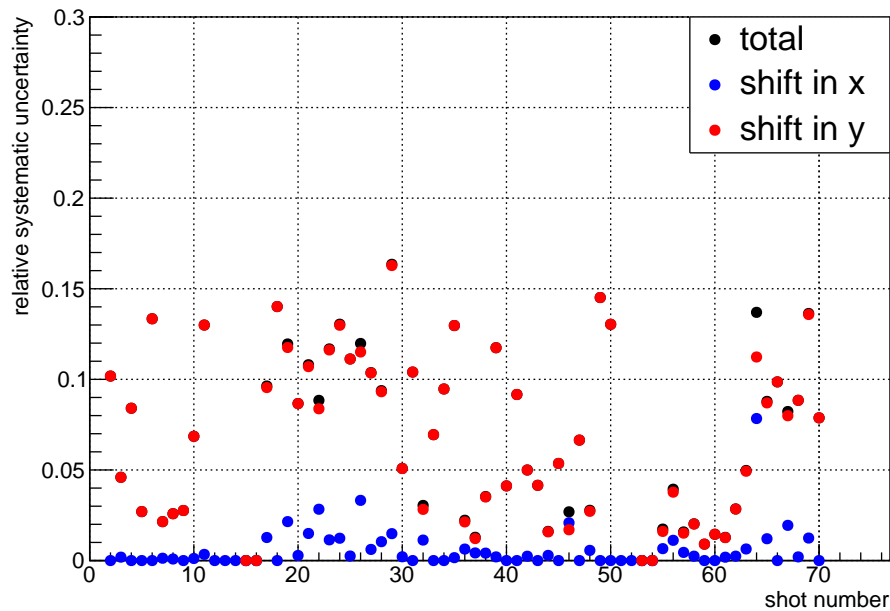


**Figure 6.10** – Systematic uncertainties for all shots taken. The systematic uncertainties caused by a variation of the evaluation region along the horizontal axis are shown in blue and the systematic uncertainties caused by a shift of the evaluation region along the vertical axis are shown in red. The combined uncertainties are shown in black, but for several shots the black dots are hidden behind the corresponding red dots.

signal, a temperature scan, two pressure scans and two laser pulse energy scans are presented in this section.

### Stability measurements

Two stability measurement series were taken. During these scans all laser and target parameters were kept constant and five shots were taken consecutively. The first scan was taken at 16 bar backing pressure, 25 K stagnation temperature (liquid regime), 30 fs laser pulse duration and a laser pulse energy of 4.1 J. The second scan was taken at 16 bar backing pressure, 34 K stagnation temperature (hypercritical regime), 30 fs laser pulse duration and a laser pulse energy of 4.6 J. Figure 6.11 shows the evaluated X-ray

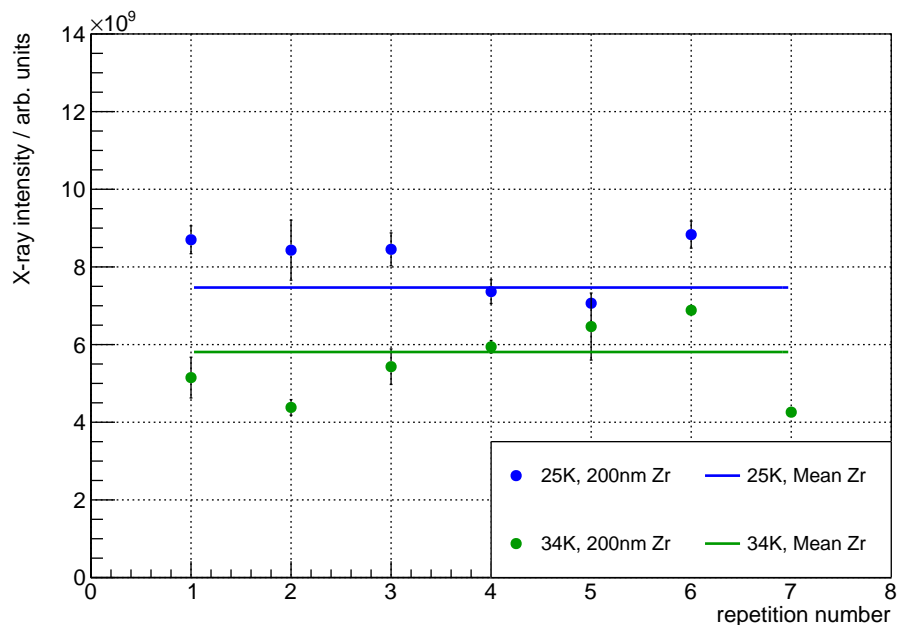


**Figure 6.11** – X-ray intensity values for the two stability scans. The shot numbers are correct for the 34 K scan, while the shot numbers of the 25 K scan were shifted by 38 for comparison. The lines show the weighted mean values as listed in table 6.1.

intensities measured for both scans. Two additional shots taken during the temperature scan at the same conditions are added to the series, respectively. Table 6.1 shows the weighted mean values and weighted standard deviations as a measure for the stability. The relative standard deviations are 9% and 21% and thus higher than the calculated uncertainties. There are more uncertainties not taken into account yet, e.g. fluctuations in the laser pulse energy or in the local target density. To include these effects, the highest relative standard deviation of the stability scans is added as an additional uncertainty for all following scans. A lower limit of the number of detected X-rays per shot is estimated later in this chapter using the results of the following scans of the target parameters.

**Table 6.1** – Weighted mean values and standard deviations ( $\sigma$ ) of the X-ray intensities of the two stability scans.

scan parameters	mean X-ray intensity / arb. units	relative $\sigma$
200 nm zirconium filter		
16 bar, 25 K, 30 fs, 4.2 J	$7.5(7) \times 10^9$	9%
16 bar, 34 K, 30 fs, 4.6 J	$5.8(1.2) \times 10^9$	21%

### Temperature scan

In addition to the two stability scans a temperature scan was taken. The laser was operated at constant parameters of 30 fs pulse length and 4.2 J pulse energy before compression. The stagnation conditions of the cluster jet were 16 bar backing pressure and the temperature was varied. Two shots were taken at each temperature setting and in steps of 3 K between 25 K and 46 K. Figure 6.12 shows the evaluated X-ray intensities of the temperature scan with the two stability scans added. The evaluated X-ray signal is higher for stagnation conditions in the liquid regime or for temperatures below the critical temperature, but a clear trend can neither be seen in the liquid nor in the gaseous regime within the given statistics. A more detailed interpretation of the temperature scan follows in the next paragraph in combination with the pressure scans taken.

### Pressure scans

Two pressure scans at stagnation temperatures of 25 K and 34 K and with laser pulse durations of 30 fs and a laser pulse energy of 4.1 J before compression were taken. Two shots were taken per pressure setting in steps of 2 bar in both scans. Figure 6.13 shows the evaluated X-ray intensities of the two pressure scans. While the scan taken at 34 K shows constant X-ray intensities for lower pressures and an increase of the X-ray intensity for higher pressures, the scan taken at 25 K shows this behaviour for the whole scan.

For an interpretation of the measurements presented so far, two additional plots were generated. Thereby, a possible dependency of the X-ray intensity measured on the cluster sizes or on the cluster jet density is investigated. Figure 6.14 shows all measurements at laser pulse energies between 4.1 J and 4.6 J before compression plotted against the respective calculated cluster jet density. In addition a background measurement with nearly no target density, taken at stagnation conditions of 34 K and 1.1 bar, is included. The cluster jet density was calculated using formula 3.1.17 and the measured values for temperature and volume flow at each single measurement. In addition, the residual gas density is calculated from the interaction chamber pressure and added to the target density to address the change of the residual gas density during the measurements. A dependency of the X-ray intensity on the target density is expected as the number of

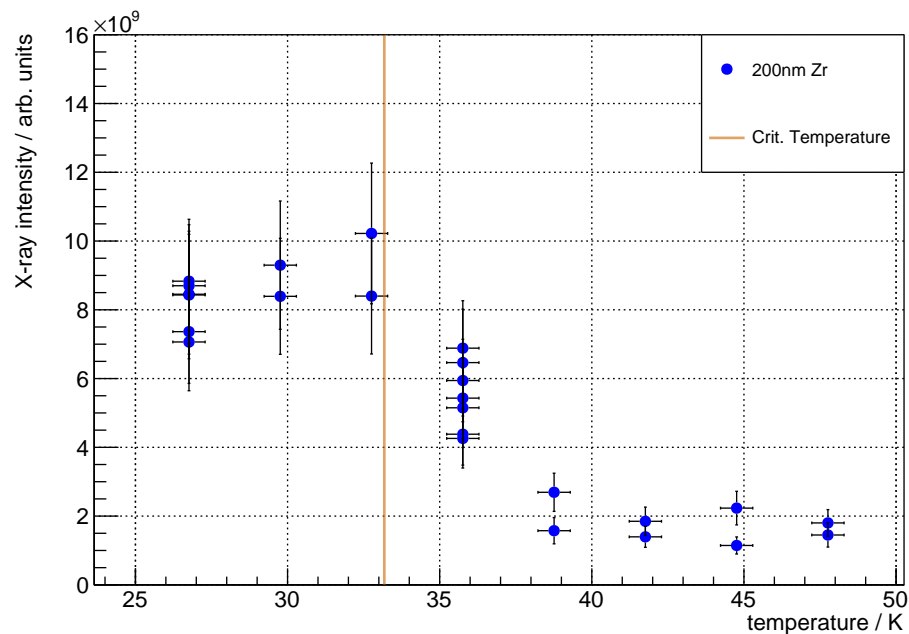


**Figure 6.12** – X-ray intensity values of the temperature scan and the two stability scans. All measurements were taken at a stagnation pressure of 16 bar and at laser pulse energies between 4.1 J to 4.6 J. The X-ray yield is higher in the liquid regime than in the gaseous regime.

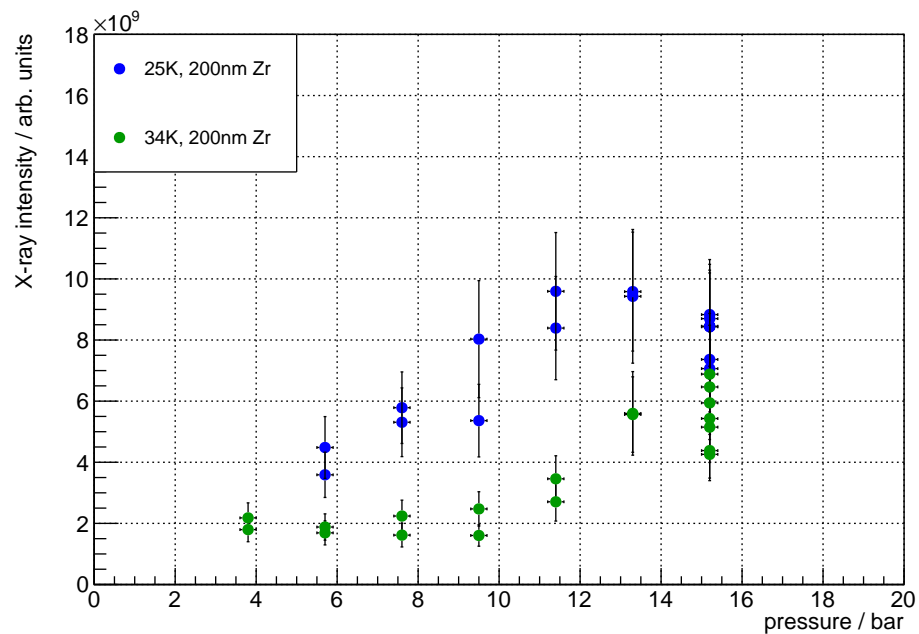


**Figure 6.13** – X-ray intensity values of the two pressure scans and the two stability scans. All measurements were taken at laser pulse energies between 4.1 J to 4.6 J. While the scan taken at 34 K shows constant X-ray intensities for lower pressures and an increase of the X-ray intensity for higher pressures, the scan taken at 25 K shows this behaviour for the whole scan.

generated X-rays by betatron radiation is the product of the number of free electrons and the number of oscillations each electrons undergoes emitting X-ray radiation. Since the laser intensity is high enough to ionise all target atoms, the number of free electrons corresponds directly to the target density. This results in combination with the oscillation frequency of the electrons (see formula 2.4.1) in

$$I_{X\text{-ray}} \propto n_e \cdot \omega_b = \frac{n_e \omega_P}{\sqrt{2\gamma}} = n_e \sqrt{\frac{n_e e^2}{\epsilon_0 m_e 2\gamma}} \quad (6.3.1)$$

$$\propto n_e^{3/2} \quad (6.3.2)$$

using the plasma frequency  $\omega_P = \sqrt{\frac{n_e e^2}{\epsilon_0 m_e}}$ . The data is fitted with  $I_{X\text{-ray}} = a + b n_e^{3/2}$  with the proportionality constant  $b$  and an offset parameter  $a$ . The function fits very well to the data confirming the density dependency of  $I_{X\text{-ray}} \propto n_e^{3/2}$ .

A certain X-ray intensity is measured even without any target density resulting in a offset parameter larger than zero as shown by the fit. This observed offset may depend on the laser parameters, which were kept constant during the presented measurements, but it originates not from the laser target interaction. Therefore, the offset has to be constant during the presented measurements. An afterglow of the camera used can be excluded since the measurements were not taken from highest to lowest target density. An interaction of the laser pulse with the residual gas in the interaction chamber is already included in the calculated target densities and the interaction of the laser pulse with water, oxygen or nitrogen leaked into the interaction chamber is unlikely. The dependency between interaction chamber pressure and target gas flow as shown in figure 6.15 shows that the leakage rates are negligible small. The interaction chamber vacuum reaches the middle  $10^{-3}$  mbar range at low gas flows. This fits very well to the used pump (Leybold RUVAC WH 7000 with a nominal pumping speed of 7800 m<sup>3</sup>/h) with the big vacuum chamber with several big flanges with big O-ring seals and relative short pumping periods of maximum a few hours resulting in water vapour remaining in the vacuum chamber. Potentially, the laser interacts with other components of the experimental setup as the focusing off axis parabola, the pinhole to the detector chamber, the magnet in the detector chamber or the zirconium filter foil in front of the camera. X-ray radiation

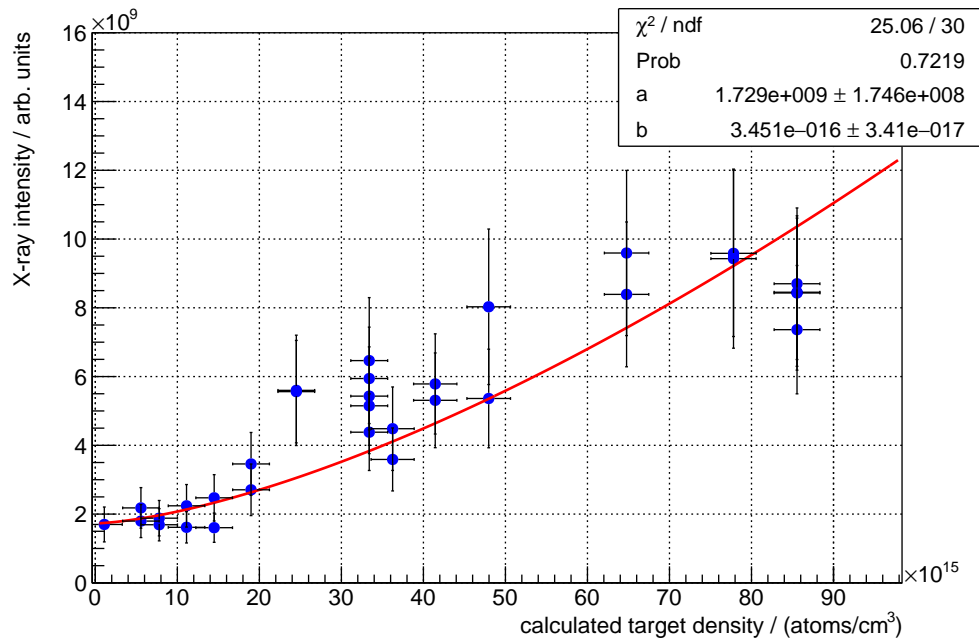


**Figure 6.14** – X-ray intensity values of the of all scans taken at laser pulse energies between 4.1 J and 4.6 J before compression plotted against the respective calculated target density using formula 3.1.17. According to formula 6.3.2 the fit functions is  $I_{X\text{-ray}} = a + b n_e^{3/2}$ .

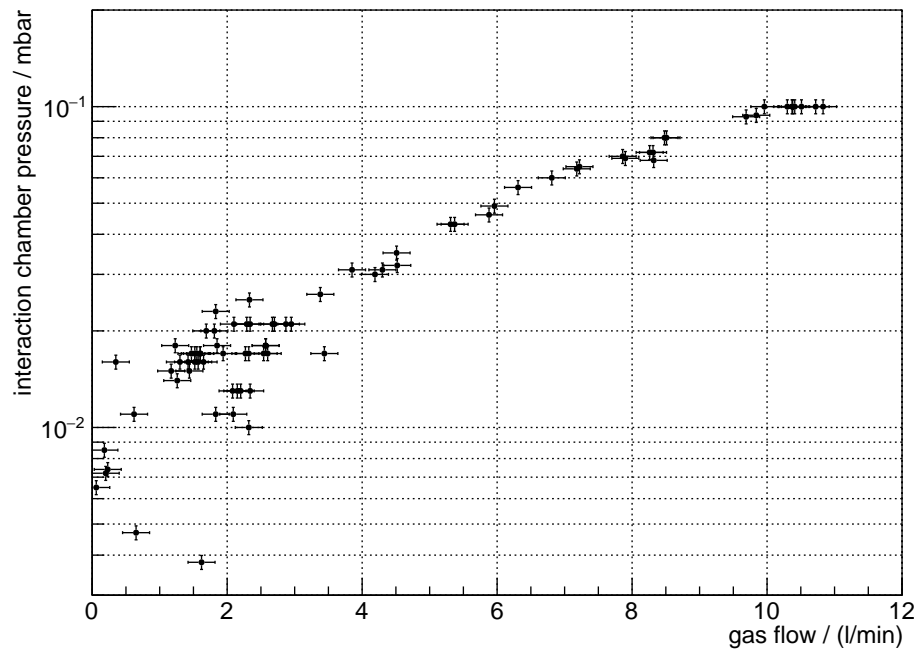


**Figure 6.15** – Interaction chamber vacuum in dependency of the target gas flow. The step trend indicates very low leakage rates.



generated in this interaction or electrons generated in the interaction with the filter may be detected by the X-ray camera. But the laser intensity is comparable low at the positions of these components resulting in the expectation of a very weak interaction. Another possibility for the observe offset is the detection of direct laser photons. The transmission of a 200 nm strong zirconium foil for photons with a wavelength of 810 nm (central wavelength of the laser system used) is according to [J<sup>+</sup>04] in the order of  $10^{-6}$  resulting in an expected offset in the X-ray intensity caused by the detection of direct laser photons in the order of  $10^7$ . However, the filter foil used was already used and stored for several years and thus may be slightly damaged (micro fissures) increasing the transmission for direct laser photons.

Figure 6.16 shows all measurements presented so far and at stagnation conditions in the gaseous regime plotted against the respective calculated mean cluster diameter. The calculation uses formula 3.1.20 and 3.1.22 (c.f. chapter 3.1) including the corrected factor  $A_N = 25(5)$  (c.f. chapter 3.4). Since a clear dependency of the X-ray intensity on the target density was already confirmed, the X-ray intensities measured are reduced by the offset parameter  $a$  and divided by the density dependency  $bn_e^{3/2}$  using the fit parameters as shown in figure 6.14. No clear trend of the X-ray intensity with the cluster diameter can be seen. The high data point at low cluster diameters results from a very low corresponding X-ray intensity divided by a very low density dependency value.

Using the presented target independent offset and the mean X-ray intensity values obtained from the stability scans, a lower limit of the number of detected X-rays per shot can be estimated. Therefore, an X-ray energy of 3 keV is assumed once again, similar to the handling of the statistical uncertainties. This determines the detection efficiency (see figure 6.3) and the number of photoelectrons per incoming X-ray (see figure 6.8) in the most conservative way, resulting in a lower limit. The evaluated mean X-ray intensity of  $7.5(7) \times 10^9$  reduced by the offset  $1.7(2) \times 10^9$  results in  $0.7(1) \times 10^7$  photons per shot. The zirconium filter covers a solid angle of  $0.5 \mu\text{sr}$  or an opening angle of 4 mrad.

As a comparison, [T<sup>+</sup>10] used a gas jet target with densities up to  $3 \times 10^{19} \text{ cm}^{-3}$  and a 10 TW laser system to accelerate electron up to 80 MeV and measured X-ray pulses with  $10^8$  photons per shot at energies between 1 keV and 10 keV. [C<sup>+</sup>13] used a 3.75 TW laser system and an argon cluster jet target with densities up to  $2 \times 10^{19} \text{ cm}^{-3}$  and

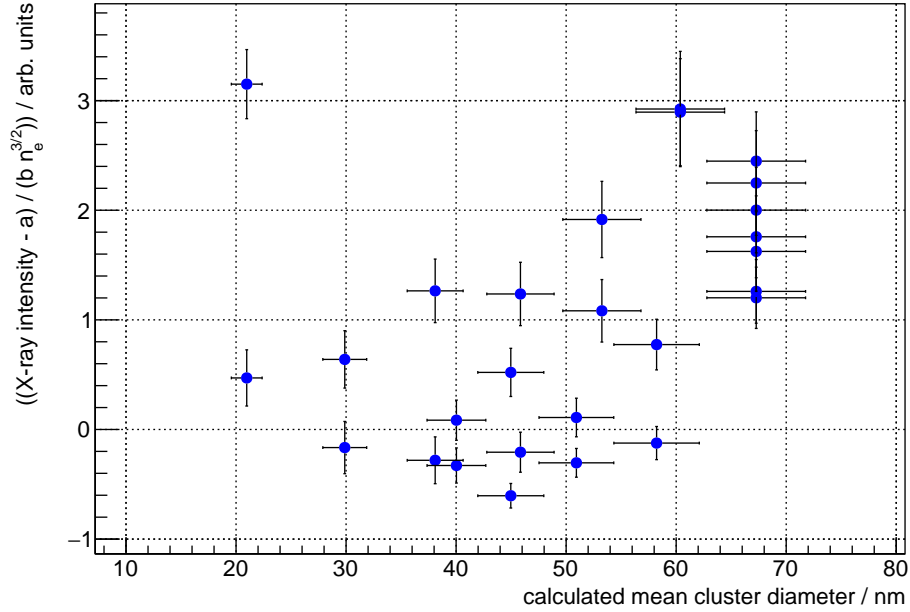


**Figure 6.16** – X-ray intensity values of the of all scans taken at laser pulse energies between 4.1 J and 4.6 J before compression and at stagnation conditions in the gaseous regime plotted against the respective calculated mean cluster diameter using the corrected Hagena scaling law (formula 3.1.22). The X-ray intensity is reduced by the offset parameter  $a$  and divided by the target density dependency relation  $b n_e^{3/2}$  using the fit parameters as shown in figure 6.14. No clear trend of the X-ray intensity with the cluster diameter can be seen.

cluster diameters of approximately 8 nm and received  $2 \times 10^8$  photons per shot with energies above 2.4 keV and within a 10 mrad divergence. After all, the estimated lower limit of this work of  $0.7(1) \times 10^7$  photons per shot is not far below other approaches, as long as the solid angle of the detectors is taken into account. However, the X-ray energy is comparatively low. This suggest the interpretation that the detected X-rays were generated by the lower energetic electrons (c.f. chapter 5.4) which were not trapped and accelerated in the laser wakefield. Since only a small fraction of these lower energetic electrons are accelerated in laser forward direction and most of them are part of the observed ring structure (c.f. figure 5.21), a strong increase of the generated X-ray flow can be expected for the examination of larger solid angle.

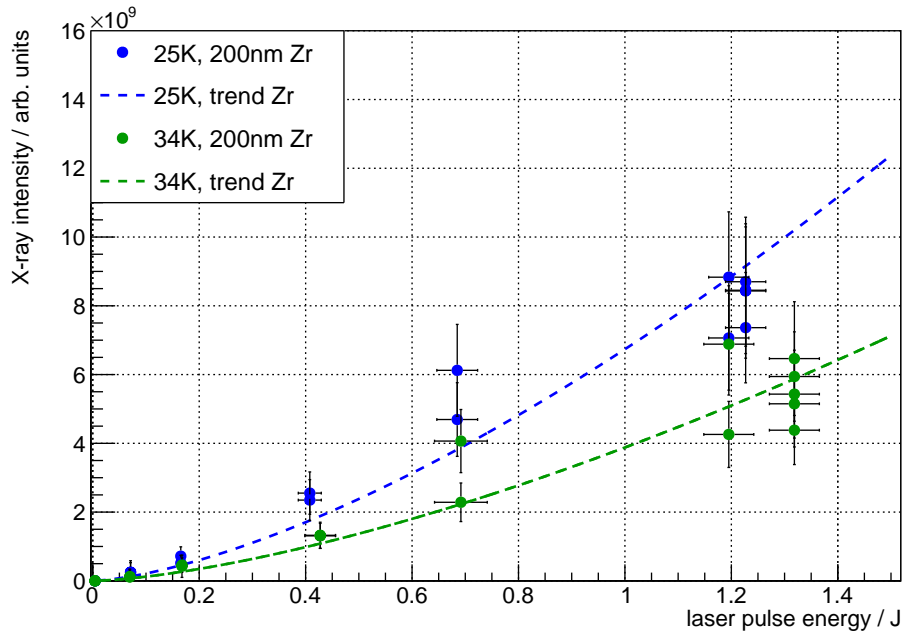


**Figure 6.17** – X-ray intensity values of the two laser energy scans and the two stability scans. The stagnation conditions of the cluster jet were kept constant at 16 bar and 25 K in the first laser energy scan and at 16 bar and 34 K in the second scan.

### Laser pulse energy scans

Two scans of the X-ray intensity at variations of the laser pulse energy were recorded. The laser pulse length was kept at 30 fs in both scans and the stagnation conditions of the cluster jet were kept constant at 16 bar and 25 K in the first scan and at 16 bar and 34 K in the second scan. Figure 6.17 shows the evaluated X-ray intensities of the two laser energy scans. Since a laser intensity of  $1.4 \times 10^{14} \text{ Wcm}^{-2}$  is already sufficient to ionise hydrogen by tunneling ionisation [Gib05], the interaction takes place at a larger volume than the focus volume. This effective interaction volume with a laser intensity beyond the ionisation limit can be calculated for every laser pulse energy by assuming a Gaussian shape of the laser pulse, a constant integral of this profile function during the propagation and a laser opening angle defined by the focusing f/2 OAP ( $\approx 35^\circ$ ). A fit of the calculated effective interaction volume ( $\propto E_L^{3/2}$ ) to the X-ray intensities measured using only a scaling factor shows their direct relation. Table 6.2 shows the fit parameters of the two scaling fits. [D<sup>+</sup>97] found the same proportionality by irradiating krypton clusters of  $5 \times 10^4$  to  $7 \times 10^5$  atoms per cluster with laser beam intensities between

$3.7 \times 10^{16} \text{ Wcm}^{-2}$  and  $5.2 \times 10^{17} \text{ Wcm}^{-2}$  and [R<sup>+</sup>01] showed the same effect at Ar clusters.

**Table 6.2** – Fit details of scaling of the calculated effective interaction volume to the X-ray intensities measured.

scan parameters	$\chi^2$ / ndf	scaling parameter / $\mu\text{m}^{-3}$
200 nm zirconium filter		
16 bar, 25 K, 30 fs	10.04 / 15	0.154(11)
16 bar, 34 K, 30 fs	10.32 / 16	0.088(7)

### Summary

In this chapter the measurements of X-ray intensities with an X-ray camera were presented. The X-ray energy was estimated by different filters to a range between 50 eV and a few keV. This identifies the origin of the X-rays measured to be the lower energetic electrons, which are not accelerated by the laser wakefield. The X-ray yield of the interaction of an ultra-short laser pulse with a hydrogen cluster jet was estimated to  $0.7(1) \times 10^7$  photons per shot at a divergence of 4 mrad, which is comparable with values of similar experiments already done by other groups. Various parameters were scanned and the expected dependency on the target density  $I_{\text{X-ray}} \propto n_e^{3/2}$  could be confirmed. Another dependency on the cluster diameter could not be observed. In addition, a relation between the X-ray intensity and the laser pulse energy  $I_{\text{X-ray}} \propto E_L^{3/2}$  was found as an effect of the effective interaction volume.

## 7 Conclusion

This thesis presented studies on the interaction of a 200 TW laser system with a state-of-the-art cluster jet target. The cluster source was designed taking precursor measurements into account, built at the University of Münster and characterised regarding cluster jet density and cluster diameter distribution. The design stagnation temperature of 25 K was achieved even at high stagnation pressures of up to 16 bar. This enables an operation at stagnation conditions in the gaseous, hypercritical and liquid regime opening a completely new parameter regime for investigations on the laser cluster interaction. The stability of the newly built cluster jet target was tested for stagnation conditions in the liquid and in the gaseous regime over several hours and found to be more than sufficient. Measurements with a Michelson interferometer estimated the density of the cluster jet to be below  $1.7 \times 10^{18} \text{ cm}^{-3}$  which is in good agreement with the calculated predictions. C. Mannweiler evaluated the Mie scattering data taken in the scope of his master's thesis [Man19], resulting in a small adjustment of the Hagen law to the gas and hardware used ( $A_N = 33 \rightarrow 25(5)$ ). This enables a prediction of the mean cluster diameter in the cluster jet for all stagnation conditions in the gaseous regime. Shadowgraphy measurements revealed the cluster size distribution in the liquid regime for the first time for such a cluster jet. The measured cluster sizes of several micrometers were in good agreement with the prediction by the atomisation theory. The interaction probability of an ultra short and highly focused laser pulse with one of the observed clusters was calculated resulting in the prediction of not a single interaction during the measuring campaigns.

Measurements on accelerated protons using a Thomson parabola were taken over a wide parameter regime of the cluster source and the laser pulse. A new evaluation routine was developed for a detailed handling of systematic uncertainties. A maximum proton energy of 301(49) keV in supposable ultra short pulses was achieved during the measuring

campaigns at optimal laser and target parameters. The proton spectra showed a good shot-to-shot stability and the cut-off energies were at stagnation conditions in the gaseous regime in good agreement with the adjusted Hagen law. The secondary dependency of the proton spectra on the laser intensity was confirmed in scans of the laser pulse energy and the laser pulse duration. A decrease of the proton flux for lower laser intensities as an effect of a smaller effective interaction volume was observed. At stagnation conditions in the liquid regime no hint of any interaction of the laser with a micrometer sized cluster was found. Instead, proton spectra with typical cut-off energies of up to around 200 keV were measured. These spectra originate from another cluster size distribution generated parallel to the larger clusters during the atomization process. The smaller clusters interact with the laser pulse and their diameters can be calculated from the achieved energies to be below 56 nm. The proton spectra taken at stagnation conditions in the liquid regime showed no significant difference to each other allowing the conclusion that the cluster size distribution of the smaller clusters generated in this regime is independent of the stagnation pressure and temperature. A bigger focus volume of high laser intensity would be necessary to achieve an interaction with the larger clusters. Should a Coulomb explosion of these clusters be realised, the expected proton energies are up to several hundred MeV.

Laser wakefield accelerated electrons were measured in laser forward direction. The Thomson parabola showed only a very weak signal with electron energies up to 11.9(1.8) MeV in supposable ultra short pulses. A significant signal was measured only at highest effective target densities corresponding to stagnation conditions in the hypercritical regime. Image plates were used to investigate accelerated electrons closer to the interaction point. A ringlike structure around a central spot was found. The energy of these electrons was below 150 keV and therefore the electrons were identified as escaped electrons, which were not accelerated in the laser wakefield. This structure was already observed before at gas jet targets with densities several orders of magnitude higher than the cluster jet target used in this work.

The X-ray radiation generated in the laser cluster interaction was recorded with an X-ray camera. Different filter layers allowed an estimation of the X-ray energy to a range between 50 eV and a few keV. The measured X-ray intensity was determined for optimised conditions to be  $7(1) \times 10^6$  photons per shot at an opening angle of 4 mrad. The expected dependency on the target density  $I_{\text{X-ray}} \propto n_e^{3/2}$  could be confirmed by

---

scanning different target parameters. A dependency on the cluster sizes could not be observed. The relation  $I_{\text{X-ray}} \propto E_{\text{L}}^{3/2}$  was found during laser energy scans as an effect of the effective interaction volume.





# A Appendix

## A.1 Proton spectra taken under $45^\circ$

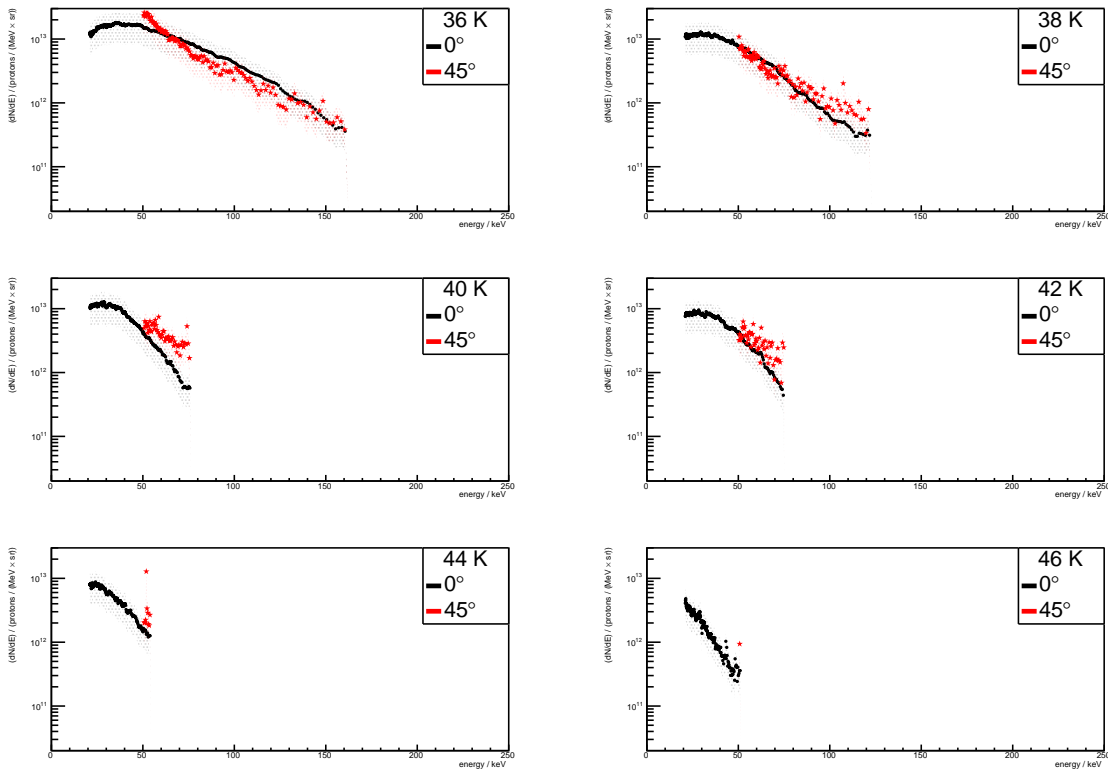


**Figure A.1** – Comparison of proton spectra obtained with two different Thomson parabolas at different angles to the laser propagation direction in the gaseous cluster regime. Since a calibration of the Thomson parabola used under  $45^\circ$  was missing, the spectra are scaled with a global and constant factor to match the spectra obtained under  $0^\circ$ . The factor is the mean ratio of the un-calibrated proton flux measured under  $45^\circ$  and the calibrated proton flux measured under  $0^\circ$ . The mean value was calculated over all energies and shots of a whole temperature scan.

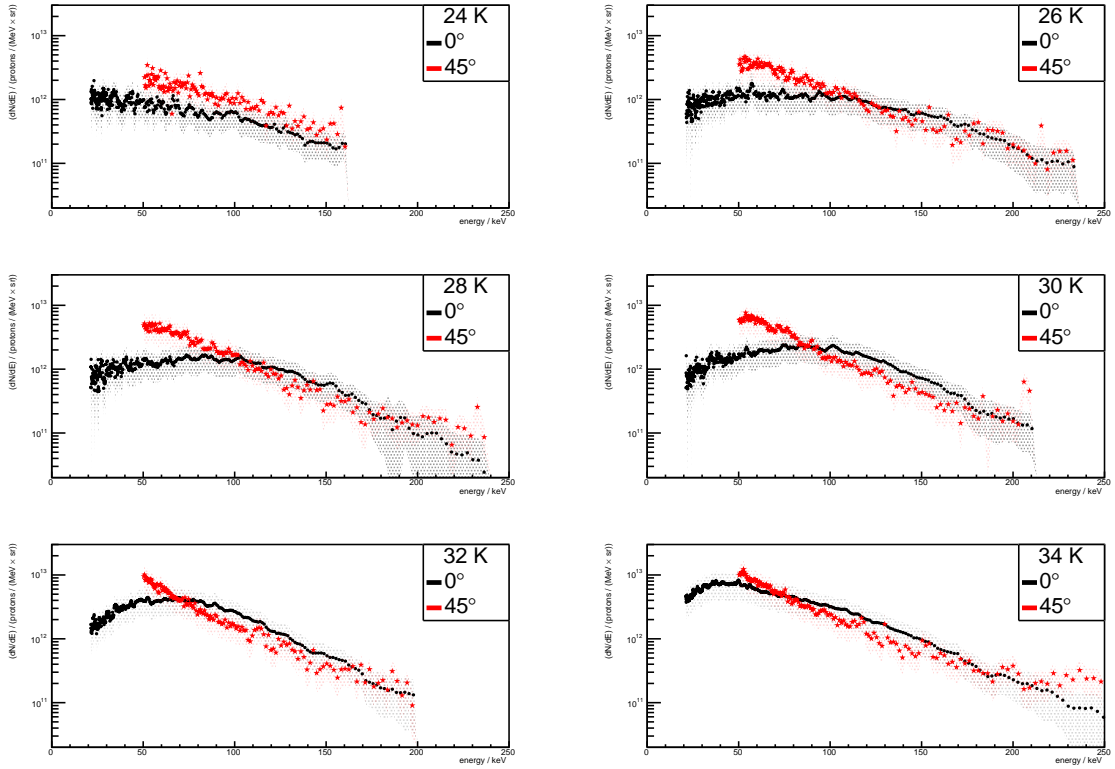


**Figure A.2** – Comparison of proton spectra obtained with two different Thomson parabolas at different angles to the laser propagation direction in the liquid cluster regime. Since a calibration of the Thomson parabola used under  $45^\circ$  was missing, the spectra are scaled with a global and constant factor to match the spectra obtained under  $0^\circ$ . The factor is the mean ratio of the un-calibrated proton flux measured under  $45^\circ$  and the calibrated proton flux measured under  $0^\circ$ . The mean value was calculated over all energies and shots of a whole temperature scan.

## A.2 Proton stability measurements

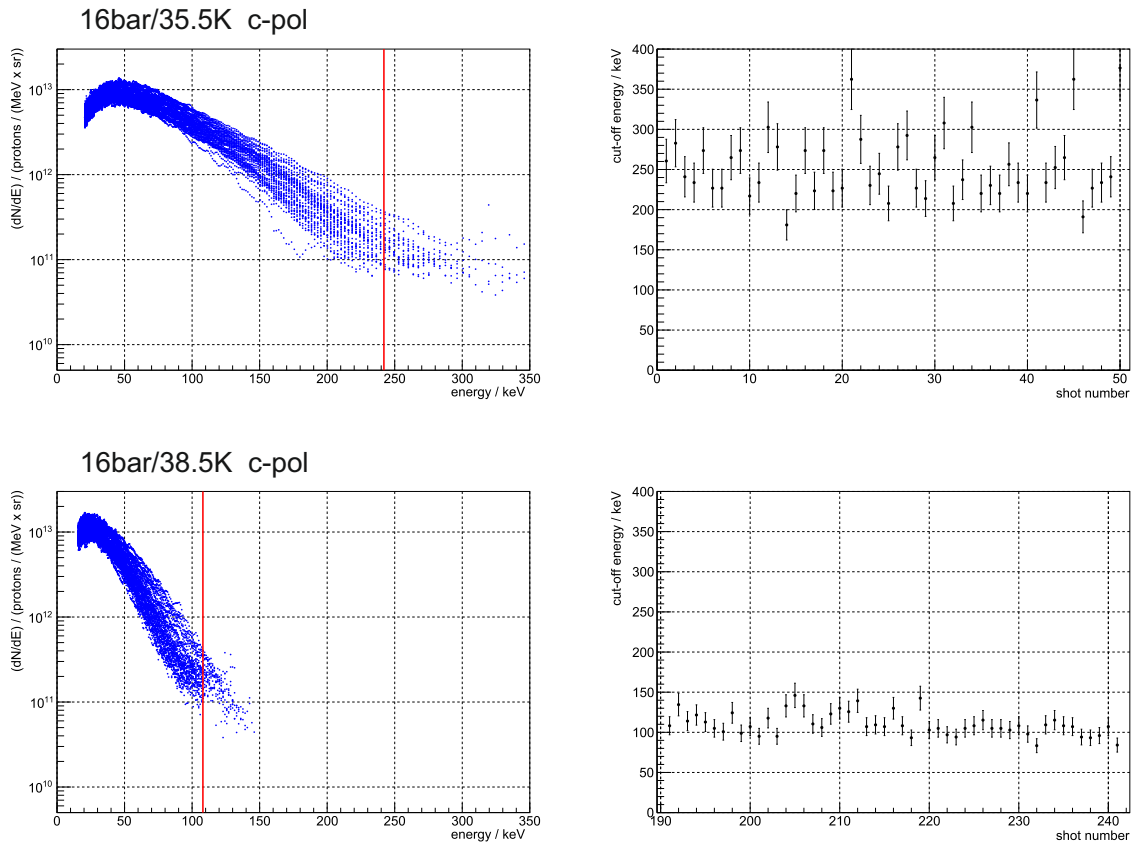


**Figure A.3** – Two stability scans taken at circular laser polarisation. The stagnation conditions of the cluster jet were (from top to bottom) 16 bar and 35.5 K and 16 bar and 38.5 K. The left side shows the 50 proton spectra of the stability scan with the mean cut-off energy marked with the red line and the right side shows the corresponding cut-off energies of the single shots in the scans.

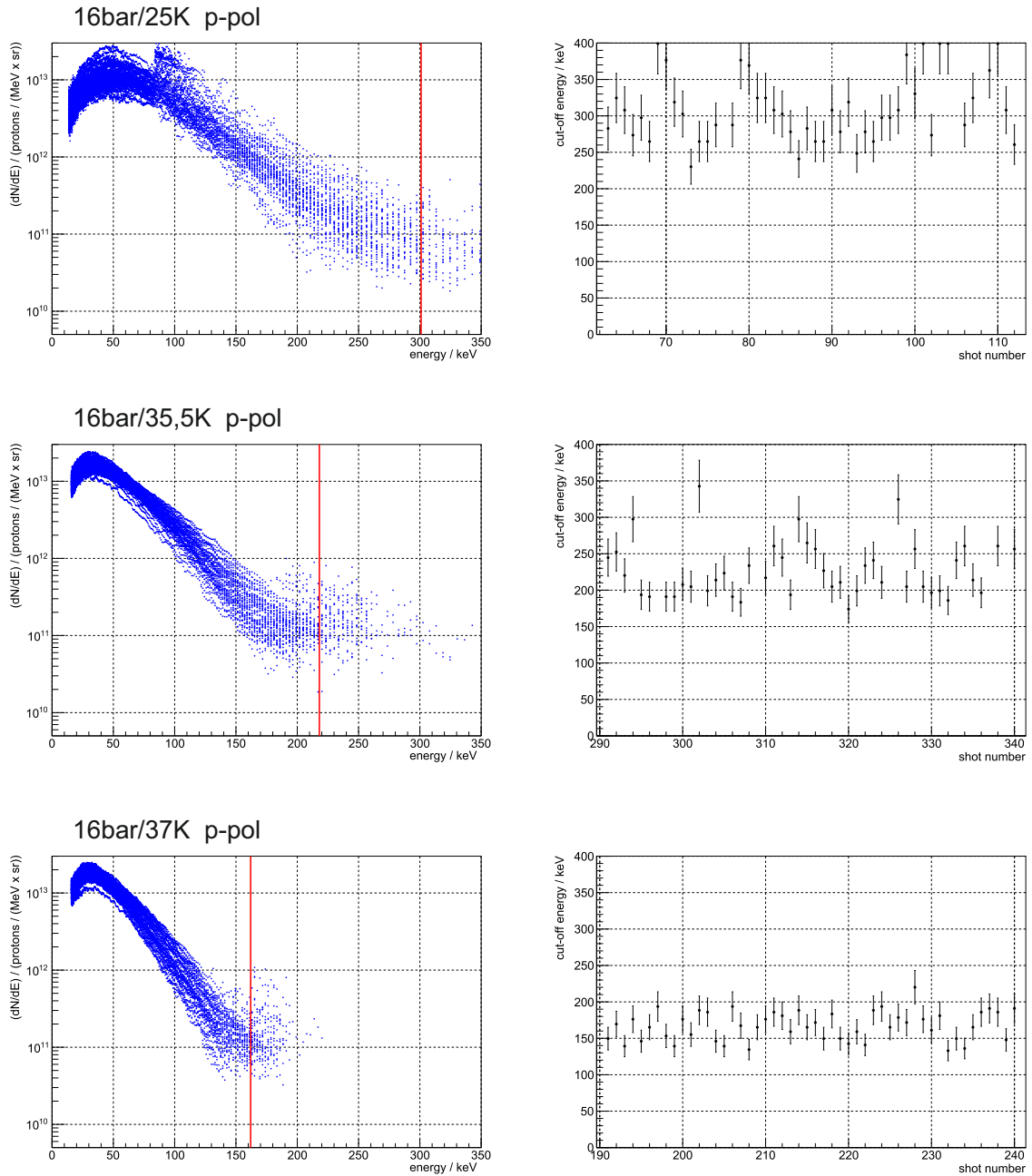


**Figure A.4** – Three stability scans. The stagnation conditions of the cluster jet were (from top to bottom) 16 bar and 25 K, 16 bar and 35.5 K and 16 bar and 37 K. The left side shows the 50 proton spectra of the stability scan with the mean cut-off energy marked with the red line and the right side shows the corresponding cut-off energies of the single shots in the scans.

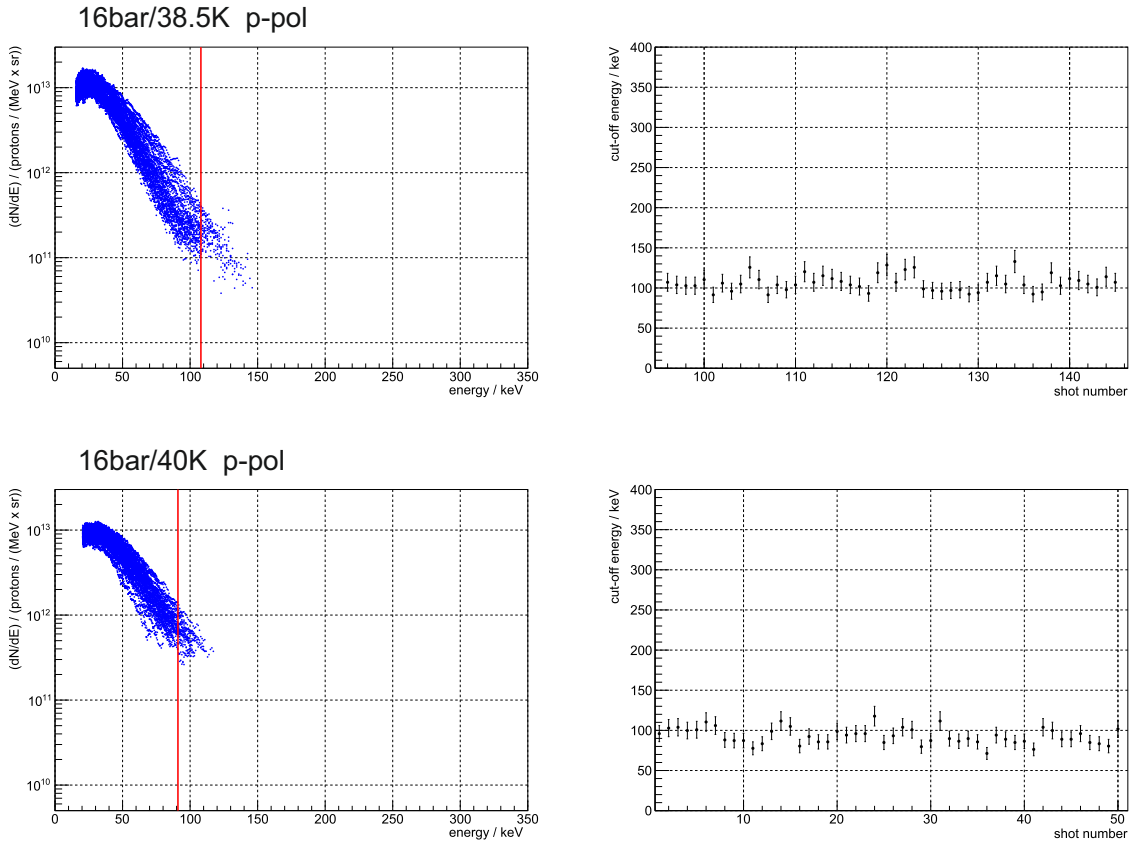


**Figure A.5** – Two stability scans. The stagnation conditions of the cluster jet were (from top to bottom) 16 bar and 38.5 K and 16 bar and 40 K. The left side shows the 50 proton spectra of the stability scan with the mean cut-off energy marked with the red line and the right side shows the corresponding cut-off energies of the single shots in the scans.

### A.3 Proton laser pulse energy scans

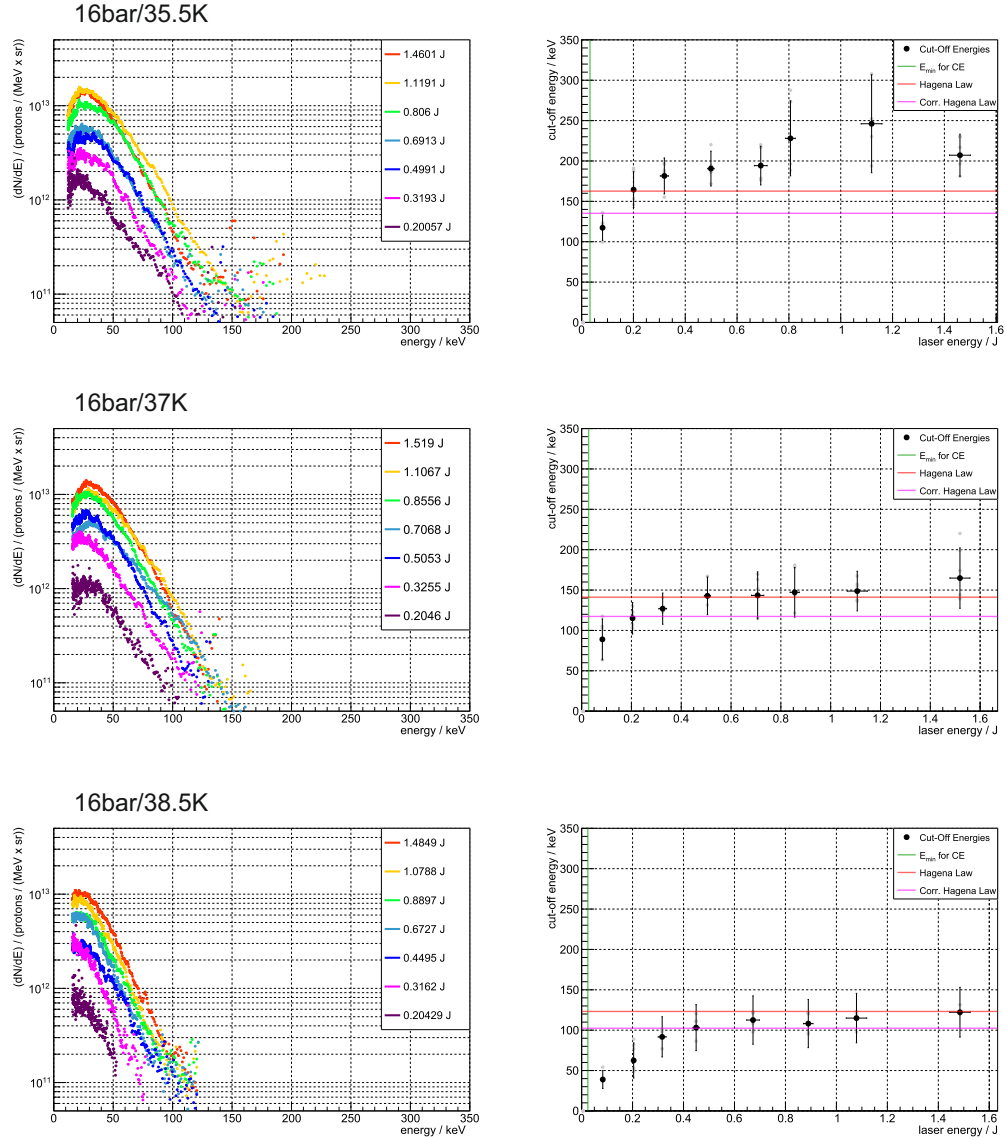


**Figure A.6** – Three laser pulse energy scans. The left side shows the proton spectra and the right side shows the corresponding cut-off energies of the different laser energies, respectively. The scan shown on the top was taken at 16 bar and 35.5 K, the scan in the middle at 16 bar and 37 K and the scan on the bottom was taken at 16 bar and 38.5 K. The red and magenta lines mark the expectations calculated from the Hagena scaling law and a pure Coulomb explosion with the original and the corrected parameters. The green line is drawn at the laser pulse energy necessary for a pure Coulomb explosion of the calculated mean cluster size.

# Bibliography

- [A<sup>+</sup>19] B. Aurand et al. A multi-Hertz, kiloelectronvolt pulsed proton source from a laser irradiated continuous hydrogen cluster target. *Physics of Plasmas*, 26(7):073102, 2019.
- [A<sup>+</sup>20] B. Aurand et al. A laser-driven droplet source for plasma physics applications. *Laser and Particle Beams*, 38(4):214–221, 2020.
- [A<sup>+</sup>21] B. Aurand et al. Electron injection in laser-driven wakefields from a hydrogen cluster target. *in preparation*, 2021.
- [B<sup>+</sup>19] K. Behm et al. Measurements of electron beam ring structures from laser wakefield accelerators. *Plasma Physics and Controlled Fusion*, 61(6):065012, 2019.
- [BH08] C. F. Bohren and D. R. Huffman. *Absorption and scattering of light by small particles*. John Wiley & Sons, 2008.
- [BP66] Yu. P. Blagoi and V.V. Pashkov. Surface Tension of Hydrogen Near the Critical Point. *Soviet Physics JETP*, 22(5), 1966.
- [Bra17] S.K. Brauckmann. *X-ray generation by high intensity laser pulses*. Doctoral thesis, Heinrich-Heine-Universität Düsseldorf, 2017.
- [C<sup>+</sup>13] L.M. Chen et al. Bright betatron X-ray radiation from a laser-driven-clustering gas target. *Scientific reports*, 3(1):1–5, 2013.
- [C<sup>+</sup>18] M.H. Cho et al. Controlled electron injection facilitated by nanoparticles for laser wakefield acceleration. *Scientific reports*, 8(1):1–8, 2018.
- [C<sup>+</sup>19] M. Cerchez et al. ARCTURUS laser: a versatile high-contrast, high-power multi-beam laser system. *High Power Laser Science and Engineering*, 7, 2019.

- [D<sup>+</sup>96] T. Ditmire et al. Interaction of intense laser pulses with atomic clusters. *Physical Review A*, 53(5):3379, 1996.
- [D<sup>+</sup>97] S. Dobosz et al. Absolute keV photon yields from ultrashort laser-field-induced hot nanoplazmas. *Physical Review A*, 56(4):R2526, 1997.
- [Dem09] W. Demtröder. *Elektrizität und Optik*, volume 2. Springer, 2009.
- [DPM15] M. Dell’Angela, F. Parmigiani, and M. Malvestuto. Time resolved X-ray absorption spectroscopy in condensed matter: A road map to the future. *Journal of Electron Spectroscopy and Related Phenomena*, 200:22–30, 2015.
- [G<sup>+</sup>17] M. Gauthier et al. High repetition rate, multi-MeV proton source from cryogenic hydrogen jets. *Applied Physics Letters*, 111(11):114102, 2017.
- [G<sup>+</sup>19] S. Grieser et al. Nm-sized cryogenic hydrogen clusters for a laser-driven proton source. *Review of Scientific Instruments*, 90(4):043301, 2019.
- [Gib05] P. Gibbon. *Short Pulse Laser Interactions with Matter*. Imperial College Press, 2005. Copyright@2005.
- [Gri14] S. Grieser. *The cluster-jet target MCT1S and the analysis of cluster beams*. Master’s thesis, Westfälische Wilhelms-Universität Münster, 2014.
- [Gri18] S. Grieser. *Cluster-Jet Targets for the  $\bar{P}$ anda-, MAGIX-, and CryoFlash-Experiments at Hadron-, Lepton-, and Laser-Facilities*. Doctoral thesis, Westfälische Wilhelms-Universität Münster, 2018.
- [Hag87] O.F. Hagena. Condensation in free jets: Comparison of rare gases and metals. *Zeitschrift für Physik D Atoms, Molecules and Clusters*, 4(3):291–299, 1987.
- [Hag92] O.F. Hagena. Cluster ion sources. *Review of scientific instruments*, 63(4):2374–2379, 1992.
- [Hah09] D. W. Hahn. Light scattering theory. *Department of Mechanical and Aerospace Engineering, University of Florida*, 2009.
- [Har19] C. Hargens. *Development and Set-up of a Droplet Generator for Cryogenic Fluids*. Master’s thesis, Westfälische Wilhelms-Universität Münster, 2019.



- 
- [HGD93] B.L. Henke, E.M. Gullikson, and J.C. Davis. X-ray interactions: photoabsorption, scattering, transmission, and reflection at  $E=50\text{--}30000$  eV,  $Z=1\text{--}92$ . *Atomic Data and Nuclear Data Tables*, 54(2):181–342, July 1993.
- [Inc16] MKS Instruments Inc. MKS Baratron Type 722B Absolute Pressure Transducer. [https://www.mksinst.com/mam/celum/celum\\_assets/resources/722B-1034138-001-MAN.pdf?1](https://www.mksinst.com/mam/celum/celum_assets/resources/722B-1034138-001-MAN.pdf?1), 2016.
- [Ins13] Brooks Instrument. Brooks SLA5850, SLA5851, SLA5853 Mass Flow Controllers Models and Models SLA5860, SLA5861, SLA5863 Mass Flow Meters. <https://www.brooksinstrument.com/~media/brooks/documentation/products/mass-flow-controllers/elastomer%20sealed/sla5800/revision%20a/mass-flow-controller-installation-manual-sla5850-sla5851-sla5853-sla5860-sla5861-sla5863-en.pdf?la=en>, 2013.
- [Ins20] Andor Oxford Instruments. Direct Detection. <https://andor.oxinst.com/learning/view/article/direct-detection>, 2020.
- [J<sup>+</sup>04] T. A. Johnson et al. Zirconium and niobium transmission data at wavelengths from 11-16 nm and 200-1200 nm. In *Optical Constants of Materials for UV to X-Ray Wavelengths*, volume 5538, pages 119–124. International Society for Optics and Photonics, 2004.
- [J<sup>+</sup>18] S. Jinno et al. Micron-size hydrogen cluster target for laser-driven proton acceleration. *Plasma Physics and Controlled Fusion*, 60(4):044021, 2018.
- [K<sup>+</sup>16] S. Kar et al. Guided post-acceleration of laser-driven ions by a miniature modular structure. *Nature communications*, 7(1):1–7, 2016.
- [K<sup>+</sup>19] V. Kaymak et al. Boosted acceleration of protons by tailored ultra-thin foil targets. *Scientific Reports*, 9(1):1–10, 2019.
- [Kho21] Alfons Khoukaz. Private Communication, 2021.
- [Köh15] E.D. Köhler. *Mass spectroscopy of hydrogen cluster-jets and beam density optimisation studies*. Doctoral thesis, Westfälische Wilhelms-Universität Münster, 2015.
- [Kuc94] Horst Kuchling. *Taschenbuch der physik*, volume 17. Fachbuchverl., 1994.

- [L<sup>+</sup>06a] W.P. Leemans et al. GeV electron beams from a centimetre-scale accelerator. *Nature physics*, 2(10):696–699, 2006.
- [L<sup>+</sup>06b] Z. Li et al. Study on the interaction of intense femtosecond laser pulses with nanometre-sized hydrogen clusters. *Chinese Physics*, 15(4):697, 2006.
- [Ley16] Leybold. IONIVAC. [https://www.leyboldproducts.de/media/pdf/43/0c/00/17200137\\_001\\_C0\\_ITR200\\_DE.pdf](https://www.leyboldproducts.de/media/pdf/43/0c/00/17200137_001_C0_ITR200_DE.pdf), 2016.
- [LM17] A. H. Lefebvre and V. G. McDonell. *Atomization and sprays*. CRC press, 2017.
- [LSC21] Inc. Lake Shore Cryotronics. DT-670 Silicon Diodes. [https://www.lakeshore.com/docs/default-source/product-downloads/catalog/lstc-dt670\\_1.pdf?sfvrsn=fc2ebd1f%206](https://www.lakeshore.com/docs/default-source/product-downloads/catalog/lstc-dt670_1.pdf?sfvrsn=fc2ebd1f%206), 2021.
- [M<sup>+</sup>02] V. Malka et al. Electron acceleration by a wake field forced by an intense ultrashort laser pulse. *Science*, 298(5598):1596–1600, 2002.
- [M<sup>+</sup>08] V. Malka et al. Principles and applications of compact laser–plasma accelerators. *Nature physics*, 4(6):447–453, 2008.
- [M<sup>+</sup>13] V. Malka et al. Review of laser wakefield accelerators. *Proceedings of IPAC2013*, pages 11–15, 2013. Creative Commons Licence: <https://creativecommons.org/licenses/by/3.0/>.
- [M<sup>+</sup>16] D. Margarone et al. Proton acceleration driven by a nanosecond laser from a cryogenic thin solid-hydrogen ribbon. *Physical Review X*, 6(4):041030, 2016.
- [M<sup>+</sup>20] M.W. Mayr et al. Nonlinear wakefields and electron injection in cluster plasma. *Physical Review Accelerators and Beams*, 23(9):093501, 2020.
- [Man19] C. Mannweiler. *Commissioning and characterisation of a cluster-jet target for CryoFlash*. Master’s thesis, Westfälische Wilhelms-Universität Münster, 2019.
- [ME51] R.A. Mugele and H.D. Evans. Droplet size distribution in sprays. *Industrial & Engineering Chemistry*, 43(6):1317–1324, 1951.
- [Mer12] W. Merzkirch. *Flow visualization*. Elsevier, 2012.
- [Mes04a] D. Meschede. *Gerthsen Physik*, volume 22. Springer, 2004.

- [Mes04b] R. Messerschmid. *Zerstäubung von Flüssigkeiten in einer nicht angepassten Lavaldüse*. Doctoral thesis, Rheinische Friedrich-Wilhelms-Universität Bonn, 2004.
- [Mie55] C.C. Miesse. Correlation of experimental data on the disintegration of liquid jets. *Industrial & Engineering Chemistry*, 47(9):1690–1701, 1955.
- [MTN08] P. J. Mohr, B. N. Taylor, and D. B. Newell. CODATA recommended values of the fundamental physical constants: 2006. *Journal of Physical and Chemical Reference Data*, 80(3):633–1284, 2008.
- [N<sup>+</sup>01] K. Nishihara et al. High energy ions generated by laser driven Coulomb explosion of cluster. *Nuclear Instruments and Methods in Physics Research Section A: Accelerators, Spectrometers, Detectors and Associated Equipment*, 464(1-3):98–102, 2001.
- [NN05] W. Nolting and W. Nolting. *Grundkurs Theoretische Physik 4: Spezielle Relativitätstheorie, Thermodynamik*. Springer, 2005.
- [O<sup>+</sup>16] T.M. Ostermayr et al. Proton acceleration by irradiation of isolated spheres with an intense laser pulse. *Physical Review E*, 94(3):033208, 2016.
- [PP17] B. Paroli and M.A.C. Potenza. Radiation emission processes and properties: synchrotron, undulator and betatron radiation. *Advances in Physics: X*, 2(3):978–1004, 2017.
- [PV<sup>+</sup>19] P. Puyuelo-Valdes et al. Laser driven ion acceleration in high-density gas jets. In *Laser Acceleration of Electrons, Protons, and Ions V*, volume 11037, page 110370B. International Society for Optics and Photonics, 2019.
- [R<sup>+</sup>01] J.-P. Rozet et al. State selective measurements of HCI produced by strong ultrashort laser-clusters interaction. *Physica Scripta*, 2001(T92):113, 2001.
- [S<sup>+</sup>00] R.A. Snavely et al. Intense high-energy proton beams from petawatt-laser irradiation of solids. *Physical review letters*, 85(14):2945, 2000.
- [S<sup>+</sup>04] S. Sakabe et al. Generation of high-energy protons from the Coulomb explosion of hydrogen clusters by intense femtosecond laser pulses. *Physical Review A*, 69(2):023203, 2004.

- [S<sup>+</sup>19] K.M. Schwind et al. A high-repetition rate droplet-source for plasma physics applications. *Nuclear Instruments and Methods in Physics Research Section A: Accelerators, Spectrometers, Detectors and Associated Equipment*, 928:65–69, 2019.
- [Sch08] M.S. Schollmeier. *Optimization and control of laser-accelerated proton beams*. Doctoral thesis, Technische Universität Darmstadt, 2008.
- [Sch13] F. Schwabel. *Quantenmechanik*. Springer-Verlag, 2013.
- [Sch18] A. Schroer. *Investigation of ion acceleration from underdense targets using a high intensity short pulse laser*. Doctoral thesis, Heinrich-Heine-Universität Düsseldorf, 2018.
- [Sch20] K.M. Schwind. *Laserbeschleunigung von Teilchen aus einem kryogenen Clustertarget*. Master’s thesis, Heinrich-Heine-Universität Düsseldorf, 2020.
- [SDT98] R.A. Smith, T. Ditmire, and J.W.G. Tisch. Characterization of a cryogenically cooled high-pressure gas jet for laser/cluster interaction experiments. *Review of scientific instruments*, 69(11):3798–3804, 1998.
- [T<sup>+</sup>10] D.B. Thorn et al. Spectroscopy of betatron radiation emitted from laser-produced wakefield accelerated electrons. *Review of Scientific Instruments*, 81(10):10E325, 2010.
- [Täs12] A. Täschner. *Entwicklung und Untersuchung von Cluster-Jet-Targets höchster Dichte*. Doctoral thesis, Westfälische Wilhelms-Universität Münster, 2012.
- [Y<sup>+</sup>17] X. Yang et al. Three electron beams from a laser-plasma wakefield accelerator and the energy apportioning question. *Scientific Reports*, 7:43910, 2017.



# Acknowledgements

Zu guter Letzt möchte ich allen Menschen, die zum Gelingen dieser Arbeit beigetragen haben, danken.

Mein Dank gilt meinem Doktorvater Prof. Dr. Alfons Khoukaz, der nicht nur das Thema dieser Arbeit vorgeschlagen hat, sondern auch ein konstantes Interesse an jedwedem Fortschritt zeigte und mich mit seiner kritischen Art stets zu Bestleistungen anspornte.

Des Weiteren danke ich Prof. Dr. Christian Klein-Bösing und Prof. Dr. Jochen Heitger für ihre Mühen als Zweit- bzw. Drittgutachter.

Besonders großer Dank gilt unserem Ingenieur Daniel Bonaventura, der mechanischen Werkstatt unter Georg Bourichter und der Elektronikabteilung unter Roland Berendes für die weitreichende Unterstützung und die zahlreichen angefertigten Bauteile.

Der ganzen Arbeitsgruppe danke ich für die anregenden Diskussionen und die gute Zusammenarbeit. Dabei möchte ich besonders die tolle Atmosphäre im Büro mit meinen Bürokollegen Johannes Bloms, Frederik Weidner aka Slim, Dr. Marcel Rump, Dr. Christopher Fritsch und Dr. Nils Hüsken würdigen. Ganz spezieller Dank geht auch an Christian Mannweiler, der mich im Rahmen seiner Masterarbeit oft auf Messzeiten und im heimischen Labor begleitet hat. Das hat echt Spaß gemacht mit dir!

Ich möchte auch den Kollegen der Heinrich Heine Universität Düsseldorf Dr. Rajendra Prasad, Dr. Mirela Cerchez, Dr. Bastian Aurand, Kerstin Schwind und Esin Aktan aus der Arbeitsgruppe um Prof. Willi danken. Die mit euch durchgeführten Experimente und Diskussionen werde ich immer in guter Erinnerung behalten.

Großer Dank gilt auch meiner motivierenden und aufbauenden Kafferrunde bestehend zunächst aus Kai (ja genau, Kyle Katarn der legendäre Held, der Jerec im Tal der Jedi

besiegt hat), Daniello und Mickebird und später aus Marco und Paul. Unsere kurzen Unterbrechungen des Arbeitstages habe ich immer sehr genossen.

Für das Korrekturlesen dieser langen Arbeit bin ich Stefan Fortmeier und Christian Mannweiler zu immensem Dank verpflichtet!

Zuletzt möchte ich auch meinen Freunden und meiner Familie für ihre konstante Unterstützung danken. Ganz besonderer Dank gilt dabei meiner Lebensgefährtin Laura, die auch in der letzten sehr anstrengenden Phase meiner Arbeit, die geprägt von Corona-Lockdowns, Homeoffice und Baby-Betreuung war, ihr Bestes gab um mich bei meiner Arbeit zu unterstützen.





# Curriculum Vitae

Name	Lukas Leßmann
Geburtsdatum	23.05.1990
Geburtsort	Münster
Staatsangehörigkeit	Deutsch
Eltern	Norbert und Gudrun Leßmann
<b>Schulausbildung</b>	
1996-2000	Baumberge-Schule, Katholische Grundschule Havixbeck
2000-2009	Freiherr-vom-Stein-Gymnasium, Münster
20.06.2009	Allgemeine Hochschulreife
<b>Zivildienst</b>	
2009-2010	Unterstützende Tätigkeiten im Operationsbereich der Klinik für Hals-, Nasen- und Ohrenheilkunde der Universitätsklinik Münster
<b>Studium</b>	
2010-2013	Bachelor Studium der Physik an der Westfälischen Wilhelms-Universität Münster
24.10.2013	Bachelorarbeit im Institut für Kernphysik „Systematische Untersuchungen von TLD-Kristallen an einem Thermolumineszent-Aufbau für das kernphysikalische Praktikum“
2013-2017	Master Studium der Physik an der Westfälischen Wilhelms-Universität Münster
23.12.2016	Masterarbeit im Institut für Kernphysik „Investigations on gas jet beam profiles with a Mach-Zehnder interferometer“
23.01.2017	Masterabschluss
<b>Promotionsstudium</b>	
01.04.2017	Beginn der Dissertation am Institut für Kernphysik der Westfälischen Wilhelms-Universität Münster unter der Betreuung von Prof. Dr. Alfons Khoukaz
<b>Berufstätigkeit</b>	
2014-2016	Studentische Hilfskraft am Institut für Theoretische Physik der Westfälischen Wilhelms-Universität Münster zur Betreuung von Bachelor-Studenten in einer Übungsgruppe